Mathematical modeling and numerical methods in three types of physical systems

by

Matthew R. G. Forbes
B.Sc., University of Victoria, 2021
B.Sc., University of Victoria, 2023

A Thesis Submitted in Partial Fulfillment of the
Requirements for the Degree of

MASTER OF SCIENCE

in the Department of Physics and Astronomy

We acknowledge and respect the Lək̓ʷəŋən (Songhees and Xʷsepsəm/Esquimalt) Peoples on whose territory the university stands, and the Lək̓ʷəŋən and W̱SÁNEĆ Peoples whose historical relationships with the land continue to this day.

Mathematical modeling and numerical methods in three types of physical systems

by

Matthew R. G. Forbes
B.Sc., University of Victoria, 2021
B.Sc., University of Victoria, 2023

Supervisory Committee

Dr. T. E. Baker, Co-Supervisor
(Department of Physics and Astronomy, Department of Chemistry, University of Victoria)

Dr. L. Leonard, Co-Supervisor
(School of Earth and Ocean Sciences, University of Victoria)

Dr. K. Jensen, Departmental Member
(Department of Physics and Astronomy, University of Victoria)

ABSTRACT

Within this thesis three physical systems are explored through a variety of methods. First, the ice thickness of Comox and Kokanee glaciers are modeled via relative gravity measurements. Efficacy of the modeling method is contrasted to more direct techniques, showing it to be largely viable. A first ever average ice thickness is therefore provided for Comox glacier at 42 ± 4 m. At the opposite scale, a 1 dimensional (1D) quantum system is constructed and explored through random matrices. The 1D Anderson model is considered here, exploring the effects of correlated disorder on localization, scaling, and the overall behavior in contrast to similar systems with uniform disorder. While some differences are seen in scaling and some questions remain unanswered, the behavior largely coincides with expectations. Finally, numerical methods are explored for 2 dimensional classical spin systems via tensor network renormalization algorithms. With the goal of eventually contrasting all known algorithms to date, how tensor networks are constructed, how they are represented, and a summary of the algorithms coded to date are provided. This thesis therefore provides not only new results across several areas of physics, but also serves as a set of short introductions into a variety of different topics.

Contents

List of Tables

List of Figures

ACKNOWLEDGEMENTS

I would like to thank:

Professor Lucinda Leonard, for guiding me through the research on glaciers and lending me the expensive equipment with very few questions asked.

Dr. Michael Flynn, for introducing me to random matrices within the realm of chaotic (or not!) quantum systems, as well as his continued patience.

Professor Thomas E Baker, for his introduction to tensor networks and numerical methods in classical statistical systems.

The Faculty of Science, for providing the initial funding for the gravity survey through the SURA award.

R.M. Petrie Memorial Fellowship, for helping to fund my studies.

The Faculty of Graduate Studies, for the travel grant which allowed me to attend the APS March conference in 2024.

my Mother, for hiking the Glaciers with me.

my Brother, for getting up early to drive to Comox Glacier.

my Father for lending me his truck.

DEDICATION

This one goes out to the bees and the trees.

Chapter 1

Introduction

Throughout physics the mathematical and numerical methods required to effectively model and analyze a system vary greatly from one topic to the next. This thesis will explore three entirely different systems with the goal of both reviewing the methods applied in the respective area, as well as proposing new approaches and results.

Each chapter in this thesis will be largely self-contained. Emphasis will either be given to analyzing the unique system in question (Chapter 3), or to the methods (Chapter 4), or both (Chapter 2). The chapters have been ordered to begin with the most physically tangible case first, continue into a more abstract system in 1 and 2 dimensions, and finally conclude with a review of numerical methods for application in 2 and 3 dimensions.

An outline of the topics considered in subsequent chapters is provided below.

Chapter 2 will look at modeling glacier ice thickness through local changes in measured gravity. A short overview of the gravitational corrections used to determine the local gravity anomaly will be reviewed, as well as how and why gravity methods can be applied to studying glaciers. An overview of the chosen glaciers and relevant steps associated with the field work are then summarized, and the method is finally applied to two data sets. The chapter will conclude with a statement on the new results and effectiveness of modeling glaciers with gravity, in addition to a comparison against more direct methods.

Chapter 3 will focus on the study of quantum chaos, or mainly lack thereof, within the 1 dimensional Anderson model using correlated random potentials retrieved through the sampling of random unitary matrices. Single particle level statistics, quantum dynamics, and more, will be discussed. Scaling collapses determined

here will be used as a way to compare the model to other similar work. The localization time, and critical particle hopping amplitude will also be determined in relation to the previously defined localization-to-localization transition. With work still ongoing, the chapter concludes with current questions and results for extending into 2 dimensions.

Chapter 4 contains a review of tensor networks and coded examples of all major tensor network renormalization group algorithms for classical spin systems in 2 and 3 dimensions. Important aspects of general tensor network operations are initially given alongside how the tensor networks are constructed for the method. This is followed by a detailed description of the various tensor network algorithms coded for inclusion into the DMRJulia library, which have been grouped by algorithmic similarity. The section is concluded with a short demonstration of a few of the algorithms through simulation of the Ising model on the square lattice.

Chapter 5 concludes the thesis with a brief summary of the work.

Chapter 2

Modeling Glaciers Through Gravity

2.1 Importance of glaciers

Ongoing reduction in permanent ice volume has been consistently witnessed across most glacial systems around the world [8]. Beyond the environmental impacts of such changes, billions of people worldwide are currently dependent, at least in part, on glacial systems for sufficient water supply, agricultural output, and economic stability [9]. For 45,000 residents on Vancouver Island in British Columbia, Canada, the water supply has historically been buffered by the now receding Comox Glacier (CG) [10, 11]. Although no direct measurements of CG have been made to date, a high-resolution regional glaciation model constrained by satellite imagery of both the Coast Range and Vancouver Island mountains projected an approximately 50% loss of ice coverage by 2050 [12]. While the loss of the glacier may not be immediately disastrous for the regional population since much of the water supply is fed through precipitation on the surrounding watershed, it will put more pressure on a vital resource for an increasingly populated region as climate change continues and summer dry periods in the area lengthen [13].

On a broader scale beyond the Comox region, of the some 200,000 glaciers globally, direct measurements of ice thickness are available for only around 5000 [14]. Current direct methods used to make these observations, such as ice penetrating radar or drilling a borehole, although accurate and relatively simple, are often expensive, potentially time consuming, and require equipment that may be difficult to transport to the desired location. Indirect methods, like satellite imagery, can readily be used to provide measures of glacial surface area [15], but provide no direct indication of

ice thickness or volume. To better supply communities with knowledge of their local water system, as well as provide more data to constrain models of glacier and climate dynamics, there is a need for additional methods to infer glacial ice thickness.

The main objective of this chapter is therefore to provide a first baseline measurement of ice thickness for the Comox Glacier through the relatively inexpensive method of ground-based relative gravity surveying. In addition to collecting and modeling a gravity transect across the Comox Glacier, a similar profile across the Kokanee Glacier is also collected such that the modeled ice thickness can be compared with thickness values recently determined using a more direct method. While relative gravity surveys are not a new idea within glaciology, with the method used a few times in the last century (as with the Athabaska Glacier in 1963 [16] or the lower Blue Glacier in 1965 [17] which claimed 5-10% accuracy in ice thickness when using this method) if the model was found truly comparable to current techniques, like ground penetrating radar, it would provide validity to the measurement across Comox Glacier and for relative gravity data contributions to the glacier thickness dataset.

2.2 Data collection and modeling

2.2.1 Fundamentals of the model

Considering the most simple Newtonian picture of gravity, when moving closer to (further from) something with great mass, an increase (decrease) in the magnitude of gravitational acceleration is witnessed. This is, at its most fundamental level, the idea of this model. Thinking about a region of Earth's surface, uniquely high or low density (mass/volume) regions will provide a relative increase or decrease in observed gravity compared to adjacent regions. The only difficulty that remains is isolating the contributions from a specific mass of interest, or for glaciers, quantifying the mass deficit relative to the surrounding rock.

Measuring these relative deviations caused by the inhomogeneity in the near-surface structure, and isolating them from other influences such as elevation, latitude, and more, is a well-known process [18]. That is, finding the Bouguer anomaly, δg^{boug}. With basic knowledge of the material properties in the local area, the determined Bouguer anomaly profile can be used as a reference to infer aspects such as shape and distance to the specific inclusion in question. In this study, focus is thus given

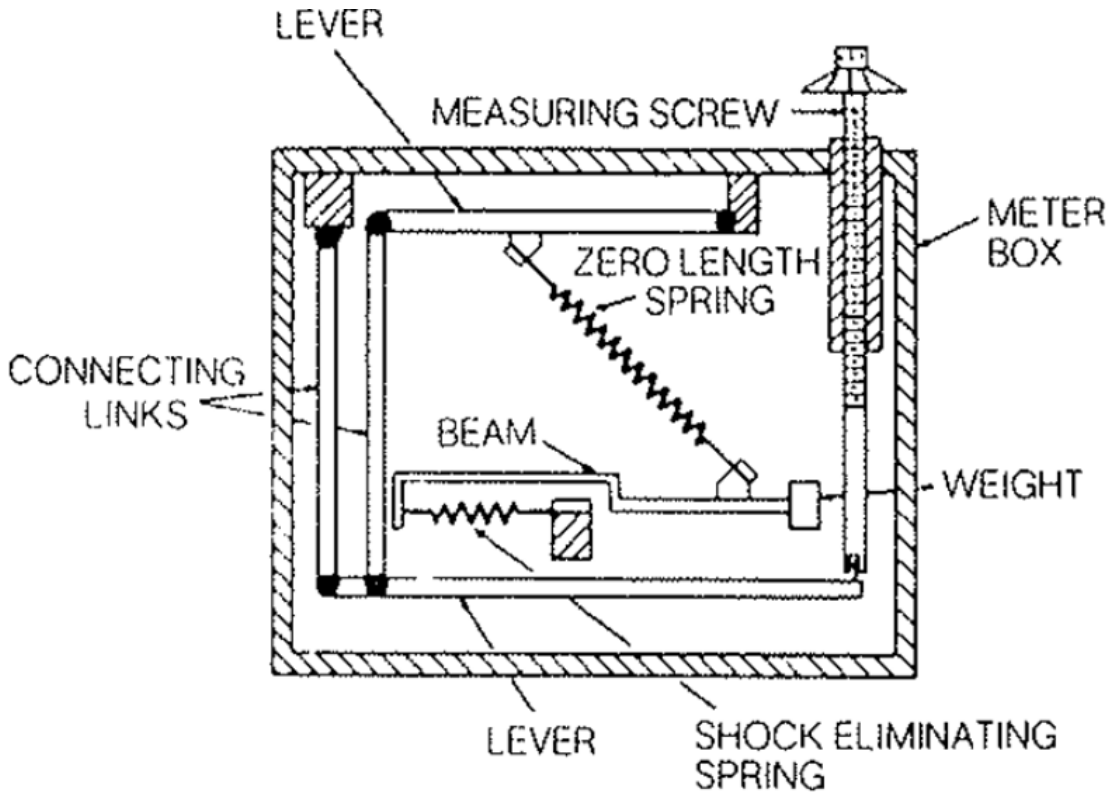

Figure 2.1: Diagram of the LaCoste & Romberg Model G gravity meter [1].

to looking at the point-to-point differences in gravity as underfoot density decreases due to increased ice thickness.

2.2.2 Principles of data collection: the gravity meter

Several methods exist capable of measuring gravity, varying from modern ways involving interferometry, to more traditional methods using a simple pendulum. For the purpose of relative gravitational measurements and surveys, requiring accuracy on the order of 0.01 mGal (10^{-7} ms^{-2}), a robust and portable option, akin to the latter method, is the gravity meter [18].

In this study a LaCoste & Romberg Model G gravity meter is used, fundamentally based on the application of Hooke's law [1, 18]:

$$\begin{aligned} F &= mg \\ &= -k(x - x_0) \end{aligned} \tag{2.1}$$

Under this more basic system a force F occurs in response to the motion of a mass m attached to a spring with constant k from a position x_0 to x under gravitational acceleration g. The model G gravity meter expands on this by using an astatic (counter-balanced) pendulum in an unstable equilibrium by attachment to a "zero-length" spring (Figure 2.1) [1]. The spring has been pre-stressed above critical tension such that a tension to length curve provides a straight line of slope k. In this state, the spring length is additionally approximated as zero. The result is a pendulum which finds a level position under some predetermined gravitational acceleration, g_0.

Under gravity $g^{obs} = g_0 \pm \Delta g$ the already tensioned spring extends or contracts appreciably, which through the appropriate relaxation or tension of the spring through a "measuring screw" restores the pendulum to a level position. Using the appropriate calibration relating the changes in the new applied tension to the difference in gravity, relative measurements can be extracted comparing the gravity at one time and location to the next.

With this process, a relative drop in gravity meter measurements should be expected when comparing the gravity experienced on the high-density rocky edge of a glacier to the low-density ice-filled center. However, These relative measurements take into account all sources which may increase or decrease the observed gravity. The Bouguer anomaly must therefore be extracted from the observed data.

2.2.3 Review of density model corrections

Isolating and modeling contributions only from local subsurface density anomalies (δg^{boug}) recorded as part of the relative gravity measurements (g^{obs}) is essential to determining an accurate value of glacier ice thickness. Below, an introduction and review of the necessary corrections typically considered for a relative gravity survey is supplied, introduced in the order in which they are applied to the raw data. That is:

$$\delta g^{boug} = g^{obs} + \Delta g^{tide} - \Delta g^{base} - \Delta g^{drift} \pm \Delta g^{lat.} + \Delta g^{top.} - \Delta g^{bp} + \Delta g^{elev.} \quad (2.2)$$

all to be defined.

Tidal correction, Δg^{tide}

Before any other corrections can be applied, the temporal changes in gravity caused by the dynamics of the Sun, Moon, and Earth must be accounted for [18]. Minute to minute, the Sun and Moon will not only contribute a changing yet measurable difference in gravitational acceleration (such as the moon acting against the downward acceleration of gravity when overhead), but also deform the Earth's surface. Similar to the ocean tides, by the variable pull from the celestial bodies and the rotation of the Earth, the Earth's crust will gain a small ellipsoid form (i.e. solid Earth tides). These can be expected to reach up to 0.1 mGal.

Fortunately, with the tidal equations being well studied for over a millennium, a MATLAB code, adopted from a program formulated by Ahern (1993) and based on [19] and [20], was already available to perform the set of relevant calculations. The resulting tide correction determined over the time period of each survey may be seen in Figure A.1.

Relative adjustment and instrument effects, Δg^{base} &Δg^{drift}

At the start of the survey a base location must be chosen from which to compare all future relative measurements against. At this location, regardless of time or relation to the rest of the survey area, δg^{boug} will be defined as 0 mgal. Taking a measurement at this location g^{base} therefore sets the value which must be subtracted from all future observations (i.e. Δg^{base}) [1].

Influences internal to the gravity meter must also be considered. To seclude it from the environment the internal mechanism of the gravity meter is housed inside an airtight thermostatic case, kept at a temperature above (most) external environments at 51°C [1]. Due to the natural material properties of the spring, specifically the thermal expansion coefficient, a small drift in the measured values will be present over the course of an experiment, Δg^{drift}. For this reason measurements must be made at the base location at the start and end of the survey, giving a total measurement drift of Δg^{diff}. While some longer or varied surveys require corrections necessitating polynomial or numerically determined functions of the drift [21], here the induced changes are assumed to be a linear function with time t over full survey time Δt, thus giving a point-to-point drift correction of:

$$\Delta g^{drift} = \frac{t}{\Delta t} \Delta g^{diff} \tag{2.3}$$

Latitude correction, $\pm\Delta g^{lat.}$

With the solid Earth tides corrected for and a zero point set at the base station, corrections associated with the latitude and elevation, as well as surrounding terrain, need to be determined. To complete these corrections, it is first noted that Earth is not a sphere, but an ellipsoid bulging at the equator [18]. Let $f = (a - c)/a$ be the flattening of the ellipsoid about the poles where a and c are the major and minor axis. Let it also be given that A is the ratio of the ellipsoid equatorial centrifugal acceleration caused by Earth's rotation to the equatorial gravitational acceleration. The gravity normal to the surface of an ellipsoid at some angle (latitude), $g^{lat.}$, is [18]

$$g_n = g_e(1 + C_1 \sin^2\phi + C_2 \sin^2 2\phi) \tag{2.4}$$

where g_e is the mean equatorial gravity around the major axis, ϕ is the angle from the equator, and C_1, C_2 are

$$\begin{aligned} C_1 &\approx \frac{5}{2}f - f + \frac{15}{4}A^2 - \frac{27}{14}fA \\ C_2 &\approx \frac{1}{8}f^2 - \frac{5}{8}fA \end{aligned} \tag{2.5}$$

For Earth, g_e is $978,031.85$ mGal, and C_1 reduces to around $0.005278895/R_e$ with $R_e = (a^2c)^{1/3} = 6371$km. Since C_2 is composed of only higher order terms fA and f^2 terms it follows that $C_2 \ll C_1$ so may be neglected here.

Taking the first derivative with respect to the angle, it is found that

$$g^{lat.} = g_e C_1 \sin(2\phi) \tag{2.6}$$

Or, relative to some other latitude, this is reformed to give

$$\Delta g^{lat.} = \frac{g_e \alpha}{R_E} \sin(2\phi)\Delta s \tag{2.7}$$

where Δs is the north-south distance from the base station. The latitude correction from base station to measurement point has therefore been found. The value is thus subtracted from the observed gravity for more northern measurements and added to it for more southern ones.

Terrain and the Bouguer plate correction, $\Delta g^{top.}$&Δg^{bp}

Local influences to gravity must also be considered. The following arguments are drawn from [18] and [22]. One can imagine that a large valley (void) or mountain (mass "above" the measurement point) will work to decrease the observed gravity. One way to correct for this is as follows. By first looking at a straight line of terrain extending from the measurement point, one may divide it into sections of distance $r_1 < r_2 < \cdots < r_n$. One can then imagine wrapping the terrain around the measurement point to give it cylindrical symmetry. For example, if the line of terrain was up a hill, the measurement point would now sit at the bottom of a cone made of concentric rings of radius r_n.

A volume of rock with density ρ may then be considered from one of the cylinders at height z, radius r, and angle θ from the origin (measurement point). The mass contribution is thus $\mathrm{d}m = \rho r \mathrm{d}r\ \mathrm{d}z\ \mathrm{d}\phi$ for some amount of angle $\phi_1 \to \phi_2$ around the cylinder. The contribution of gravity from this point is

$$g_n = G\frac{\mathrm{d}m}{r^2+z^2}\cos\theta = G\frac{\rho r z \mathrm{d}r\ \mathrm{d}z\ \mathrm{d}\phi}{(r^2+z^2)^{3/2}} \tag{2.8}$$

where G is the gravitational constant. This can then be integrated over the volume to get the contribution at the measurement point

$$g = G\rho\int_{\phi_1}^{\phi_2}\mathrm{d}\phi\int_{r_n}^{r_n+1}\int_{z=0}^{z+h}\frac{rz}{(r^2+z^2)^{3/2}}\mathrm{d}z\ \mathrm{d}r \tag{2.9}$$

This integral must be taken for every volume element, over every cylinder, at every location measured to retrieve $\Delta g^{top.}$. While surveys in the past may have had to do this by hand, code now exists to complete these operations. As an intensive process by hand, the computational assistance for this correction makes gravity surveys on glaciers a much more approachable method.

Here, GTeC software is used [22]. Similar to above, the code looks at partitioned concentric rings around the measurement point. Input to these calculations was a 1:20,000 topographic dataset at a pixel size of 2 m and elevation grid of 25 m provided by the Province of British Columbia Terrain Resource Information Management [23].

With the terrain correction complete, the valley or peak surrounding the measurement may be considered filled in or removed. However, the measurement point is now sitting on top of or below a uniform fictitious layer of rock. The Bouguer plate

correction is therefore introduced where the contribution is removed as [18]

$$\Delta g^{bp} = 2\pi G\rho h \tag{2.10}$$

where h here is the thickness of the fictitious layer (elevation difference) compared to the base station. With this, all points now sit in the free air suspended above a perfect ellipsoid of mass m_e.

Elevation (free air) correction, $\Delta g^{elev.}$

As a simple final correction, the elevation correction works to account for differences in gravity caused by getting farther from the Earth (or a perfect ellipsoid when the other corrections are applied), here taken as a point mass. That is [18]

$$g^{elev.} = \frac{\mathrm{d}}{\mathrm{d}r}\left(-\frac{Gm_e}{r^2}\right) = \frac{2g_e}{r} \tag{2.11}$$

where m_e is the mass of Earth. The correction relative to a base station is thus

$$\Delta g^{elev.} = \frac{2g_e}{r}\Delta h \tag{2.12}$$

where Δh is the change in height.

2.3 Gravity survey

With a necessary basis for what the measurements are for and how they will be manipulated, here it is provided how the relative gravity measurements were acquired and how they are used to infer ice thickness.

2.3.1 Glacier setting

Comox Glacier (49.550°N, 125.355°W) resides within the Vancouver Island Ranges near the south-eastern border of Strathcona Provincial Park between Black Cat Mountain and Mount Arthur Evans 2.2. The bedrock geology of the region is of the Karmutsen formation (Vancouver group), consisting primarily of middle to upper Triassic basalt [24, 25]. The median, minimum, and maximum glacial altitude was estimated through the Randolph Glacier Inventory 6.0 (RGI 6.0) at 1840 m, 1490 m,

Figure 2.2: Location of Comox Glacier and Kokanee Glacier (red squares) within British Columbia, Canada (Google Earth, Landsat/Copernicus, 01/01/2021).

and 1940 m respectively over an area of approximately 1.55 km^2 [26]. An average altitude was estimated for the survey area at 1872 $\pm$ 2 m via a handheld Garmin ETREX 32x Global Positioning System (GPS) device.

Within mainland BC, Kokanee Glacier (49.749°N, 117.145°W) sits inside Kokanee Glacier National Park in the West Kootenays Selkirk mountain range on the north face of Kokanee peak 2.2. Kokanee Peak and the surrounding mountains are composed of middle Jurassic granite and granodiorite of the Nelson batholith [27, 25, 28]. Occurrences of Triassic argillite, quartzite, and limestone, associated with the Slocan group to the northeast of the batholith, are also dispersed throughout the park [28, 27]. The median, minimum, and maximum glacial altitude was again estimated through the RDI 6.0 dataset at 2620 m, 2230 m, and 2800 m over and area of 2.71 km^2 [26]. The altitude for the survey area was recorded, again with a Garmin ETREX 32x GPS locator, at 2659 $\pm$ 2 m.

2.3.2 Field surveys

Both the CG and KG survey areas were accessed on foot, over a 2-day return trip from the Comox Glacier and Gibson Lake trailheads, respectively. In both cases the survey was completed in the late dry season prior to any snowfall. Conditions on both occasions were well above freezing such that ice was witnessed to melt while the survey was taking place. Surface runoff was observed draining from the head of KG, and within both glaciers running water could be heard below the surface. Many small crevasses were also observed along the transect area, with lengths and depths of at least a few meters.

To take the relative gravity measurements, we use a LaCoste & Romberg Model G gravity meter. Within the model chosen, gravitational acceleration is measured via the mechanical response of a mass on a beam supported by a "zero-length" spring which is clamped during transportation, making it a relatively tough, accessible, yet adequately accurate candidate for on-foot traversal of mountain environments without damage [1]. For this method, by the approximations in ground density and material homogeneity, it is expected that the result of this experiment will serve only as an estimate to the depth of the glacier. As with the aforementioned measurements of the 1960's, an accuracy within 5-10% of the true depth is anticipated [16, 17]. When considering year to year height fluctuations, however, alongside relatively rapid melt, a value within this range may be adequate for many purposes.

Comox Glacier

The gravity survey for CG was carried out on the afternoon of 10 October 2022. The survey transect extended from a point located 2 m south of the glacier edge to the approximate center of the glacier. A reference location was set up on the exposed rock next to CG, shown as location "1, 12" of Figure 2.3.a. The first and last gravity measurements were made at this base station to allow for relative corrections throughout the survey (see section 3.2).

During a two hour period, a total of twelve gravity readings were recorded over 450 m traversing the straightest path which could be safely crossed from the base station at the edge extending towards the center. For each measurement the gravity meter was placed on a metal plate dug a few centimeters into the ice. In addition to the gravity readings, the time, GPS location, and altitude were recorded at each spot (see supplementary material Table S1.1). The relative horizontal and vertical positions

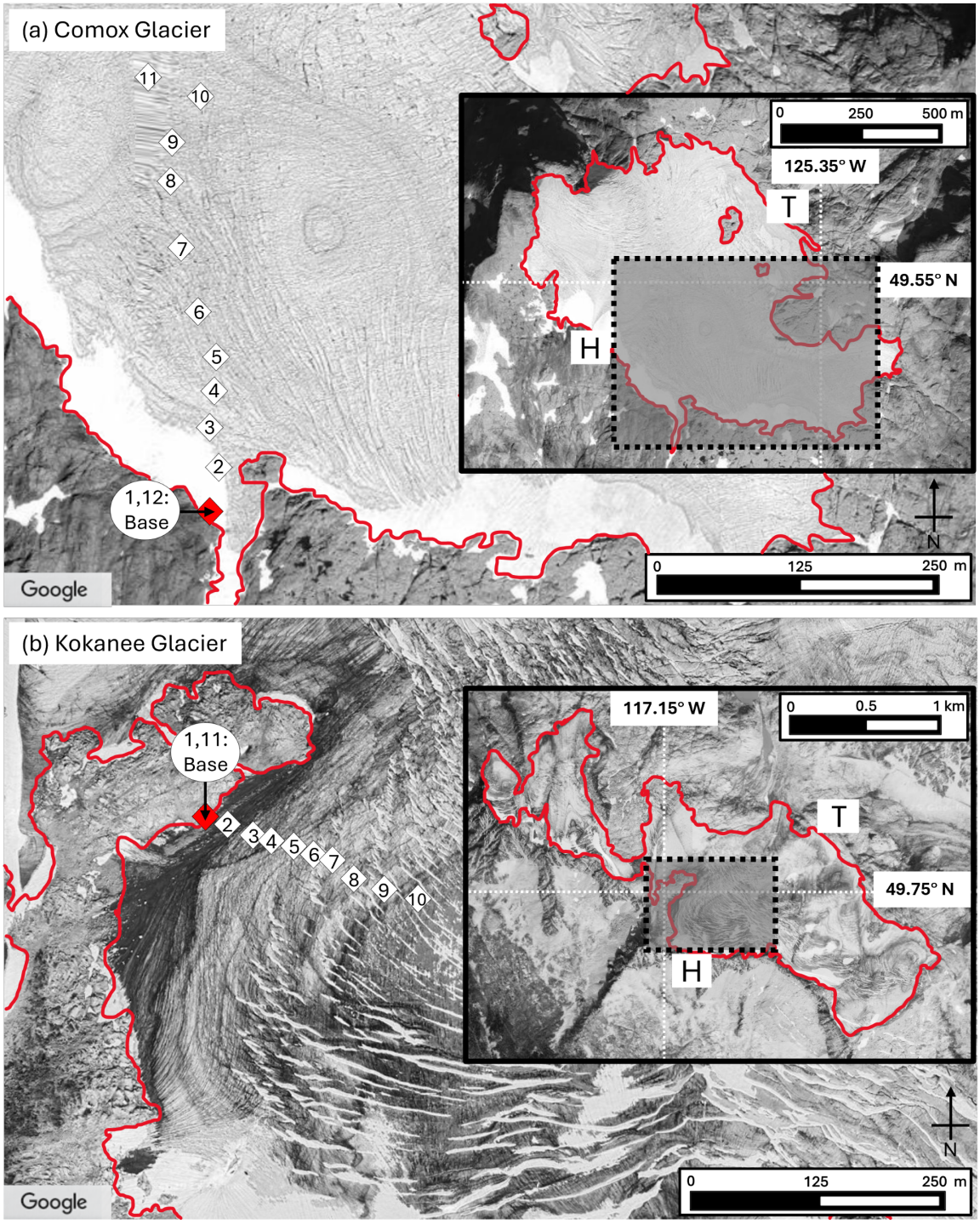

Figure 2.3: Survey measurement locations (diamonds) across the Comox Glacier (a) (Google Earth, Airbus, 30/09/2023) and the Kokanee Glacier (b) (Google Earth, Airbus, 08/09/2024). For both (a) and (b) the location of the larger image is given by the dashed line box in the inset map, which includes the full glacier extent, with the head and toe regions marked by H and T respectively.

of the measurement sites were then surveyed using a Spectra Precision Focus 6 5 in. Total Station and associated reflector prism.

To ensure consistency and that the apparatus was undamaged for the experiment, two extra measurements were also made near the University of Victoria before the experiment took place at 22:27 (PST) on 8 October, and directly after returning from location at 19:16 (PST) on 11 October (see supplementary material Table S1.1).

Kokanee Glacier

KG was accessed on the afternoon of 1 September 2023. The transect area was chosen on an approximately flat 220 m section on the upper part of the glacier, again extending from a base station on exposed rock approximately 3 m west from the glacier edge. The process of the experiment was completed nearly identically to that of Comox Glacier. In this experiment, however, a total of 11 measurements were made on the glacier (see supplementary material Table S1.1), and the Total Station was exchanged for a Bosch handheld 400 ft. laser rangefinder for measurements of relative height and distance along the transect. Again, the first and last measurements, labeled "1, 11" in Figure 2.3.b, were made at the base station, and for consistency extra measurements were made before and after the survey for comparison.

2.3.3 Summary of data reduction and density model

To isolate the local Bouguer anomaly resulting from the near-surface density structure, and thus enable the approximation of ice thickness, the corrections of section 2.2.3 were made to both sets of gravity data. As stated, beyond the subtraction of the base station measurement to achieve a relative gravity measurement from zero ice depth, the data at each point was adjusted for the effects of solid Earth tides, linear drift from gravity meter spring creep, latitude, elevation (free air correction), the Bouguer plate correction, and the local terrain (Appendix A).

For the preliminary corrections, manufacturer instructions specific to the LaCoste & Romberg Model G were followed to convert gravity readings to units of mGal [1]. Tidal corrections were further calculated through a MATLAB program produced by Samantha Palmer with equations based on Schureman [19] and compiled by Longman [20].

For both the terrain and Bouguer plate corrections a rock density of 2.89±0.16 g cm^{-3}, associated with the predominant basalt of the Karmutsen formation sur-

Table 2.1: Bouguer gravity anomaly values (δg^{boug}) and inferred glacier ice thickness ($Tck.$) for Comox and Kokanee glaciers.

$Pt.$	1	2	3	4	5	6	7	8	9	10	11	12
$\delta g^{boug,CG}$ $\pm 0.15(mGal)$	0.00	-0.62	-0.86	-1.01	-2.44	-3.40	-2.97	-2.68	-3.13	-3.05	-3.02	0.00
CG $Tck.$ $\pm 2(m)$	0	4	7	3	35	57	36	30	46	45	45	0
$\delta g^{boug,KG}$ $\pm 0.12(mGal)$	0.00	-2.18	-2.71	-2.90	-3.22	-3.34	-3.20	-3.47	-3.42	-3.29	0.00	-
KG $Tck.$ $\pm 2(m)$	0	31	42	44	51	55	50	53	56	51	0	-

rounding CG, and 2.67±0.08 g cm^{-3}, associated with the predominant granite and granodiorite makeup of the Nelson batholith surrounding KG, were used [29, 30]. These density values are the average saturated bulk density of, respectively, Karmutsen basalt samples and British Columbia granite and granodiorite samples as documented in the Canadian Rock Physical Property Database [29]. For both glaciers the terrain corrections were calculated using GTeC software [22] alongside the Province of British Columbia Terrain Resource Information Management 1:20,000 topographic dataset at a pixel size of 2 m and elevation grid of 25 m [23]. A radius of 7 km was used around each measurement station, with gravity corrections compiled over the area with step size increasing from 25 m to 2 km in distance from each station.

Density model

Final determination of the ice thickness across CG and KG transects was inferred through gravity modeling with GravMag software (Table 2.1, Figure 2.4) [2]. The software calculates the gravity contribution of a 3-D ice body of given dimensions (represented in 2-D as adjoining polygons) relative to underlying and adjacent rock, for comparison with the observed Bouguer gravity anomaly. The assumed homogeneous ice density is 0.917 g cm^{-3}, and rock densities are as defined above for the CG and KG study areas, such that the ice body is assigned a density contrast of -1.97±0.16 g cm^{-3} and -1.75 ±0.08 g cm^{-3} for CG and KG respectively [29, 30].

The glacier width parallel to the survey transect is constrained by the satellite imagery and the modeling assumes uniform continuation of the ice body in the perpendicular directions. In each case the dimensions of the ice body were therefore varied in order to minimize the root mean square error (RMSE) misfit between the observed and model-predicted values. Once the RMSE misfit was minimized for each model, the inferred ice thickness at each measurement was recorded (Table 2.1). Error for the inferred depths was taken by adjusting the models to match the recorded data when the gravitational anomaly uncertainties had been added or subtracted.

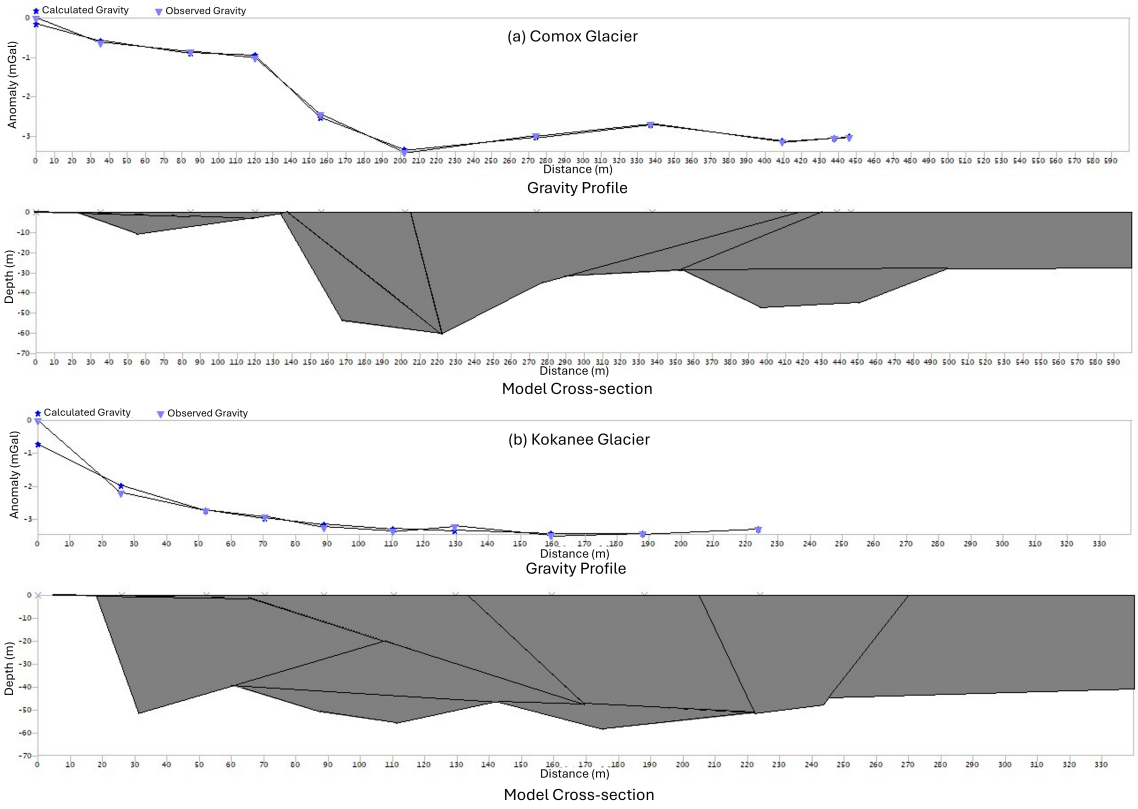

Figure 2.4: GravMag density structure model of ice thickness across Comox (a) and Kokanee (b) Glaciers, providing a best fit to the measured Bouguer gravity anomaly data [2]. The top panel of each sub-figure is the observed gravity (triangles) verses distance distance along the transect, plotted alongside the calculated gravity (stars) produced by the structure in the lower panel. For the model in the bottom panel, the white region indicates area of expected rock, while the grey bodies indicates the present ice.

2.4 Summary of the study

2.4.1 Results

The determined local Bouguer anomaly values along each transect are listed in Table 2.1. Calculation of the relative gravity across the CG transect shows a gradual decrease for the first 130 m extending from the base station, at which point the gravity drops to an average of -2.95 ± 0.18 mGal relative to the base station (Figure 2.4.a). Forward modeling with the GravMag software inferred an ice thickness of less than 10 m within the first 130 m the transect, after which the thickness increased to an average of 42 ± 4 m, with an RMS misfit of 0.064 mGal between the observed and simulated gravitational data. For this transect of CG a maximum depth of 57 ± 2 m was obtained just over 200 m north from the base station and 250 m south of the center of the glacier (point 6-7, Figure 2.3.a).

Completing the same analysis for the as with CG, the Bouguer gravity profile across KG shows a steady decrease from the base station. The profile further levels out after approximately 50 m to a low of -3.19 ± 0.13 mGal relative to the base station (Figure 2.4.b). Modeling the negative gravity anomaly with the GravMag software provided an RMS misfit for the simulated gravity in comparison to the measured data of 0.24 mGal, inferring a range and average ice thickness for the leveled central region of the transect of 42 - 56 ± 2 m and 50 ± 3 m respectively (points 3-10, Figure 2.3.b).

2.4.2 Method limitations

It is possible that our inferred ice thickness profiles under- or over-estimate the true glacier thickness, due to necessary simplifying assumptions. The modeled value for the glacier density assumes a homogeneous ice body, when in fact the glacier contains some volume of sediment and meltwater (both denser than ice) as well as air-filled crevasses (less dense than ice). We assume that these volumes are relatively insignificant and that they mostly cancel each other out. Adding such features to the model may enable a different ice thickness profile that equally well fits the data, but the inclusion of unconstrained complexities is not warranted. Additional sources of uncertainty include the assumption of homogeneity of the adjacent rock density, as well as the choice of total area and grid size for the terrain corrections.

Our study is somewhat limited in that only one transect was surveyed for each glacier. However, since each transect crosses the main trunk of the glacier in the

midstream section, the measured gravity anomaly results partially from the density structure in the adjacent up- and downstream directions, as well as directly along the transect. Modeling then enables approximation of an ice thickness profile that is spatially averaged in the up- and downstream directions.

2.4.3 Ice thickness comparison

For the Comox Glacier, our determination of ice thickness provides the first measurement that can be used in regional or global modeling efforts (e.g., [31]) and to serve as a baseline value to enable monitoring of future change, but there are no previous estimates for comparison. The ice thickness values determined here for the Comox Glacier (mean 42 $\pm$ 4 m; maximum 57 $\pm$ 2 m) are consistent with those measured in glaciers of comparable area. A 2020 study by Pandit and Ramsankaran on 65 glaciers in Chandra Basin of the Himalayas reported eight glaciers of similar surface area to the CG (<2.0 km^2), all with mean ice thickness in the range 27 to 59 m, and maximum thickness between 61 and 158 m [32]. Glaciers of the same study with slightly larger surface areas (2.0-8.0 km^2) generally had a mean thickness marginally deeper, between approximately 40 and 80 m, while the few covering the biggest areas (>8.0 km^2) typically measured greater than 100 m in thickness.

The Kokanee Glacier was previously extensively surveyed using ice penetrating radar [3]. That study measured ice thickness up to 88 m, with an average of 48 m, consistent with the 50 $\pm$ 3 m average determined for our gravity transect. Our estimated uncertainties at 6-10% are also similar to those estimated for the ice-penetrating radar-derived ice thicknesses (5.2-10.4%; [3]) and for gravity studies of other glaciers (e.g., [16]; [17]). Figure 2.5 shows a comparison of the ice thickness transect inferred from our gravity survey with nearby values determined by [3]. Although much of the transect matches well with previous trends in the area, it is seen that there is a slight over- and underestimation of ice thickness at either end of the gravity survey transect. While this could be due to changes in the ice thickness in the time between each survey, it could also be explained by the gravity survey measurements implicitly averaging all features in the local area, and not just those at precisely the point of measurement. For example, it is seen that [3] witnessed a short decrease in ice thickness from 60-80 m to 40-60 m just beyond the end of the gravity transect. This feature, in combination with ice melt, could account for why the end of the gravity survey transect was inferred at more shallow ice thickness. Accepting these few dif-

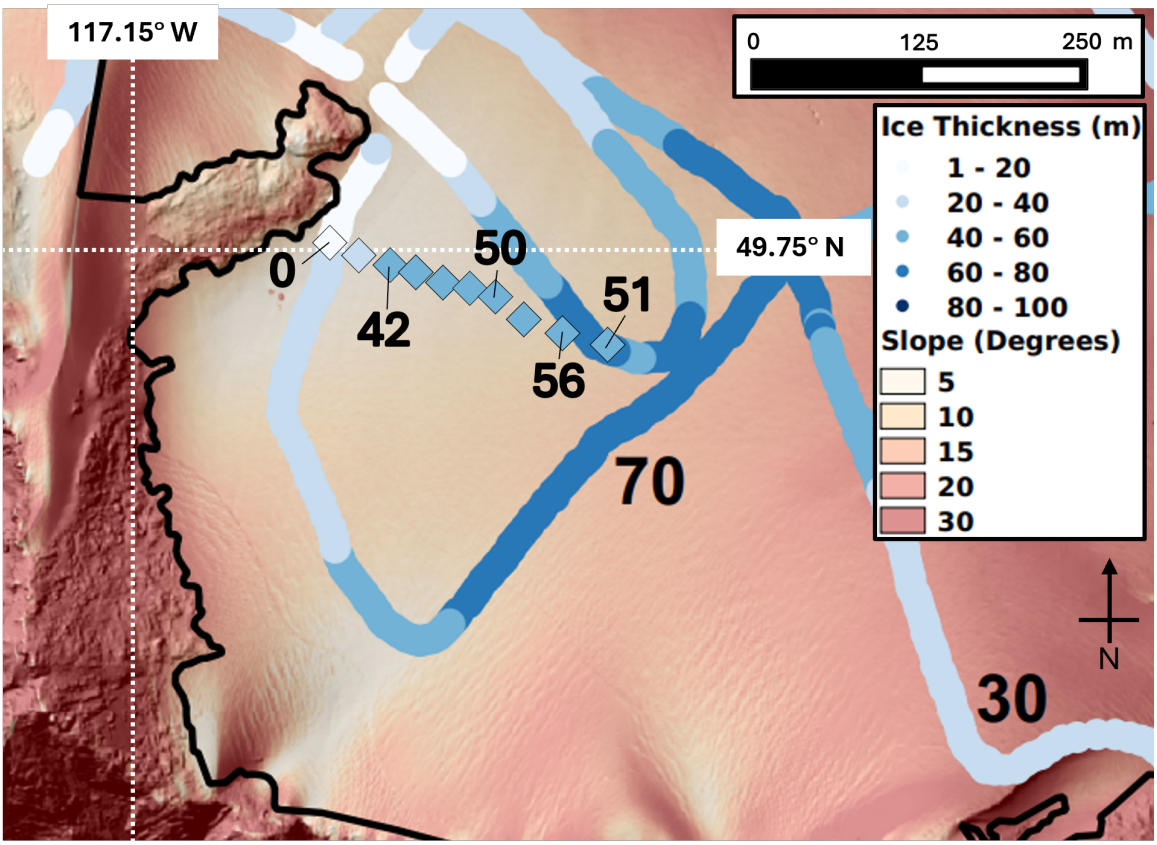

Figure 2.5: Gravity survey results (diamonds) imposed overtop of the data and figure determined by [3] for the same region of Kokanee Glacier. The gravity survey data has been coloured to match that of the previous work, with the thickness of several points provided alongside.

ferences, the similar values and trend derived from two independent methods applied to the Kokanee Glacier thus verify that a gravity survey can enable a good first-order approximation of glacial ice thickness, and provide confidence in our results for the Comox Glacier too, despite a lack of direct groundtruthing data.

2.5 Gravity survey conclusions

Collection and modeling of gravity survey data along transects across the Comox and Kokanee Glaciers has enabled determination of average ice thicknesses of 42 $\pm$ 4 m and 50 $\pm$ 3 m, respectively. This study provides the first ice thickness measurement for the Comox Glacier, to serve as a baseline to which future measurements can be compared, and to inform decisions around water resource management in the Comox

Valley watershed. The ice thickness profile of the Kokanee Glacier was found to be consistent with previous measurements obtained using ice penetrating radar, and the thickness of both glaciers was found to be comparable to other systems of similar sizes.

Gravity surveying, while not a commonly applied technique in recent glacier studies, is demonstrated here to be a viable and cost-effective method for the estimation of glacial ice thickness to within 5-10%. If applied more widely, it has the potential to significantly add to the global ice thickness database. Such data are critically needed to constrain regional and global assessments of glacial ice volumes and their changes over time, with implications for water supply, glacioisostatic adjustment, and relative sea level change (e.g., [31]; [33]; [34]).

Chapter 3

The Anderson Model via Random Matrices

3.1 Focus of the analysis

Identifying and characterizing the chaotic nature of a quantum system remains an important topic of research for many areas including condensed matter physics, statistical physics, and high-energy physics [35, 36, 37]. Focusing on the Hamiltonian of a given system, in many cases when written in a non-fine-tuned basis it appears random. Moreover, statistics typical of random matrix ensembles have been known to emerge throughout a wide variety of physics, and are often associated with qualities of chaotic behavior, diffusion, and eigenstate thermalization [38]. Random matrix theory (RMT) is thus an important tool for both characterizing when phenomena such as chaos happen, as well as when it is likely absent. For the latter case, when RMT statistics break down, this is often associated with the occurrence of localization [39, 40].

One model that has previously been considered through the lens of RMT is the Anderson model [41]. The system is generally given by a lattice with random potentials applied on each site, where non-interacting particles are allowed to hop from one site to the next. As a quadratic fermionic model, quantum chaos may be defined in this context by the appearance of random amplitudes appearing within the single-particle eigenfunctions of the Hamiltonian [41]. In 2, 3, and higher dimensions, while varying the disorder supplied to the system, quantum chaos is seen to be present but greatly suppressed in finite systems, and absent for any non-zero disorder in the ther-

modynamic limit [42, 39]. That is, interference on the eigenfunction caused by the potentials works to limit any chaotic behavior. In this case, localization in position space or quasi-momentum space of the eigenstates becomes exponentially likely, with localization absolute in the thermodynamic limit for any non-zero potentials [42, 39].

In 1D, and the focus of this study, localization of the eigenstates in position space is similarly seen at zero disorder strength, while localization in quasi-momentum space is had for any non-zero potentials, in the thermodynamic limit [43, 44, 45]. In finite systems, however, although there is no true chaotic regime, non-zero disorder has been seen to produce localization in both position and quasi-momentum space with a so-called "localization-to-localization" crossover [41]. As much of the previous work in this area has been completed using uniform (UN) random potentials one question that can be asked is how the physics differ when using correlated disorder defined through a random matrix ensemble? That is, how, if at all, does the change to a completely correlated system of potentials affect the 1D Anderson model with respect to localization, the presence of chaos, and scaling?

In this chapter the Anderson model will therefore be studied on a periodic chain in 1-dimension, with correlated disorder given through the eigenvalues of the Circular Unitary Ensemble (CUE). Behavior of the spectral statistics, quantum quench dynamics, many-particle eigenstate entanglement entropy, and inverse participation ration will be explored after the introduction to the model and an analysis through perturbation theory. In each section, comparisons will be made against the work by reference [41], which completed a similar analysis under uniform disorder. Additionally, preliminary observations for the 2D Anderson model through spectral statistics of the single particle sector will be shown.

3.2 Preliminaries

3.2.1 Random matrix disorder

Before providing a definition to the Anderson model, a short discussion of the random matrix ensemble used to construct the system, and how it provides the disorder, is given here. With some previous work in literature having taken place using the CUE, it has been chosen as the desired random matrix ensemble to pull from here when constructing the Hamiltonian ensemble [46]. A wide variety of other ensembles could have been chosen, however, and therefore much of the discussion here applies to the

Circular Orthogonal Ensemble (COE) as well as Circular Symplectic Ensemble (CSE).

Let U_β be an $L_\beta \times L_\beta$ random unitary matrix (given by the Haar measure acting on the unitary group $U(n)$) with eigenvalues $\lambda_j = \exp(i\theta_j)$ where $\theta_j \in [-\pi, \pi)$. For the circular ensembles, the eigenvalues are governed by the joint probability distribution ([38]; [46])

$$\begin{aligned} P(\theta_1, \cdots, \theta_L) &= \frac{1}{Z_{L,\beta}} \prod_{1 \le j < k \le L} \left| e^{i\theta_j} - e^{i\theta_k} \right|^\beta \\ Z_{L,\beta} &= (2\pi)^L \frac{\Gamma(L\beta/2 + 1)}{[\Gamma(\beta/2 + 1)]^L} \end{aligned} \tag{3.1}$$

where $\beta = 2$ for the CUE.

From this it is clear that for $P(\vec{\theta})$ to be non-zero, no two angles θ_j will be degenerate. Moreover, the set of θ_j are completely correlated under $P(\vec{\theta})$ through this level repulsion. With each realization of the CUE, a set $\mathcal{J}$ of L non-degenerate correlated real potentials is therefore supplied, which when averaged over the ensemble spread out over the unit circle at spacing $\sim 1/L$.

3.2.2 Defining the model

For this study a system of fermions hopping on a 1-dimensional lattice of size L is taken with random correlated potentials applied on each site and periodic boundary conditions (PBC). Under the Hamiltonian formalization, this is defined here by the Anderson model as:

$$H = \sum_{j=1}^{L} \left[\theta_j \hat{n}_j - J \left(c_j^\dagger c_{j+1} + \text{h.c.} \right) \right] \tag{3.2}$$

where c ($c^\dagger$) are fermion annihilation (creation) operators, $\hat{n}_j = c_j^\dagger c_j$ are number operators, J is the hopping amplitude, and θ_j are the random correlated fields (disorder) drawn from $L \times L$ matrices of the CUE. For this study the disorder strength will be limited to $[-\pi, \pi)$, and the hopping amplitude will be varied in order to observe the effects of correlated disorder.

For the purposes of the spectral statistics (to be defined) and notation, a form

similar to a Fluoqet picture is taken where $\mathcal{U} = \mathcal{U}_1\mathcal{U}_2$ as

$$\begin{aligned} \mathcal{U}_1 &= \exp\left[-i\sum_{j=1}^{L}\theta_j\hat{n}_j\right] \\ \mathcal{U}_2 &= \exp\left[iJ\sum_{j=1}^{L}\left(c_j^\dagger c_{j+1} + \text{h.c.}\right)\right] \end{aligned} \tag{3.3}$$

Although not equivalent to the individual on-site or hopping term of the Hamiltonian, for ease of communication when referring only to a dominant term $\mathcal{U}_1$ and $\mathcal{U}_2$ will be used for brevity.

With many samplings of the CUE an ensemble of Hamiltonians is therefore produced. In each disorder realization H takes a block diagonal form in the fermion occupation basis due to conservation of fermion number. As an example, in a trivially small case where $L = 3$ we have constructed the matrix:

$$H = \begin{bmatrix} \theta_1 & J & J \\ J & \theta_2 & J \\ J & J & \theta_3 \end{bmatrix} \bigoplus \begin{bmatrix} \theta_1+\theta_2 & J & J \\ J & \theta_2+\theta_3 & J \\ J & J & \theta_3+\theta_1 \end{bmatrix} \bigoplus \Big[\theta_1+\theta_2+\theta_3\Big] \tag{3.4}$$

The diagonal elements of the n^{th} sector are constructed from the L potentials of the single particle sector.

This symmetry allows the partition of the Hilbert space $\mathcal{H}$ into sectors $\mathcal{H}_N$ with a fixed fermion number $N \in [0, L]$. The total space is thus $\mathcal{H} = \bigoplus_{n=0}^{L}\mathcal{H}_N$ with dimension $\mathcal{D}$ where $\mathcal{H}_N$ has dimension $d_N = \binom{L}{N}$ and

$$\sum_{n=0}^{L} d_n = 2^L \equiv \mathcal{D} \tag{3.5}$$

In addition to this, in order to reduce the complexity of some numerical calculations a particle-hole structure is noted within the Hamiltonian definition. That being the diagonal elements of particle sector $L/2-n$ given by $\sum_{q\in\mathcal{Q}}\theta_q$ for some set $\mathcal{Q} \subseteq \mathcal{J}$ are related to those of particle sector $L/2+n$ by $\sum_{j\in\mathcal{J}}\theta_j - \sum_{q\in\mathcal{Q}}\theta_q$. With respect to the Hamiltonian, introducing operator $\mathcal{P}$ which swaps all single fermion states and

vacuum states like

$$\begin{aligned} &\mathcal{P}\left|0\right\rangle = \left|1\right\rangle, \quad \mathcal{P}\left|1\right\rangle = \left|0\right\rangle \\ &\text{or} \\ &\mathcal{P}\left|01\right\rangle = \left|10\right\rangle, \quad \mathcal{P}\left|01\right\rangle = \left|10\right\rangle \end{aligned} \tag{3.6}$$

it is seen that the fermion operators are transformed via

$$\begin{aligned} \mathcal{P}c\mathcal{P} &= c^\dagger \\ \mathcal{P}c^\dagger\mathcal{P} &= c \\ \mathcal{P}\hat{n}\mathcal{P} &= 1-\hat{n} \end{aligned} \tag{3.7}$$

From these relations, it follows that H satisfies

$$\mathcal{P}H\mathcal{P} = \sum_{j=1}^{L}\Big[\theta_j(1-\hat{n}_j) + J(c_j^\dagger c_{j+1} + \text{h.c.})\Big] \tag{3.8}$$

and many-particle sectors H_N may be efficiently constructed from their particle hole partner. Additionally, this structure allows one to see that much of the statistics associated with a particle sector will closely mirror those of its partner.

Finally, perhaps the most important aspect of the Anderson model for the work here is that it is quadratic in fermion operators, and therefore there exists a basis which the system decomposes into non-interacting fermions [47, 48]. For calculation of certain statistics, specifically the many-particle entanglement entropy, the creation, annihilation, and diagonalizing matrix will be defined as follows. Taking $\hat{H} = \boldsymbol{c}^\dagger H \boldsymbol{c}$ where $\boldsymbol{c}^\dagger$ ($\boldsymbol{c}$) are vectors of fermion operators in the standard basis (i.e. $\boldsymbol{c} = [c_1, c_2, \ldots, c_L]$), a diagonalized form D can be found by

$$\begin{aligned} \hat{H} &= \boldsymbol{c}^\dagger U U^\dagger H U U^\dagger \boldsymbol{c} \\ &= \boldsymbol{b}^\dagger D \boldsymbol{b} \end{aligned} \tag{3.9}$$

where U is some unitary matrix and $\boldsymbol{b}^\dagger = \boldsymbol{c}^\dagger U$ ($\boldsymbol{b} = U^\dagger \boldsymbol{c}$). In this basis the Hamiltonian of free fermions is thus $\hat{H} = \sum_j \epsilon_j b_j^\dagger b_j$ with ϵ_j the energy of each free particle. Notably, for the many-particle sectors this means that their eigenstates $\left|n\right\rangle$ and energies are described by a population of the non-interacting single particle eigenstates $\left|\alpha\right\rangle$ and energies ϵ_α.

With all many-particle correlations understood in terms of the single particle energies and states, the task of calculation is greatly reduced. Despite this, some

statistics are not self averaging (i.e. do not follow the central limit theorem) [49]. A great number of disorder realizations may therefore be required to see the ensemble behavior. As will typically be done throughout this work, averaging over a set of states will be defined by $\langle ... \rangle_\alpha$ or the ensemble of Hamiltonians as $\langle ... \rangle_H$.

3.2.3 Perturbation theory

In order to characterize the behavior of the Anderson model with correlated disorder, and contrast it to similar work using UN disorder, scaling collapses in the hopping amplitude J and system size L will be searched for throughout the statistics. Also, because many real physical systems are not truly in the thermodynamic limit, information for real systems may be provided through these re-parameterizations. An easy method to achieve leading order approximations in various limits is perturbation theory. Perturbations to the limiting $J \to 0, \infty$ cases are therefore provided here for the first few terms.

Limit: $J \to 0$

For $J = 0$, the single-particle eigenstates are just the position eigenstates: $H_{J=0} |\alpha\rangle^0 = \theta_j |j\rangle$ where $E_j^0 = \theta_j$ is the unperturbed energy. Since $\theta_j \neq \theta_i \forall\ i, j$, the energies and states are considered non-degenerate. The first order energy and eigenstate corrections are then

$$\begin{aligned} E_j^1 &= \langle j | J \sum_p c_p^\dagger c_{p+1} + \text{h.c.} \, |j\rangle = 0 \\ |\alpha\rangle^1 &= \frac{J}{\theta_j - \theta_{j+1}} |j+1\rangle + \frac{J}{\theta_j - \theta_{j-1}} |j-1\rangle \end{aligned} \tag{3.10}$$

where the leading order energy shifts have vanished. At second order the corrections are then of $\mathcal{O}(J^2)$. For the state this will be taken as a negligible correction when determining first approximations. To demonstrate that not all energy corrections are 0 in this limit, it is easily calculated at second order that

$$\begin{aligned} E_j^2 &= \sum_{n \neq j} \frac{\left| \langle n | J \sum_{m=1}^L \left(c_m^\dagger c_{m+1} + \text{h.c.} \right) |j\rangle \right|^2}{E_j^0 - E_n^0} \\ &= J^2 \left(\frac{1}{\theta_j - \theta_{j+1}} + \frac{1}{\theta_j - \theta_{j-1}} \right) \end{aligned} \tag{3.11}$$

where corrections of higher even order $2m$ find contribution $\mathcal{O}(J^{2m}/\delta_{j\pm n,j}^{2m-1})$ with $\delta_{j\pm n,j} = \theta_j - \theta_{j\pm n}$.

Perturbation theory therefore predicts that the small J energy shifts scale as $[J^2/\delta_{j\pm1,j}] + [J^4/\delta_{j\pm1,j}^3]$. The small J single-particle level spacing $\delta_{j\pm1,j}$ is thus set by the applied order of θ_j. By the probability distribution of section 3.2.1, it is given that level repulsion will separate nearest random unitary quasi-energies of the CUE (δ_{CUE}) as $\theta_\alpha - \theta_{\alpha\pm1} \approx 1/L$. Therefore, as $\delta_{j\pm1,j} \geq \delta_{CUE}$, by E_j^1 these small J limit corrections are expected to be negligible when $J^2 \lesssim \delta_{CUE}$. Rather, the small J limit is certain for $J \lesssim 1/\sqrt{L}$. With the random potentials dominating in this regime, it is expected that statistics like the level spacing will follow that of the CUE, and the system can be effectively considered as $\mathcal{U}^1$.

Finally, the perturbative corrections largely take the same form when considering a higher dimensional lattice, where indices $j, j+1$ are exchanged with i, j for nearest neighbor hopping. Therefore, for a d-dimensional cubic lattice this result is exchanged with the small hopping limit provided below $J \lesssim 1/L^{d/2}$. When extending the problem into two dimensions on an $L \times L$ lattice (section 3.4) it is predicted that CUE statistics will be found for $J \lesssim 1/L$.

Limit: $J \to \infty$

For the large $J \to \infty$ limit the Hamiltonian is reduced to only the hopping of $\mathcal{U}_2$, and the disorder term drops out. The eigenstates are then localized in momentum space ($|k\rangle$), which can be related back to the standard spatial basis through a Fourier transform as [41, 50]:

$$|k\rangle^0 = \frac{1}{\sqrt{L}} \sum_{j=0}^{L-1} e^{-2\pi i k j/L} |j\rangle \tag{3.12}$$

where $k \in [0, L-1]$, and the zeroth order energy perturbation is

$$H_{J\to\infty} |k\rangle = -2J \cos\left(\frac{2\pi k}{L}\right) |k\rangle, \quad E_k^0 = -2J \cos\left(\frac{2\pi k}{L}\right) \tag{3.13}$$

For simplicity L is even here, accepting small changes when L is odd. With cosine being an even function, it is seen that $k = 0, L/2$ corresponding to $E_k^0 = \pm 2J$ are the only non-degenerate momenta. The rest are two fold degenerate such that $k = m$ provides the same solution as $k = L - m$ for integer m.

This degeneracy is thus taken into account when computing the first order cor-

rections, where now the CUE disorder term in $\mathcal{U}_1$ is taken as the perturbation. For degenerate perturbation theory, first order energy corrections can be found by diagonalizing the subspace of the matrix W formed by the zeroth order states acting on the perturbation. That is,

$$\begin{aligned} W_{k,l} =& \langle k| \sum_{p=1}^{L} \theta_p \hat{n}_p |l\rangle \\ =& \frac{1}{L} \sum_{p,j,m} \theta_p \exp[2\pi i(jk - ml)/L] \langle j| \hat{n}_p |m\rangle \\ =& \frac{1}{L} \sum_{j=0}^{L-1} \theta_j \exp[2\pi ij(k-l)/L] \end{aligned} \tag{3.14}$$

with degenerate subspaces W^s given by

$$W^s_{k,l} = \begin{pmatrix} \sum_j \theta_j/L & \sum_j \theta_j e^{-4\pi ijk/L}/L \\ \sum_j \theta_j e^{4\pi ijk/L}/L & \sum_j \theta_j/L \end{pmatrix} \tag{3.15}$$

The degenerate spectrum corrected to first order is therefore

$$E_k = -2J\cos\left(\frac{2\pi k}{L}\right) + \sum_{j=0}^{L-1} \frac{\theta_j}{L} \pm \left(\sum_{j,l=0}^{L-1} \frac{\theta_j \theta_l}{L^2} \exp\left(\frac{-4\pi k(j-l)}{L}\right)\right)^{1/2} \tag{3.16}$$

or $E_k = \pm 2J + \sum_{j=0}^{L-1} \theta_j/L$ for the two non-degenerate states ($k = 0, L/2$). Focusing on the last term of the degenerate states, it may be simplified further by

$$\begin{aligned} &\left(\sum_{j,l=0}^{L-1} \frac{\theta_j \theta_l}{L^2} \exp\left(\frac{-4\pi k(j-l)}{L}\right)\right)^{1/2} \\ &= \frac{1}{L}\left(\sum_{j=0}^{L-1} \theta_j^2 + \sum_{0\le j<l\le L-1} 2\theta_j\theta_l \cos\left(\frac{4\pi k(j-l)}{L}\right)\right)^{1/2} \end{aligned} \tag{3.17}$$

Although higher order perturbations could also be calculated, use of the momentum states alone gives the appropriate scaling in J when applied in future work (section 3.3.3). Focus is therefore limited to these first terms for the remainder of the discussion.

Eq. (3.16) may be reduced further by noting that $\theta_j \in [-\pi, \pi)$ are spaced around the unit circle at distance $\delta_{j+1}, j = 1/L$, i.e. due to level repulsion, one can approxi-

mately use $\theta_j \approx -\pi + 2\pi j/L$ where $j \in [0, 1. \ldots, L-1]$. On average the sum of the on site potentials is

$$\langle \theta \rangle \approx \sum_{j=0}^{L-1} -\pi + \frac{2\pi j}{L} = 0 \tag{3.18}$$

and their variance is

$$\begin{aligned} \langle \theta^2 \rangle &\approx \sum_{j=0}^{L-1} \left(-\pi + \frac{2\pi j}{L} \right)^2 \\ &= \frac{\pi^2 L}{3} - \pi^2 + \frac{4\pi^2}{3L} \end{aligned} \tag{3.19}$$

Inputting these into Eq. (3.16), and assuming L is large enough such that $\pi^2 L/3 >> \pi^2, 4\pi^2/3L$ the energy in the large J limit is

$$E_k \approx -2J \cos\left(\frac{2\pi k}{L}\right) \pm \frac{1}{L} \left(\frac{\pi^2 L}{3} + \sum_{0 \le j < l \le L-1} 2\theta_j \theta_l \cos\left(\frac{4\pi k (j-l)}{L}\right) \right)^{1/2} \tag{3.20}$$

Without calculating an ensemble average for $\langle \theta_j \theta_k \rangle$, it is clear that the terms of the remaining sum will at least partially cancel, leaving only a term of $\mathcal{O}(1/\sqrt{L})$. Alternatively, taking an extreme case where all $\theta_j \theta_k \approx \pi^2$, i.e.

$$\sum_{0 \le j < l \le L-1} 2\theta_j \theta_l \cos\left(\frac{4\pi k (j-l)}{L}\right) < 2\pi^2 \sum_{0 \le j < l \le L-1} \cos\left(\frac{4\pi k (j-l)}{L}\right) \tag{3.21}$$

then

$$\begin{aligned} 2\pi^2 \sum_{0 \le j < l \le L-1} \cos\left(\frac{4\pi k (j-l)}{L}\right) &= 2\pi^2 \sum_{j=1}^{L-1} (L-j) \cos\left(\frac{4\pi k j}{L}\right) \\ &= 2\pi^2 \Re \left[\sum_{j=1}^{L-1} (L-j) \exp\left(i \frac{4\pi k j}{L} \right) \right] \end{aligned} \tag{3.22}$$

where, recognizing a geometric series is formed and taking $\exp(4\pi i k/L) = x$, the sum is given as

$$\begin{aligned} \Re \left[L \sum_{j=1}^{L-1} x^j \right] &= \Re \left[L \left(-1 + \sum_{j=0}^{L-1} x^j \right) \right] \\ &= \Re \left[-L + L \frac{1 - x^L}{1 - x} \right] \\ &= -L \end{aligned} \tag{3.23}$$

and

$$\begin{aligned}\Re\left[\sum_{j=1}^{L-1} jx^j\right] &= \Re\left[x\frac{\mathrm{d}}{\mathrm{d}x}(-1+\sum_{j=0}^{L-1} x^j)\right] \\ &= \Re\left[-\frac{L}{1-x}\right] \\ &= \frac{L}{2\cos(4\pi k/L)}\end{aligned} \tag{3.24}$$

Even without assuming any interference of $\theta_j\theta_k$, the perturbed energy in the large J limit seems to go like

$$E_k \approx -2J\cos\left(\frac{2\pi k}{L}\right) \pm \mathcal{O}\left(\frac{1}{\sqrt{L}}\right) \tag{3.25}$$

Therefore, with L states spread within a range $\mathcal{O}(J)$ when the J dependent term dominates, the large J limit for the spectral scaling in L will be found for $J/L \gtrsim 1/\sqrt{L}$, or rather $J \gtrsim \sqrt{L}$. This also matches the previous prediction for UN disorder, as will be indicated by Figure 3.1 in Section 3.3.1 [41].

3.3 Statistics in 1D

Observations on the behavior, scaling collapses throughout the statistics, and how they relate to uniform disorder explored by [41] are presented and discussed here. The spectral statistics of the single particle sector are initially explored, followed by the single particle quantum quench dynamics, the inverse participation ratio and variance, and finally the many-particle entanglement entropy. In each case the statistic will be defined first along with any expectations. Data drawn from the ensemble will then be presented and discussed.

3.3.1 Single particle spectral statistics

With many random matrix ensembles achieving a unique distribution of quasi-energy level spacings, analysis of the nearest level difference within a given ensemble is an indicator of random matrix behavior [38, 51]. Importantly, ensembles like the Gaussian Orthogonal Ensemble (GOE) have level statistics which match that of many classical chaotic systems, and are therefore used as one way to look for quantum chaos [41, 51, 52]. As a numerically determined quantity here, the spectral statistics $\tilde{r}$ of

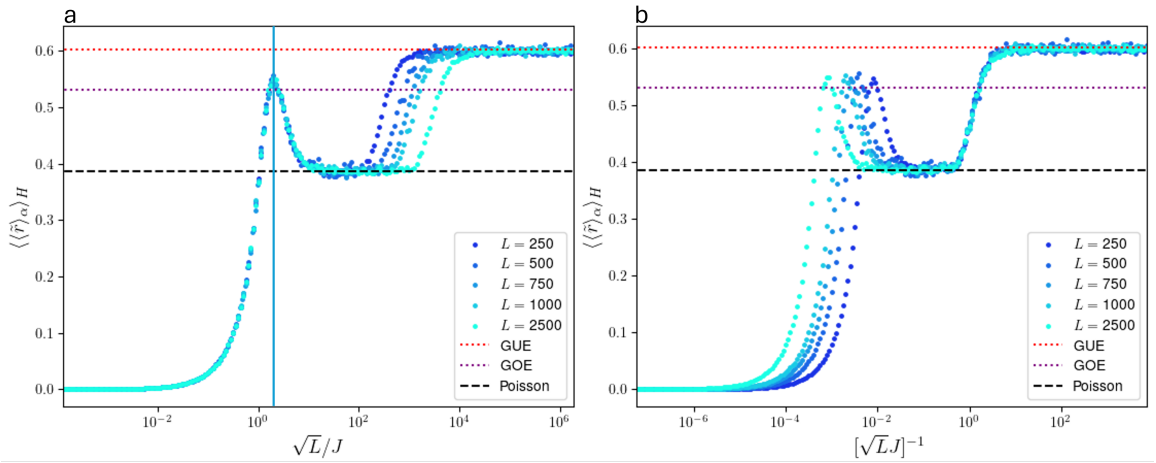

Figure 3.1: $\langle\langle\tilde{r}\rangle_\alpha\rangle_H$ over inverse hopping amplitude, $1/J$, for different chain lengths L of the 1D periodic CUE disordered Anderson model. In each case the hopping strength has been rescaled by powers of the system size $L^{\pm 1/2}$. Statistics typical of GUE, GOE, and Poisson systems are provided in each figure by the horizontal dotted/dashed lines. The critical hopping amplitude in the large J limit at the GOE peak is provided by the vertical blue line on the left hand side (a).

the Hamiltonian ensemble are taken as the ratio

$$\tilde{r} = \frac{\min[\delta_{\alpha,\alpha+1}, \delta_{\alpha-1,\alpha}]}{\max[\delta_{\alpha,\alpha+1}, \delta_{\alpha-1,\alpha}]} \tag{3.26}$$

where $\delta_{\alpha,\alpha+1}$ is the difference in consecutive energy levels $\epsilon_{\alpha+1} - \epsilon_\alpha$. At any point, the measured value observed is thus within $\tilde{r} \in [0, 1]$.

Thinking about the behavior of the Anderson model with varying hopping amplitude, via perturbation theory it is expected that the quasi-energies of the random unitaries from the CUE will dominate for $J \lesssim 1/\sqrt{L}$ in 1D. That is, particles will be nearly entirely localized in space. Plotting in terms of J^{-1} for consistency throughout future statistics, a scaling collapse is therefore predicted here by taking $J^{-1} \to (J\sqrt{L})^{-1}$. $\langle\langle\tilde{r}\rangle_\alpha\rangle_H$ is therefore expected to match that of a random unitary ensemble, known for the Gaussian unitary ensemble (GUE) at $\tilde{r}_{GUE} \approx 0.60266$ [51].

Moving beyond this small magnitude of J ($L^{-1/2} \lesssim J \lesssim L^{1/2}$), it is expected that the states will remain localized, but begin to spread out over some range of lattice sites. With this localized non-chaotic behavior typical of uncorrelated eigenstates, spectral statistics are likely to match that of a Poisson distribution, $\tilde{r}_P = 2\ln 2 - 1 \approx 0.3863$ [51, 52]. For large $J \gtrsim \sqrt{L}$ (localization in momentum space) the two fold degeneracy observed in perturbation theory is likely to drive $\langle\langle\tilde{r}\rangle_\alpha\rangle_H \to 0$. That is,

since pairs of momentum $|k\rangle, |-k\rangle$ differ only at $\mathcal{O}(\theta_j/L)$, the $\delta_{\alpha,\alpha+1}$ for $|k\rangle, |-k\rangle$ will likely be much less than the level spacing to the next pair.

Lastly, for systems with chaotic behavior typical of correlated eigenstates, as stated, level spacings typical of the GOE are seen at $\tilde{r}_{GOE} \approx 0.5359$ [51, 52]. While similar studies have shown this type of behavior is suppressed in the Anderson model, a crossover in $\langle\langle\tilde{r}\rangle_\alpha\rangle_H$ typical of $\tilde{r}_{GOE}$ has been witnessed with $\sqrt{L}/J$ scaling, and has been conjectured in the literature to be a highly universal feature of the model [41].

With respect to Figure 3.1.a and b, it is seen that the reasoning above accurately depicts the level spacing statistics for the 1D periodic Anderson model under CUE disorder. Taking $J^{-1} \to \infty$ moves $\langle\langle\tilde{r}\rangle_\alpha\rangle_H$ toward the level statistics given by that of the CUE (matching $\tilde{r}_{GUE}$). Similarly, taking $J^{-1} \to 0$ the level spacings go to 0. A Poisson plateau is additionally seen between the two regimes, with the localization-to-localization crossover occurring as expected from [41] under uniform disorder.

Highly accurate collapses are observed when re-scaling $1/J \to 1/(J\sqrt{L})$, or $\sqrt{L}/J$, as seen on either side of the Poisson plateau. While evidence of the $\tilde{r}_{GUE} \to \tilde{r}_P$ crossover is less visible in other statistics, the crossover through GOE statistics is present in some cases. Moreover, it has been seen that this peak is a highly universal feature of the 1D Anderson model. It is therefore denoted by the blue line in Figure 3.1.a, occurring at $J_{GOE} \approx \sqrt{L}/2$.

Finally, the level statistics in the thermodynamic limit can be extracted (i.e. L_∞). With the CUE plateau disappearing like $1/\sqrt{L}$, and the GOE peak increasing like $\sqrt{L}$, the Poisson regime will monotonically increase in size. That is, as the system size reaches large L the hopping amplitude will need to go to either ∞ or 0. It would therefore appear that in the thermodynamic limit the 1D Anderson model with CUE disorder achieves identical statistics to that of Uniform disorder for any $J \neq 0$. As expected, localization occurs at any finite J.

3.3.2 Quantum dynamics

With localization readily occurring for both finite and infinite L, here the dynamics of a particle in an initially (entirely) localized state are tested, observing how it (de)localizes in time with changes in system size and hopping amplitude. In detail, a quantum quench approach is taken with a particle initially prepared in the state $|j_0\rangle = c_0^\dagger |\emptyset\rangle$ where $|\emptyset\rangle$ is taken as the vacuum state and j_0 is the initial position of

the particle. As PBC are used, site $L/2$ on the chain was arbitrarily chosen. The particle is then time evolved in the standard way, with the new state at time t given by $|\psi(t)\rangle = e^{-iHt}\,|j_0\rangle$ [1].

To observe changes in the wavepacket occupation for each site throughout the chain, the weighted width of the state $|\psi(t)\rangle$ is measured by

$$\Sigma(t)^2 = \sum_{j=1}^{L}(j-j_0)^2\,\langle\psi(t)|\,\hat{n}_j\,|\psi(t)\rangle \tag{3.27}$$

Following [41], the ansatz is made where the particle dynamics are modeled via $\Sigma(t) \propto t^{1/z}$ where z is the dynamic exponent. For a particle acting in a ballistic nature (spreading out) it is expected that $\Sigma(t) \propto t$ (i.e. $1/z = 1$). Alternatively, a localized particle (retained to some set of physical sites) would cease to spread out over the chain, providing $1/z \to 0$. Acknowledging that in practice the $1/z$ will itself have some time dependence, from the previous ansatz the inverse of the dynamic exponent may be taken as:

$$\begin{aligned} z(t)^{-1} &= \frac{d\ln\Sigma(t)}{d\ln t} \\ &= \frac{t}{\Sigma(t)}\frac{d}{dt}\sqrt{\Sigma(t)^2} \\ &= \frac{t}{2\Sigma(t)^2}\frac{d}{dt}\Sigma(t)^2 \end{aligned} \tag{3.28}$$

Plotting this over time, instead of the wave packet occupation $\Sigma(t)$, provides a clear indication of the particle ballistic to localization behavior in position space as $z(t)$ changes.

Taking the results from perturbation theory, scaling collapses for some of the $z(t)^{-1}$ features can be retrieved prior to numerics in the small and large J limit. Considering the equation for the wavefunction width:

$$\begin{aligned} \Sigma(t)^2 &= \sum_{j=1}^{L}(j-j_0)^2\,\langle\psi(t)|\,\hat{n}_j\,|\psi(t)\rangle \\ &= \sum_{j=1}^{L}(j-j_0)^2\,\langle j_0|\left(\sum_{\alpha,\beta=1}^{L} e^{-it(\epsilon_\alpha-\epsilon_\beta)}\,|\alpha\rangle\,\langle\beta|\,\langle\alpha|\,\hat{n}_j\,|\beta\rangle\right)|j_0\rangle \end{aligned} \tag{3.29}$$

In the small J limit, going only to $\mathcal{O}(J^2)$, by Eq. (3.10), since $|n\rangle$ are position

[1] $\hbar = 1$

eigenstates, and $j - j_0 = 0$ for $j = j_0$, only positions corresponding to sites $j = j_0 \pm 1, \pm 2$ will provide non-zero evaluation. Additionally, ϵ_α are taken here as the zeroth order energy, θ_α only, here denoted θ_j for the position basis. Eq. (3.29) therefore simplifies in this regime to

$$\begin{aligned}\Sigma(t)^2_{J\to 0} \approx & \left(\frac{J}{\delta_{j_0+1,j_0}}\right)^2 \left(2 - e^{-it\delta_{j_0+1,j_0}} - e^{it\delta_{j_0+1,j_0}}\right) + 4\left(\frac{J}{\delta_{j_0,j_0+1}}\right)^2 \left(\frac{J}{\delta_{j_0+2,j_0+1}}\right)^2 \\ & + \left(\frac{J}{\delta_{j_0-1,j_0}}\right)^2 \left(2 - e^{-it\delta_{j_0-1,j_0}} - e^{it\delta_{j_0-1,j_0}}\right) + 4\left(\frac{J}{\delta_{j_0,j_0-1}}\right)^2 \left(\frac{J}{\delta_{j_0-2,j_0-1}}\right)^2 \\ = & \, 4\left(\frac{J}{\delta_{j_0+1,j_0}}\right)^2 \sin^2\left(\frac{t\delta_{j_0+1,j_0}}{2}\right) + 4\left(\frac{J}{\delta_{j_0-1,j_0}}\right)^2 \sin^2\left(\frac{t\delta_{j_0-1,j_0}}{2}\right) + \mathrm{f}\left(\frac{J}{\delta_{j\pm1,j}}\right)\end{aligned} \tag{3.30}$$

where $\delta_{j\pm1,j}$ is the difference in adjacent potentials $\theta_j - \theta_{j\pm1}$ around site j_0, and $\mathrm{f}\left(\frac{J}{\delta_{j\pm1,j}}\right)$ is the sum of the two time independent terms. Inputting into Eq. (3.28) the dynamic exponent in the limit $J \to 0$ is given by

$$\begin{aligned} z(t)^{-1}_{J\to 0} \approx & \, t\frac{\delta_{j_0-1,j_0}\sin\left(\frac{t\delta_{j_0+1,j_0}}{2}\right)\cos\left(\frac{t\delta_{j_0+1,j_0}}{2}\right) + \delta_{j_0+1,j_0}\sin\left(\frac{t\delta_{j_0-1,j_0}}{2}\right)\cos\left(\frac{t\delta_{j_0-1,j_0}}{2}\right)}{2\left(\frac{\delta_{j_0-1,j_0}}{\delta_{j_0+1,j_0}}\right)\sin^2\left(\frac{t\delta_{j_0+1,j_0}}{2}\right) + 2\left(\frac{\delta_{j_0+1,j_0}}{\delta_{j_0-1,j_0}}\right)\sin^2\left(\frac{t\delta_{j_0-1,j_0}}{2}\right) + \mathrm{f}\left(\frac{J^2}{\delta_{j\pm1,j}}\right)} \\ = & \, t \times \mathrm{h}(\delta_{j_0\pm1,j_0}) \end{aligned} \tag{3.31}$$

The same as before, since differences in energy levels scale in the CUE as $\delta_{\alpha\pm1,\alpha} \propto 1/L$, when randomized and applied as on site potentials in the Anderson model the difference from one site to the next, $\delta_{j\pm1,j}$, will behave as $\delta_{j\pm1,j} \gtrsim 1/L$. The terms of $\mathrm{f}(J^2/\delta_{j\pm1,j})$ therefore drop out for $J \lesssim 1/\sqrt{L}$. The dynamics in the small J limit (i.e. within the CUE regime of the level statistics) are therefore expected to be independent of both system size and hopping amplitude. Indeed, this could have been expected, as in the $J \to 0$ limit the eigenstates become particles localized on the lattice, only seeing some contribution from nearest neighbor potentials.

Doing similarly in the $J \to \infty$ limit, plugging the momentum states and large J perturbed energy into Eq. (3.29), an equation for the spread of the wavepacket site

occupation is found:

$$\begin{aligned}\Sigma(t)^2_{J\to\infty} &\approx \sum_{j=1}^{L}\left(\frac{(j-j_0)}{L}\right)^2\sum_{k,l=0}^{L-1}\exp\left[-i2tJ\left(\cos\left(\frac{2\pi l}{L}\right)-\cos\left(\frac{2\pi k}{L}\right)\right)+p_k-p_l\right]\\ &\qquad\qquad\times\exp\left[i2\pi(k-l)\frac{(j-j_0)}{L}\right]\\ &= \sum_{j=1}^{L}\left(\frac{(j-j_0)}{L}\right)^2\left(L+\sum_{0\le k<l\le L-1}2\cos[\mathrm{g}(tJ)_{j,k,l}]\right)\end{aligned} \tag{3.32}$$

where p_k is the perturbation on the energy determined in section 3.2.3, $\mathrm{g}(tJ)_{j,k,l}$ is taken in each summed term by

$$\begin{aligned}\mathrm{g}(tJ)_{j,k,l} &= 2tJ\Big[\cos\frac{2\pi l}{L}-\cos\frac{2\pi k}{L}\Big]+p_k-p_l+2\pi(k-l)\frac{(j-j_0)}{L}\\ &= tJG_{k,l}+2\pi(k-l)\frac{(j-j_0)}{L}\end{aligned} \tag{3.33}$$

and noting it has the property $\mathrm{g}(tJ)_{j,k,l}=-\mathrm{g}(tJ)_{j,l,k}$ which has been used in the simplification of the overall sum. Again, translating this into terms for the dynamic exponent, it is seen that it may be approximated by

$$\begin{aligned}z(t)^{-1}_{J\to\infty} &\approx -tJ\frac{\sum_{j=1}^{L}(j-j_0)^2\sum_{0\le k<l\le L-1}\sin[\mathrm{g}(tJ)_{j,k,l}]G_{k,l}}{\sum_{j=1}^{L}(j-j_0)^2\Big(L+\sum_{0\le k<l\le L-1}2\cos[\mathrm{g}(tJ)_{j,k,l}]\Big)}\\ &= tJ\times\mathrm{h}(tJ,1/L)\end{aligned} \tag{3.34}$$

In the large J limit the dynamic exponent is expected to scale in J with $(t\to t/J)$.

As $z(t)^{-1}$ changes smoothly with differences in hopping amplitude applied, an exact magnitude of J where this regime is expected to dominate is difficult to label. A numerical analysis moving from the small, to large J limit over a range of system sizes is therefore provided (Figure 3.2). As well, unlike the small J limit, higher order corrections were not taken for the state function, and the equation above is only used as a way to extract the scaling collapse.

Without going further into the analytics, it would seem that there is some $1/L$ scaling. Moving into the numerics this is largely not the case, as with the UN disorder Anderson model (Figure 3.4.a) [41]. It is therefore expected the calculated factor of $1/L$ will cancel out. One feature that does seem to have some scaling in system size is the sudden drop from the collapsed curve, seen in both Figure 3.4.a and b.

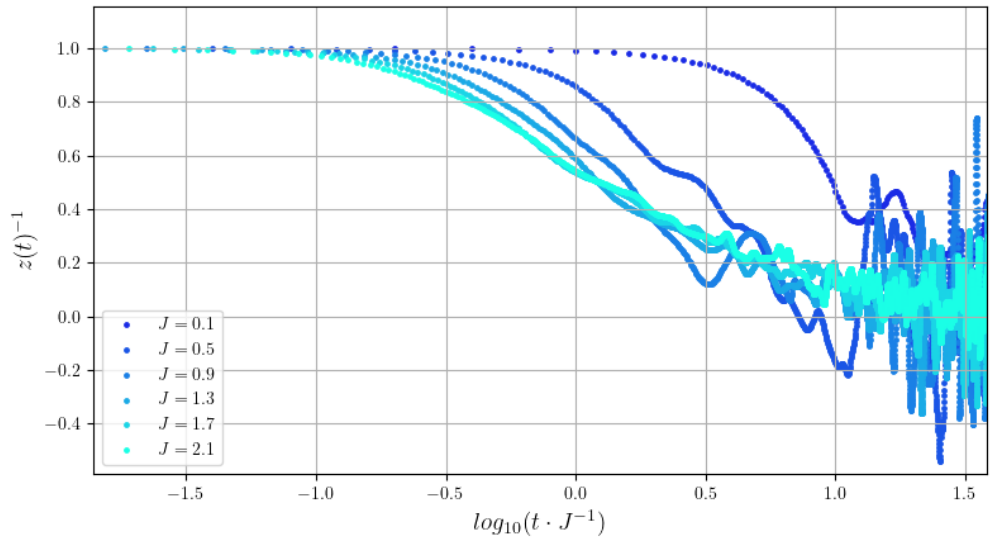

Figure 3.2: Dynamic exponent $z(t)^{-1}$ evolved over time t for the $1/\sqrt{L} < J < 2$ regime at $L = 500$ using 500 samples from the Hamiltonian ensemble. Time has additionally been rescaled by the inverse hopping amplitude.

Although not shown, these features have a scaling collapse which goes like $t \to t\sqrt{L}$. Additionally, they occur earlier in time with increased J or decreased L. The physical interpretation is the wavefunction moving through the sites in the system and running into itself. As such, this feature is expected to disappear in the thermodynamic limit, leaving only the J dependency.

Considering first the relationship in J in the small J limit, as found above, it is observed that there is almost no influence on the dynamic behavior for $J \lesssim 1/\sqrt{L}$. Moreover, this regime may even be extended to larger hopping magnitudes (Figure 3.3). Taking the difference in 100 quasi-energies and applying them to Eq. (3.31), it is also seen that the numerical and "exact" plots match well for early time, and similarly change to a more sporadic behavior at $\mathcal{O}(t) \approx 1$ (Figure 3.3). This makes sense, as the particle starts localized in position, approximately remains localized, and only fluctuates ballistically within the nearest lattice sites.

Over the range $1/\sqrt{L} \lesssim J \lesssim 2$, the dynamics quickly require t/J re-scaling for a collapse (Figure 3.2). How this crossover behaves on the upper limit of J is not known yet, but it seems as though larger systems find it for smaller J. Continuing to increase J further, this scaling collapse persists (Figure 3.4.b). A smooth crossover from $z^{-1}(t) = 1 \to 0$ is thus witnessed, with the scaling and qualitative form of Figure

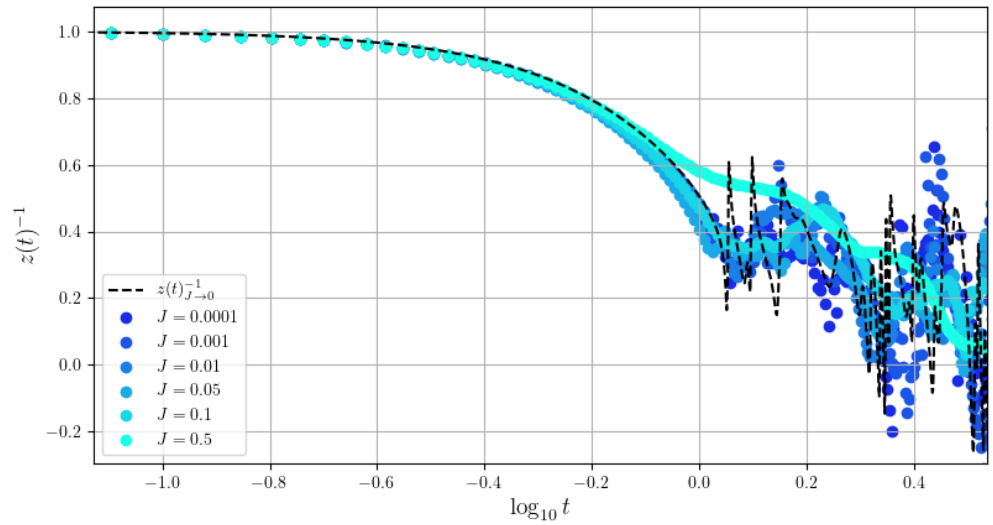

Figure 3.3: Dynamic exponent $z(t)^{-1}$ evolved over time t in the $J \to 0$ limit at $L = 500$ using 100 samples of $\delta_{j_0\pm1,j_0}$ from the Hamiltonian ensemble for the $z(t)^{-1}_{J\to 0}$ prediction, and 500 samples for the purely numerical data.

3.4 likely taking place in the thermodynamic limit for all J.

Finally the scaling of $t \to t/J$ is not identical to the scaling of UN disorder, where $1/J^2$ might be expected [41]. This can be made sense of by again determination of the conditions for localization-to-localization (J_{GOE}) crossover. First, the localization time is considered, in which the dynamics go from ballistic, to localization in position space. That is, the Thouless time t_{TH}, where here $t_{TH}/J = \text{const.}$, or rather $t_{TH} \propto J$. Following again [41], at the crossover point, t_{TH} will match the Heisenberg time t_H, which is proportional to the inverse level spacing $1/\delta_{j\pm1,j}$. By Eq. (3.25), at the crossover point within a finite system

$$-2J\cos\left(\frac{2\pi k}{L}\right) \approx \mathcal{O}\left(\frac{1}{\sqrt{L}}\right) \tag{3.35}$$

with smaller hopping amplitudes breaking from the large J approximation.

The difference in energy levels therefore go like $\delta_{j\pm1,j} \propto 1/\sqrt{L}$ at this point. As such,

$$t_{TH}(J = J_{GOE}) \propto 1/\delta_{j\pm1,j} \propto \sqrt{L} \tag{3.36}$$

and the critical hopping amplitude for the localization-to-localization crossover is again found at $J_{GOE} \propto \sqrt{L}$. Although the initial scaling in J may appear different, the

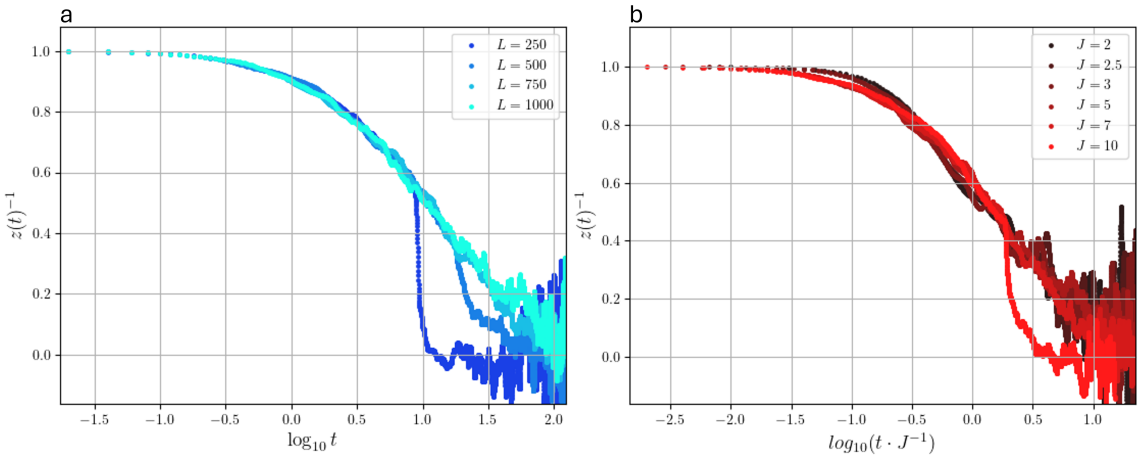

Figure 3.4: Dynamic exponent $z(t)^{-1}$ evolved over time t and averaged over 100 disorder realizations in the large J limit. The left panel (a) depicts $z(t)^{-1}$ for different system sizes L at hopping amplitude $J = 8$. The right panel (b) is taken over different hopping amplitudes at $L = 500$, and has additionally been rescaled by J.

critical localization-to-localization hopping amplitude is recovered, matching that of UN disorder and that previously determined from $\langle\langle \tilde{r} \rangle_\alpha \rangle_H$. Minor scaling differences sourced from the choice of disorder therefore lead to consistent features between models, such as the localization crossover.

3.3.3 Localization in the site occupation basis

Similar to the dynamic exponent, which looked at how a particle prepared on a single lattice site $|j_0\rangle$ spreads out, the inverse participation ratio (IPR), I_α, looks at how the eigenstates $|\alpha\rangle$ delocalize over the physical space. For a single state in a single realization of the Hamiltonian, the IPR is defined here to be

$$I_\alpha = \sum_{j=1}^{L} |\langle j|\,\alpha\rangle|^4 \tag{3.37}$$

For a completely delocalized eigenstate with occupation $1/\sqrt{L}$ on each site, I_α is expected at $L(1/\sqrt{L})^4 = 1/L$. Taking this against a completely localized state where $I_\alpha = 1$, it is found that $1/L \leq I_\alpha \leq 1$.

In order to compare system sizes where logarithmic scaling is required for observation, the inverse participation ratio is rescaled by L. Moreover, it is averaged across 25% of states corresponding to the middle of the single particle spectrum, and further

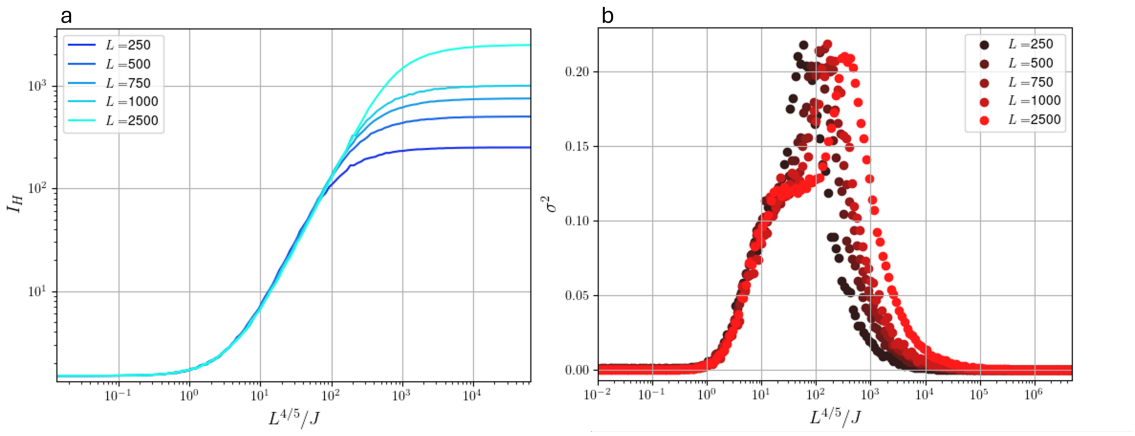

Figure 3.5: Inverse participation ratio of the ensemble, I_H (left), and its variance, σ^2 (right), taken over inverse hopping amplitude $1/J$. In both cases a range of system sizes have been plotted, and the horizontal axis has been rescaled by $L^{4/5}$.

averaged over the ensemble of Hamiltonians. The inverse participation ratio of the ensemble, I_H, is taken here as

$$I_H = L\langle\langle I_\alpha\rangle_\alpha\rangle_H \tag{3.38}$$

such that $1 \leq I_H \leq L$.

In addition to I_H, here the variance of inverse participation ratio, σ^2, is calculated to see the eigenstate crossover from localized to delocalized across the 1D chain. It is given here by

$$\sigma^2 = \left\langle \frac{\langle I_\alpha^2\rangle_\alpha - \langle I_\alpha\rangle_\alpha^2}{\langle I_\alpha\rangle_\alpha^2} \right\rangle_H \tag{3.39}$$

Clearly, in the $I_\alpha \approx L, 1/L$, (localized, delocalized) limits for the single particle eigenstates the variance goes to 0.

Numerical results for I_H and σ^2 are provided in Figure 3.5, 3.6, and 3.7, corresponding to three different scaling collapses. First, the curves of I_H perform as expected. In the small and large J limit, plateaus are observed corresponding to localization and delocalization in position space and are further connected by a smooth curve in the intermediate regime. Similarly, the variance goes to zero in these extremes, peaking in the middle.

Although the overall form of I_H is the same with UN disorder, here the variance and some scalings are seen to change. Although no analytics have yet been done to support this, the best scaling collapse in L for I_H and σ^2 in the large J limit is seen

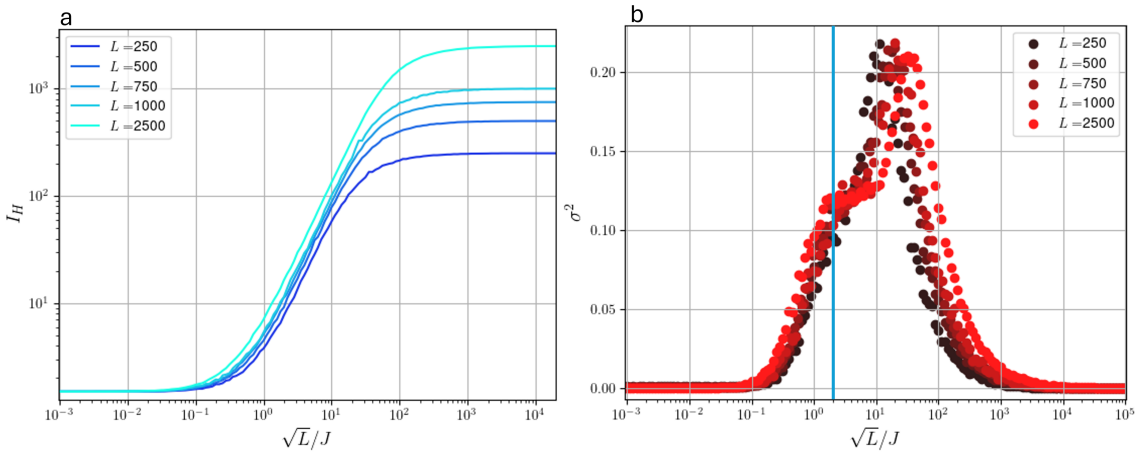

Figure 3.6: Inverse participation ratio of the ensemble, I_H (left), and its variance, σ^2 (right), taken over inverse hopping amplitude $1/J$. In both cases a range of system sizes have been plotted, and the horizontal axis has been rescaled by $L^{1/2}$. The critical hopping amplitude J_{GOE} found in the spectral statistics is additionally given as the vertical blue line.

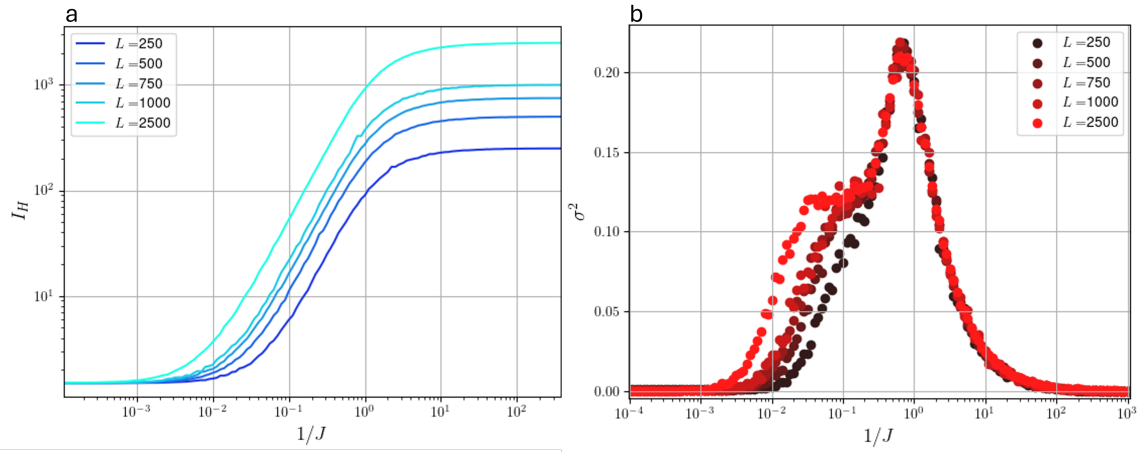

Figure 3.7: Inverse participation ratio of the ensemble, I_H (left), and its variance, σ^2 (right), taken over inverse hopping amplitude $1/J$.

around $1/J \to L^{4/5}/J$ (Figure 3.5). Under UN disorder something like $\sqrt{L}/J$ would be expected [41]. Instead, when rescaling by $1/J \to \sqrt{L}/J$ the curves of the I_H no longer align; however, with reference to Figure 3.6.b, the cusp witnessed within the variance now matches marginally well with the value of J_{GOE} previously determined.

Why the cusp aligns with J_{GOE}, and where this new scaling comes from in the large J limit, has yet to be explored. However, what is immediately clear is that, looking at the unscaled I_H and variance of Figure 3.7 as well as back at the $L^{4/5}/J$

scaling of Figure 3.5, it is again found that eigenstate localization in position space is ensured for any J as $L \to \infty$. While not surprising, this remains a good consistency check with the observations of spectral statistics. Similar to the dynamic exponent, while the scaling is marginally different, the underlying qualities of the Anderson model when using correlated CUE disorder seem to mimic those of UN disorder.

3.3.4 Many-particle eigenstate entanglement entropy

Here, the quadratic nature of the Anderson model will be used to study the entanglement entropy of the many-particle eigenstates in position space. As previously stated, a basis can be found in which the Hamiltonian is diagonalized by some unitary U as $H = \sum_{\alpha=1}^{L} \epsilon_\alpha b_\alpha^\dagger b_\alpha$ where ϵ_α are the single-particle energies and $b_\alpha^\dagger$ (b_α) creates (annihilates) a particle in the eigenstate $|\alpha\rangle$ of the single-particle sector [47, 48]. An n-particle state ($|n\rangle$) in this basis is therefore constructed as a binary sequence of n non-interacting spinless fermions

$$|a\rangle = \prod_{\alpha \in A} b_\alpha^\dagger |\emptyset\rangle \tag{3.40}$$

where $|\emptyset\rangle$ is the vacuum state and A is a random set of $|\alpha\rangle$. It is easy to see that the resulting n-particle energy is $\epsilon_a = \sum_{\alpha \in A} \epsilon_\alpha$.

To analyze the many-particle entanglement entropy, the sector at half filling is chosen ($n = L/2$), and the physical lattice is partitioned into two continuous subsystems of sizes $L/2 = L_A, L_B$ with system L_1 to be studied. The von Neumann entanglement entropy for the first partition is $s = -\mathrm{Tr}(\rho_A \ln \rho_A)$, where $\rho_A = \mathrm{Tr}_2(|a\rangle \langle a|)$ is the reduced density matrix for the partition L_A and the degrees of freedom for L_B have been traced out.

It is useful to note, however, that the many-particle states are made from non-interacting (uncoupled) fermions, and moreover are described by Slater determinants [48]. By Wick's theorem, under these conditions all many-particle correlation functions factorize into the product of one-particle correlation functions [48, 53, 54], i.e.

$$\langle c_i^\dagger c_j^\dagger c_k c_l \rangle = \langle c_i^\dagger c_k \rangle \langle c_j^\dagger c_l \rangle - \langle c_i^\dagger c_l \rangle \langle c_j^\dagger c_k \rangle \tag{3.41}$$

The expectation values of correlations in $|n\rangle$ are therefore completely determined by one-body correlation matrices $C_{ij} = \langle c_i^\dagger c_j \rangle$. Since the reduced density matrix must

reproduce the expectation values within the subsystem, this may also be recast as $C_{ij} = \mathrm{Tr}(\rho_A c_i^\dagger c_j)$ [54].

Assuming the reduced density matrix takes the form

$$\rho_A \propto \exp(-H) = \exp\left(-\sum_\alpha \epsilon_\alpha b_\alpha^\dagger b_\alpha\right) \tag{3.42}$$

and the operators are similarly transformed like

$$b_j = \sum_i U_{ij} c_j \tag{3.43}$$

then the one-body correlation matrix is similarly diagonalized by U. Moreover, normalizing $\mathrm{Tr}(\rho_A) = 1$, the one-body correlation matrix is recast as

$$C_{ij} = \sum_{k,l} U_{ik}^* U_{jl} \frac{1}{\exp(\epsilon_\alpha) + 1} \tag{3.44}$$

and the eigenvalues of the one-body correlation matrix, γ_j, are thus related to those of the reduced density matrix by $\gamma_j = [1 + \exp(\epsilon_j)]^{-1}$ [54]. The entanglement entropy can therefore be pulled from the system by only finding the matrix U, provided numerically here, and computing the one-body correlation matrix for some binary sequence of single particle occupations. In a practical sense, the problem has therefore been simplified greatly.

For consistency with comparing to the UN disordered Anderson model in 1D [41], the calculation is modified slightly by using the generalized one-body correlation matrix

$$\begin{aligned} J_{j,k} &= 2\langle a| c_j^\dagger c_k |a\rangle - \delta_{jk} \\ &= 2\sum_{p,q} U_{jp}^* U_{kq} \langle a| b_p^\dagger b_q |a\rangle - \delta_{jk} \end{aligned} \tag{3.45}$$

where $J_{j,k}$ is an $L_A \times L_A$ matrix. Following the transformations of [5, 48, 53, 54, 55], the entropy is then

$$s = -\sum_j^{L/2} \left(\frac{1+\zeta_j}{2}\right) \ln\left(\frac{1+\zeta_j}{2}\right) + \left(\frac{1-\zeta_j}{2}\right) \ln\left(\frac{1-\zeta_j}{2}\right) \tag{3.46}$$

where ζ_j are the eigenvalues of the matrix J. However, the principle idea remains that only a correlation matrix needs to be calculated through a relatively simple numerical

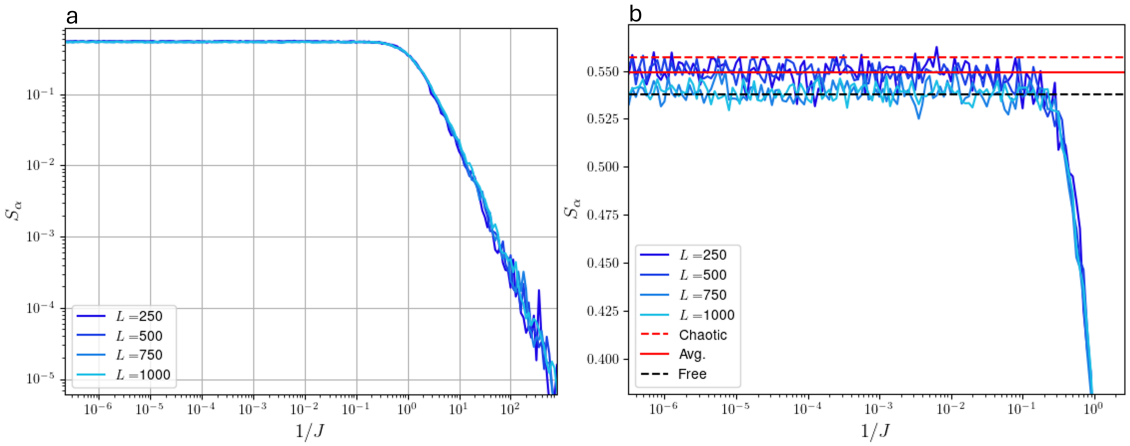

Figure 3.8: Many-particle rescaled entanglement entropy, S_α, averaged over 50 states and 50 disorder realizations plotted over the inverse hopping amplitude, $1/J$, for a range of system sizes L. Large J expectations for the entanglement entropy where the system becomes either chaotic (red dashed line) or resembles a translationally invariant free fermionic system (black dashed line) are provided by the horizontal lines in the right panel (b) [4, 5]. The average ("Avg.") for the smaller L systems has additionally been provided by the solid red line.

step.

Averaging the entropy for each many-particle state $|a\rangle$ within realizations of the Hamiltonian, the quantity $\langle\langle s\rangle_a\rangle_H$ is known to be limited maximally at $L_A \ln 2$ [4]. It is expected that this limit will not be found, but rather that entanglement entropy will go like

$$\langle\langle s\rangle_a\rangle_H = S_\alpha L_A \ln 2 \tag{3.47}$$

where $S_\alpha \in [0, 1]$. In literature, two common values have been recognized for this prefactor corresponding to chaotic systems, $S_\alpha^{cha.} \approx 0.5573$, and free fermionic systems, $S_\alpha^{free} \approx 0.5378$ [5, 4]. It is therefore this value $S_\alpha = \langle\langle s\rangle_a\rangle_H/(L_A \ln 2)$, referred to here as the rescaled entanglement entropy, which is investigated. Thinking about the spectral statistics, for small hopping amplitude it is expected that $S_\alpha \to 0$ as the states become localized entirely on some set of lattice sites. For large hopping amplitude, however, it is expected that $S_\alpha \to S_\alpha^{free}$ as the system is approximated by free moving fermions. This transition is expected to take place around J_{GOE}.

With respect to Figure 3.8, although the qualitative form of the function matches identically to that of UN disorder, the scaling in system size does not [41]. Under UN disorder, scaling in L at $1/\sqrt{L}$ would be expected. The rescaled entanglement entropy under CUE disorder here shows almost no change in behavior with system size. The

crossover from $S_\alpha \to 0$ to S_α^{free} is therefore not seen around J_{GOE}. Additionally, while the large L tests show a S_α^{free} plateau in the large J limit, smaller systems sizes are seen to find a plateau closer to $S_\alpha^{cha.}$ (Figure 3.8.b).

The reason for both of these occurrences is still unknown. While a physical explanation may be possible, it might also be the case that the number of samples from the ensemble of Hamiltonians, or from the number of states, is not enough. Here, 50 states picked randomly from the total spectrum and 50 Hamiltonian realizations were used. Choosing states from one part of the spectrum and using more samples may therefore change these results. As well, the difference in large J plateau for small and large system sizes may be due to finite size effects. Looking at other system sizes between $L = 500$ and $L = 750$ may see a gradual drop to S_α^{free}. More checks need to be completed here prior to making a concrete statement.

3.4 Current and future work

With the behavior of the 1D Anderson model under correlated disorder largely exhibiting the same qualities as with that of UN disorder, beyond possible changes in entanglement entropy, interest is shifted to similar models in higher dimensions. As such, the easy next step is to increase the dimension of the lattice to 2D, where localization is known to not occur as readily. Although still in progress, a few preliminary results observed for Anderson model with CUE disorder on a 2D periodic square lattice are provided below, now taking the Hamiltonian as

$$H = -J \sum_{\langle ij \rangle} c_i^\dagger c_j + \text{h.c.} + \sum_{j_x, j_y = 1}^{L^2} \theta_{j_x, j_y} \hat{n}_{j_x, j_y} \tag{3.48}$$

where L has become the linear size of the lattice along each dimension.

Again, the analysis of the model is started by looking at the spectral statistics (Figure 3.9). While the low J (high $1/J$) CUE plateau and dip to Poisson statistics remain the same, the GOE peak has now become more of a plateau, and the tail end of the large J limit no longer vanishes. While analytic assessment would provide a more convincing claim, it is likely that the non-vanishing tail is due to the higher degree of degeneracy now found in the momentum states.

What is more important here, is the new scaling in system size. As predicted in Section 3.2.3, in 2D the small J limit is found for $J \lesssim 1/L$. As with 1D, the large

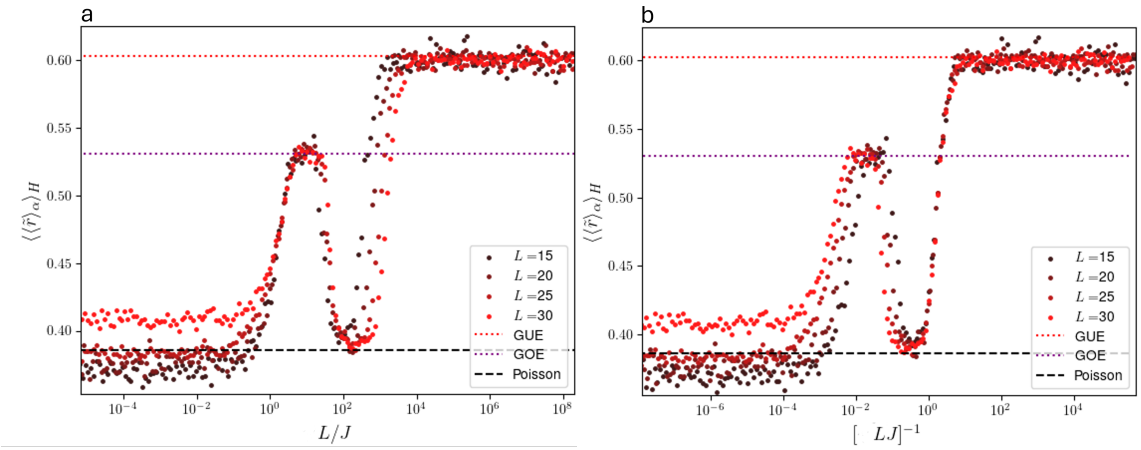

Figure 3.9: $\langle\langle\tilde{r}\rangle_\alpha\rangle_H$ over inverse hopping amplitude, $1/J$, for the 2D periodic CUE disordered Anderson model at a range of system sizes, L. In both cases the system has been rescaled by the linear system size $L^{\pm 1}$. Statistics typical of GUE, GOE, and Poisson systems are provided in each figure by the horizontal dotted/dashed lines.

J limit mirrors this with $J \gtrsim L$ scaling. The break from Poisson level statistics to GOE, however, does not exhibit scaling of $\mathcal{O}(L)$, but instead is conjectured to scale closer to a logarithmic correction in L. That is, while the GOE (chaotic) phase is not totally stable in the true thermodynamic limit, it does grow for large L.

With this, several questions can therefore be asked. It should be repeated that the spectral statistics calculated above were done for the single particle sector of the Hamiltonian. A current research avenue is thus investigating how this chaotic regime behaves through the full many-particle Hamiltonian via the spectral form factor (SFF). Typically defined as

$$\mathcal{K}(t,J)_H = \left\langle |\mathrm{Tr}(\exp[-itH])|^2 \right\rangle_H \tag{3.49}$$

with a characteristic dip-ramp-plateau behavior in many systems exhibiting quantum chaos, the SFF may be used as both an indicator of that chaos, as well as a probe for dynamic properties like the Thoulesss time discussed above [46, 49]. How it behaves in the GOE regime found within the single particle spectral statistics of the 2D Anderson model remains to be seen.

3.5 Conclusions to the 1D Anderson Model

The current analysis suggests that the 1D Anderson model under CUE disorder largely exhibits the same behavior as with uniform disorder. That is, beyond some differences in scaling, correlated disorder seems to have minimal influence over the generic localization of the model. While a few truly novel features may be present, like within the entanglement entropy, considering the close consistency of most other statistics with uniform disorder, it is more likely they are due to a lack of convergence within the ensemble sampling.

Regardless, the groundwork has been laid to explore effects of correlated disorder for fermionic systems in higher dimensions, as well as step into more exotic systems. Several questions, like how the spectral form factor behaves within the new chaotic plateau of the 2D Anderson model, additionally remain to be seen.

Chapter 4

Tensor Operations from Quantum Information for Classical Spin Systems

4.1 Introduction to tensor networks

Solving large systems is an ever-present problem in many areas of physics. Handling many degrees of freedom presents a challenge for representing the problem onto a computer. Finding an algorithm that scales in a way that useful results can be derived is paramount to finding new results.

In 1966, Kadanoff introduced the idea of using a renormalization group algorithm to truncate the degrees of freedom in a lattice from an untenable amount of data to something that could be used to solve a physical system [56]. The modern view of these algorithms is that the density matrix can be used to truncate the large number of degrees of freedom to obtain the most relevant states in a system.

One of the most popular algorithms for solving classical spin lattices (as was the original formulation) is the tensor renormalization group (TRG) from Levin and Nave in 2007 [7]. This algorithm solved for an exponential number of spin sites on a two-dimensional square lattice and can be readily extended to other lattice geometries.

Since that time, an explosion of algorithms has entered into the literature. Many additional tools and techniques have been added to the main idea behind TRG. The use of disentanglers in the tensor network renormalization (TNR) algorithm greatly reduced the bond dimension that was required to obtain high accuracy results [57].

Truncating the environment tensors in the second renormalization group similarly was pursued in several algorithms [58]. Often the major improvements in the algorithms are to improve on the accuracy of calculating a thermodynamic value for a given model, or to solve a different lattice geometry [59, 60].

In this chapter, the goal was made to of code all relevant tensor network renormalization group algorithms for 2D classical spin systems into a single library, DMRjulia [61]. While some algorithms remain to be implemented, the completed algorithms have been sorted into four categories: 1) unique renormalization method, 2) use of disentanglers, 3) modification of decomposition, and 4) environment updates. In many cases, algorithms of later sections build off of those from previous ones. An in depth overview is provided for each algorithm, and the chapter concludes with a short example from a few of the algorithms, noting that a full analysis to find the best one is yet to be completed. In doing this project, it was additionally noted that simple tensor operations might allow one to take any lattice, to any other. As this has not been explicitly noted in literature, a discussion is provided below on how and why this might be done, resulting in the need for only one tensor network renormalization group algorithm, hard coded to a single lattice.

4.2 Formulation of the problem

4.2.1 General problem

The formal description of the problem is best phrased as the computation of the partition function from statistical thermodynamics. Given a Hamiltonian of a physical system the partition function provides a complete description of the system's properties [62]. In the grand-canonical partition function where temperature T ($=1/\beta$) is considered as a variable, then the probability of being in a state with energy E_i is

$$P_i \propto \exp(-\beta E_i) \tag{4.1}$$

where P_i is the probability for the ith state [62, 63]. The partition function is merely the sum of all probabilities

$$\mathcal{Z} = \sum_i P_i \tag{4.2}$$

where the energies E_i can be implicitly a function of the applied magnetic field h, temperature T, or some other variable.

The probability is normalized by the partition function, but the greater significance of $\mathcal{Z}$ is its relation to other quantities of interest in the system. Computation of the partition function at a range of temperatures can be used to obtain quantities such as the specific heat

$$C_V = -\beta \frac{\mathrm{d}^2 \mathcal{Z}}{\mathrm{d}T^2} \tag{4.3}$$

or the magnetization

$$M = \frac{\mathrm{d}^2 \mathcal{Z}}{\mathrm{d}h^2} \tag{4.4}$$

for some applied magnetic field h. As will be shown, the partition function and these thermodynamic quantities will be simple to pull from the tensor networks when simulating both large finite systems, and towards the thermodynamic limit.

4.2.2 Notation via diagrams

For the purposes here, the use of a diagrammatic notation will greatly reduce the amount of information required in conveying the algorithm for implementation. How they are used in this work is summarized below. Here, the rank of a tensor is defined as the number of indices a tensor has, whereas the size refers to the dimension of some index. For example, tensor $T_{\mu\nu}$ is a rank-2 tensor (matrix), and each index μ and ν have some dimension ≥ 1.

The rank of a tensor is denoted on a diagram with a shape and a number of lines (indices, edges) that extend from it. This matches the rank of the tensor being represented. Figure 4.1 demonstrates a rank-4 tensor undergoing a reshape and permutation of the indices to cast it as a rank-3 tensor under the diagram notation.

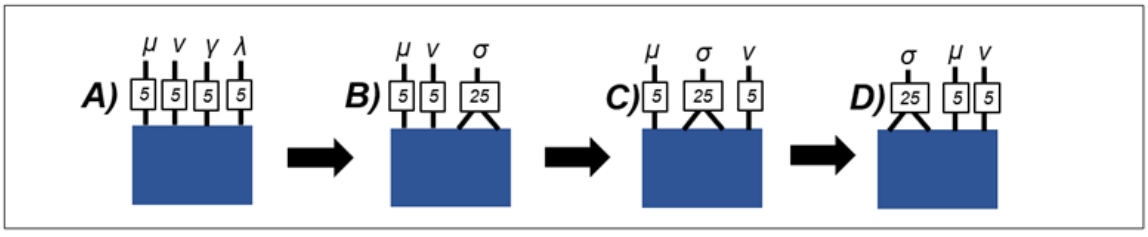

Figure 4.1: The permuting and reshaping of a rank-4 tensor ($T_{\mu\nu\gamma\lambda}$) to a rank-3 tensor ($T_{\sigma\mu\nu}$). In steps A to B a reshaping of the indexes can be seen, going from (5,5,5,5) to (5,5,25). Steps B to C and C to D then permute the indices to form a rank-3 tensor of dimensions (25,5,5).

Moving into the operations which can be competed on these tensors, as introduced

the first two are reshaping and permuting indices. As well, it is always possible to create indices of size 1. With again regards to Figure 4.1, reshaping an index multiplies the size of the indices to make a new one (or produces a multiplicative pair on separation). A size 1 index can therefore be introduced whenever needed. Additionally, for the purpose of this work these operations will be assumed as implicit, and therefore largely ignored.

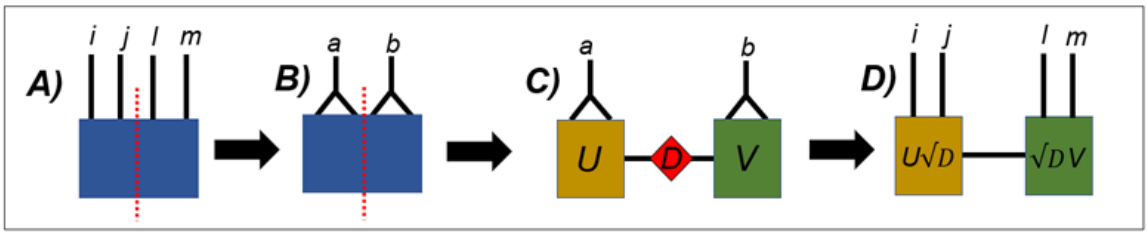

Figure 4.2: Rank-4 tensor decomposition. In step A to B the indices are reshaped to form a matrix, with the desired cut given as the red line. In step B to C, the SVD takes place producing two rank-3 tensors, $\hat{U}$ and $\hat{V}^\dagger$, and one rank-2 tensor connecting the others, $\hat{D}$. The tensor $\sqrt{\hat{D}}$ is then contracted back into each of the flanking tensors.

The next, and final, two operations required for the tensor networks are the contraction and decomposition of two tensors. In diagram notation the contraction of two indices, be it a trace over one tensor or contraction over two, will be given by drawing a line between those indices. Opposite to this, the decomposition of a tensor will commonly be done via the singular value decomposition (SVD)

$$A = UDV^\dagger \tag{4.5}$$

which is denoted by drawing a red line over the tensor. This process is provided in Figure 4.2.

One of the greatest advantages of using this method is seen referring back to what the tensors represent. Since the initial matrix $\hat{M}$ is a redefinition of the wavefunction for the system, ψ, objects such as the density matrix ($\hat{\rho} = \psi\psi^\dagger$) can be retrieved relatively easily. Using the results of the SVD, it would be defined as

$$\hat{\rho} = \hat{U}\hat{D}\hat{V}^\dagger\hat{V}\hat{D}\hat{U}^\dagger = \hat{U}\hat{D}^2\hat{U}^\dagger. \tag{4.6}$$

Any quantities dependent on the system's density matrix, such as the entanglement entropy, can therefore be pulled from the tensor network algorithm formulation.

This tensor decomposition is also the point in which the computational demand of the algorithms increases. As the SVD is completed over matrices, the tensor is first reshaped from some large rank tensor into a rank-2 $m \times n$ object. Upon decomposition, the central $r \times r$ matrix D has the condition $r \geq \min[m, n]$. For any tensor with rank≥ 4 and index size1, like in many lattice system simulations, the size of r will grow at each decomposition operation. In order to ensure the tensors do not grow outside computational limitations a truncation must take place. Since the singular values of D are organized in order from largest to smallest, the procedure used here is to truncate D to the largest q values. Assuming the smaller values of the density matrix are less physically relevant this truncation allows for systems of near thermodynamic magnitude to be closely approximated.

For ease of communication, a variation of the SVD that is used frequently in the algorithms is defined here. One can take the diagonal matrix D and contract $\sqrt{D}$ onto both U and V. This distributes the weights of the partition function onto both tensors and is better than contracting D onto one side. Here it is called a symSVD,

$$A = \left(U\sqrt{D}\right)\left(\sqrt{D}V^{\dagger}\right) \tag{4.7}$$

as will frequently be used.

As a final note on notation, the computational complexity of a given algorithmic step, or over the full algorithm, will be desired. The limiting factor in all of these algorithms is the contraction operation. An uncontracted index will contribute corresponding to the size of the index, χ, while contracted pairs will only contribute χ in total. For a tensor contraction where k free bonds are left at the end and n pairs of indices are contracted will thus computationally scale like $\mathcal{O}(\chi^{n+k})$.

4.2.3 Formulation of the problem with tensors

For a partition function represented by local interactions in some d-dimensional space, the problem of casting the model into the language of tensor networks is commonly completed in two different ways [59, 58]. Taking as an example a two dimensional spin model, the system may be thought of as a graph where spins are located at the vertices while the various site-to-site interactions, or transfer matrices, are defined along each edge. In this way a tensor network is achieved either by considering the decomposition and contraction of the edge matrices, forming a direct tensor network which inhabits the same graph as the model [59], or it is achieved by taking the duality

transformation of the model, forming a dual tensor network on the dual lattice to the original [58].

This process is most simply observed through application of both constructions with the two dimensional Ising model, given as

$$\mathcal{H} = -J \sum_{\langle i,j \rangle} \sigma_i \sigma_j \tag{4.8}$$

where $\sigma_i = \pm 1$ and $\langle i, j \rangle$ is taken only between nearest neighbor spins. The partition function for the system is then defined as

$$\mathcal{Z} = \sum_{\{\sigma_i\}} \prod_{\langle i,j \rangle} \exp\left(\beta J \sigma_i \sigma_j\right) = \mathrm{Tr} \prod_{\langle i,j \rangle} \langle \sigma_i | W_{i.j} | \sigma_j \rangle \tag{4.9}$$

where $W_{i,j}$ is the transfer matrix for the model

$$W_{i.j} = \begin{pmatrix} e^{\beta J} & e^{-\beta J} \\ e^{-\beta J} & e^{\beta J} \end{pmatrix} \tag{4.10}$$

With reference to Figure 4.3.a, on a square lattice the spins and transfer matrices can be pictorially represented with the spins (σ_i) pictured on each vertex, and the $W_{i,j}$ transfer matrices on each edge. From here it is seen that through the decomposition and contraction of the matrices, a network of tensors is constructed directly over the original spin model. The partition function is therefore reformulated in the language of tensor networks as

$$\mathcal{Z} = \mathrm{Tr} \prod_{\langle i,j,k,l \rangle} T_{i,j,k,l} \tag{4.11}$$

In practice the type of matrix decomposition used to form the direct tensor network is not important, so long as the contraction of two adjacent tensors reforms the original transfer matrix along the edge. The decompositions typically chosen, however, are the singular value decomposition, as it applicable to any matrix and may be given as

$$W_{i,l} = U_{i,\alpha} \Lambda_{\alpha,\alpha} V^{\dagger}_{\alpha,l} = A_{i,\alpha} B_{\alpha,l} \tag{4.12}$$

or the eigenvalue decomposition, although not always available for all transfer matrices, and may be given as

$$W_{i,l} = P_{i,\alpha} \Lambda_{\alpha,\alpha} P^{\dagger}_{\alpha,l} = D_{i,\alpha} D^{\dagger}_{\alpha,l} \tag{4.13}$$

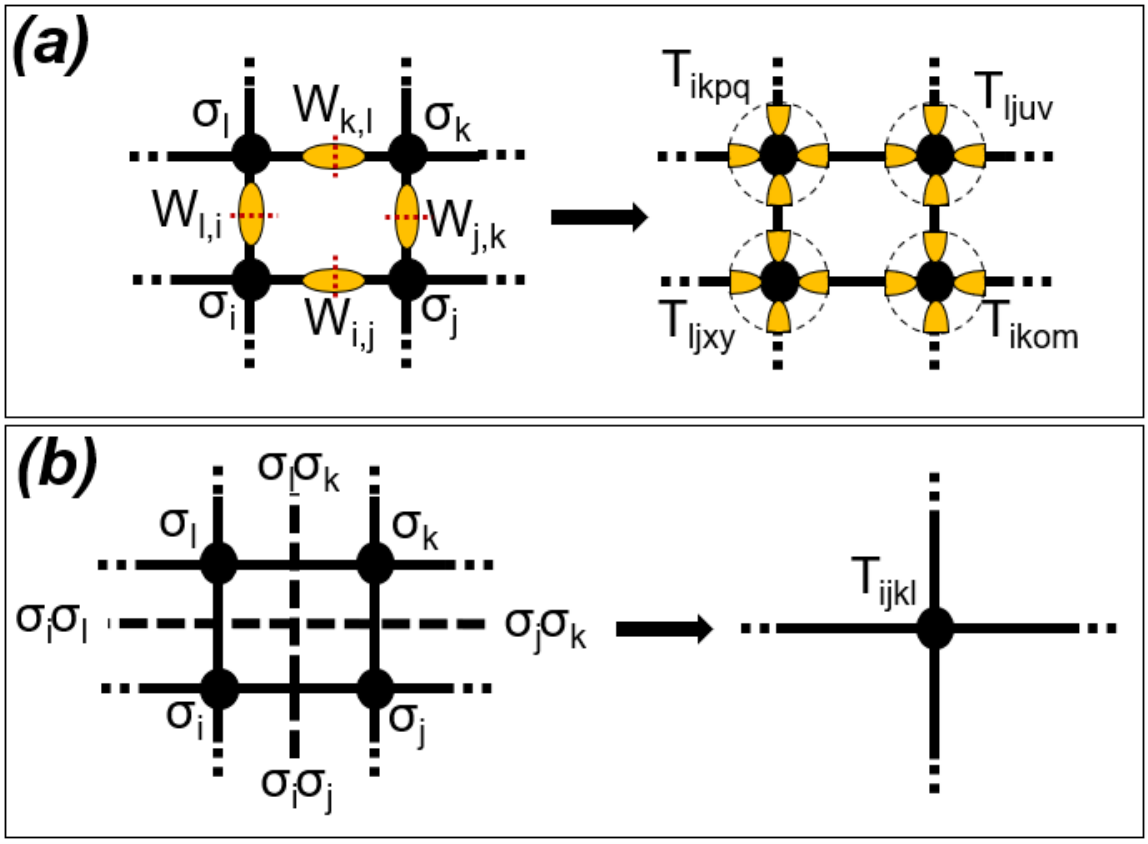

Figure 4.3: Diagrammatic contruction of the tensor network of tensors T_{ijkl} from transfer matrices W_{ij} between spin sites σ_i (a), and using the dual lattice transformation (b).

where in both cases the square root of the central matrix (Λ) has been contracted into the adjacent matrices. For the Ising model on a two dimensional square lattice, the problem is therefore transformed to a network of tensors on the direct lattice

$$T_{i,j,x,y} = D_{\alpha,i} D_{\alpha,j} D_{\alpha,k} D_{\alpha,l} \tag{4.14}$$

Alternatively, returning to the initial Hamiltonian, one can take the duality transformation of the model and further define $S_i = \sigma_i \sigma_j$. With this new variable $S_{i,j}$ similarly taking values of ± 1 depending on the combined parity of the original spins, the partition function may be recast as

$$\mathcal{Z} = \mathrm{Tr} \prod_{\langle i,j,\ldots \rangle} \exp\left(\frac{\beta J}{2} \sum_{i,j} \delta(i,j) S_{i,j} \right) \tag{4.15}$$

where $\delta(i,j)$ is the standard delta function, the factor of 2 has been introduced to avoid double counting, and the sum is taken over each pair of interacting spins. Again, with reference to Figure 4.3.b, specifically for a square lattice system this is given as

$$\mathcal{Z} = \mathrm{Tr} \prod_{\langle i,j,k,l \rangle} \exp(\beta J (S_{i,j} + S_{j,k} + S_{k,l} + S_{l,i})) \tag{4.16}$$

By extension, the tensor network is therefore defined to be

$$T_{i,j,k,l} = \exp\left(\frac{\beta J}{2} (S_{i,j} + S_{j,k} + S_{k,l} + S_{l,i}) \right) \tag{4.17}$$

on the dual lattice system.

While the two methods of construction are equally viable, the resulting tensors are not identical. When input into a tensor network renormalization group algorithm which method was used must be known for normalization purposes.

4.2.4 Mapping between lattices

A short discussion is made here about the generality of the tensor networks constructed. Specifically, so long as the order of tensor operations does not matter, and remains reversible, the graph or lattice may be reshaped into any other, at least locally. This is not to say a dual transformation or similar is taking place. In this context, if an appropriate set of tensor transformations can be found which take, for

example, the graph of a Kagome lattice to that of the square lattice, renormalization may be completed via the square lattice while still representing the original physics, keeping normalization factors in mind.

Two examples are presented to illustrate the idea. First, let there exist a single tensor with a single index, T_i. Via the SVD, this can be decomposed into two tensors $T_i = A_{i,j}B_j$, or reshaped as $T_i = T_{i,j}$ (even if index j is of only size 1). This process of reshaping, decomposing, and adding indices to the network can then be continued as many times as needed. While much of the network may simply contract together to form the identity, by this method any network orientation may be achieved.

While this may seem somewhat trivial, one may again play the same game on a random infinite 2D lattice. First, all the indices within a large region of the network may be contracted into a single tensor. With the caveat that the connections to the external non-contracted region are preserved, this single tensor may then be decomposed, reshaped, have size 1 indices introduced, or contracted as above to form any lattice shape in that region.

It should be noted that the first case would be for the most part entirely redundant, while the second case may be practically impossible due to the size of indices growing incalculable. For the purposes of renormalization on 2D and 3D systems, this really only has benefit in mapping finite 3D systems down to 2D, or when the lattice contains a unit cell where a small set of operations in each cell transform the entire lattice. In the case of reducing the dimension, this can only be done when the system is, say, a few 2D lattices stacked on top of each other.

For the context of 2D renormalization group algorithms, the conclusion of this observation is that the lattice on which the algorithm is carried out does not matter. So long as a set of operations can be made to the unit cell of tensors in the initial system over to the one the algorithm works on, only one algorithm on one lattice is required. As such, while algorithms on other lattices have been coded (Appendix B) the square lattice algorithms will be presented here.

4.3 Classical tensor network algorithms

A summary of the algorithms coded to date is provided below. A brief introduction is given for the prototypical algorithm, TRG, with the others being organized according to their methodology.

Tensor renormalization group (TRG)

By M. Levin and P. Nave [7], TRG has become one of the most common renormalization group approaches throughout statistical physics. The algorithm is broadly composed of sequential singular value decomposition (SVD) and contraction operations on a given tensor network representation in order to coarse grain the lattice.

Considering a tensor network defined on a square lattice, the partition function of the system is initially represented by a field of four index tensors T_{abcd}, as in Figure 4.4(i). Renormalization of the lattice begins by taking a symSVD of each tensor within the network, isolating pairs of adjacent edges (Figure 4.4(ii)). The result is a set of four rank-3 tensors, defined as

$$T_{(ad)(cb)} = A_{ad,e}B_{e,cb} \tag{4.18}$$

and

$$T_{(ad)(cb)} = C_{cd,g}D_{g,ab} \tag{4.19}$$

pictured in Figure 4.4(iii)).

Here, it should be noted that the operation was completed along two different directions to isolate the different pairs of indices. Considering the entire network, the indices which are isolated together alternate between (ab)(cd) and (ad)(cb) from one tensor to the next. In this way, the network of Figure 4.4(iv) is formed, where the rest of the network has been similarly decomposed.

As every tensor T_{abcd} was the same throughout the original network, the result of the network decomposition is a series of plaquettes composed of the four rank-3 tensors, $A_{ad,f}$, $B_{e,cb}$, $C_{cd,g}$, and $D_{h,ab}$, which are contracted as

$$T'_{efgh} = A_{ad,f}B_{e,cb}C_{ab,g}D_{h,cd} \tag{4.20}$$

to reform the renormalized square lattice of tensors T'_{efhg} (Figure 4.4(v)). The number of tensors within the renormalized network has thus been reduced by a factor of two, and the orientation has been rotated by $\pi/4$. Thus, after N iterations a total of 2^N tensors have been renormalized together. Additionally, through the contraction of the four rank-3 tensors a computational cost of $\mathcal{O}(\chi^6)$ is achieved.

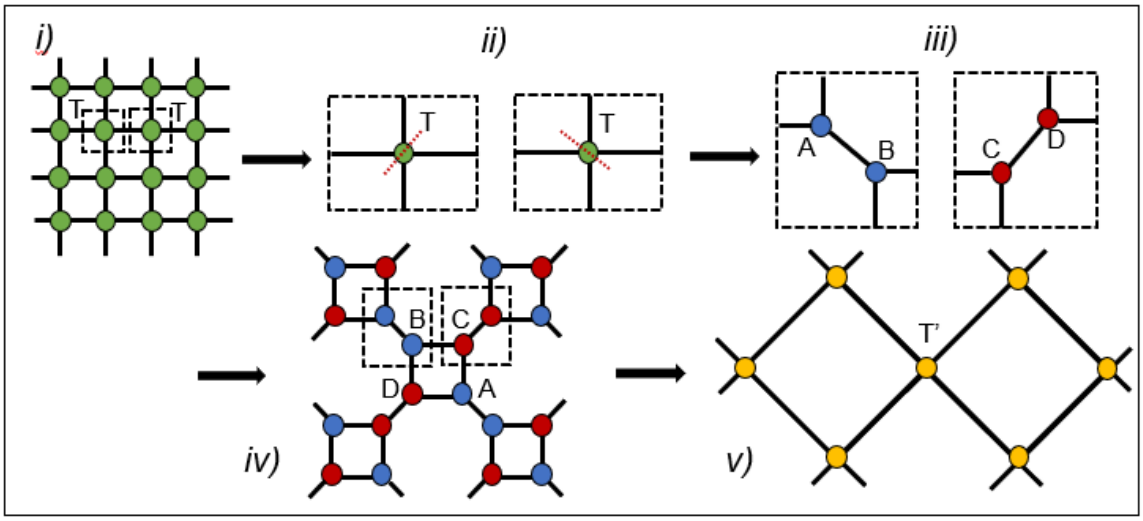

Figure 4.4: The steps used in TRG.

4.3.1 Modifying renormalization

With the fundamental method understood, modifications to the process are now introduced. The first looks to add a tunable parameter to the indices, while the others undertake renormalization via a completely different set of contractions.

Bond-weighted tensor renormalization group (BTRG)

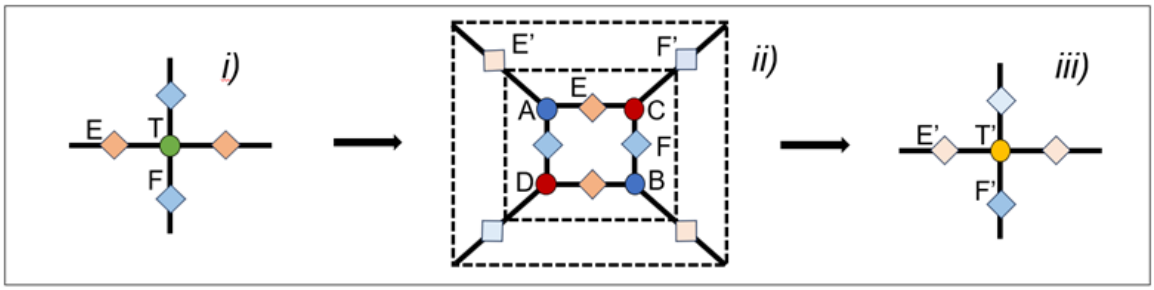

Figure 4.5: The steps used in BTRG.

The BTRG algorithm adds to the TRG algorithm via the introduction of weighted matrices along each lattice index, while keeping the general contraction scheme the same (Figure 4.5(i)) [64]. The BTRG algorithm begins by completing steps i-iii of the TRG algorithm, with the only change that instead of completing a symSVD of

the tensor T_{abcd} as (Figure 4.4(ii))

$$T_{(ad)(cb)} = (U\sqrt{\Lambda})_{ad,e}(\sqrt{\Lambda}V)_{e,cb} \tag{4.21}$$

providing

$$A_{ad,e} = (U\sqrt{\Lambda})_{ad,e} \tag{4.22}$$
$$B_{e,cb} = (\sqrt{\Lambda}V^{\dagger})_{e,cb} \tag{4.23}$$

the BTRG algorithm instead takes

$$A_{ad,e} = (U\Lambda^{(1-\phi)/2})_{ad,e} \tag{4.24}$$
$$B_{e,cb} = (\Lambda^{(1-\phi)/2}V^{\dagger})_{e,cb} \tag{4.25}$$

where ϕ is some predefined constant ($\phi \in [0, 1]$). The same change from symSVD to this new form is made for the decomposition of tensors $C_{ab,f}$ and $D_{f,cd}$ as well.

From this point, a contraction of the four rank-3 tensors is done like with the TRG scheme. Again, the only difference here being that instead of directly contracting the four rank-3 tensors, bond-weighted matrices are introduced between each tensor (Figure 4.5(ii)). They are represented as the tensors E and F along the horizontal and vertical edges of the diagram respectively. For the initialization of the algorithm, the bond weighted matrices are taken as the identity matrix, however upon renormalizing the network they are updated by

$$E'_{ef} = \Lambda^{\phi}_{ef} \tag{4.26}$$
$$F'_{gh} = \Lambda^{\phi}_{gh} \tag{4.27}$$

where Λ_{ef} and Λ_{gh} were the density matrices from the decompositions of the tensors A,B and C,D respectively.

Once the four rank-3 tensors are contracted together with the four bond-weighted matrices a round of BTRG renormalization is complete (Figure 4.5(iii)). In a sense, the algorithm can be thought of as leaving behind Λ^{ϕ} along each bond during each decomposition, which is to be contracted back into the tensor upon the next iteration of the algorithm. Similar to TRG, the network is reduced by two each iteration with a computational cost of $\mathcal{O}(\chi^6)$. For the Ising model, it is additionally known that a value of 0.5 is optimal for the value of ϕ.

Corner transfer matrix renormalization group (CTMRG 1-2)

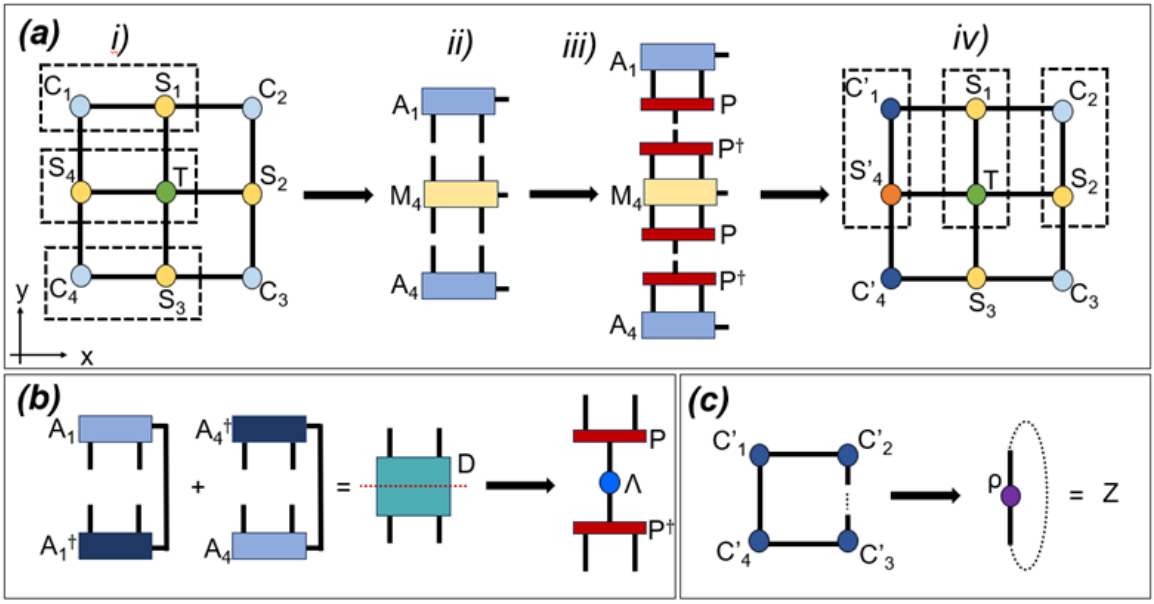

Figure 4.6: The steps used in CTMRG1.

With corner transfer matrices (CTMs) first developed by Baxter in 1968 [65] and later reworked for the context of renormalization by Nishino and Okunishi [66], currently several common CTMRG algorithms are defined. Each algorithm takes a slightly different form with a varying level of uniqueness in contraction order and calculation of specific tensors. The algorithmic steps are therefore provided for two methods which have differences in both these aspects, called here CTMRG-1 and CTMRG-2 [67, 68].

Considering first CTMRG-1, unlike other renormalization group algorithms CTMRG-1 does not consider the entire tensor network, but instead surrounds a single site with CTMs (C^i) and edge tensors (S^i), as seen in Figure 4.6.a(i). While the initialization of these eight tensors is model dependent, one may take C^i_{gm} as 1×1 matrices equal to 1, and S^i_{eaf} as $1 \times n \times 1$ tensors with the dimension 1 edges connecting to two adjacent C^i and the dimension n edge connecting to the central $n \times n \times n \times n$ tensor T_{abcd}.

With reference to the network provided in Figure 4.6.a(i), CTMRG-1 begins by

the set of contractions

$$A^1_{gaf} = C^1_{ge} S^1_{eaf} \tag{4.28}$$

$$M^4_{ghabc} = S^4_{ghd} T_{abcd} \tag{4.29}$$

$$A^4_{hck} = C^4_{hj} S^4_{hck} \tag{4.30}$$

along the left side of the network. As seen in Figure 4.6.a(ii), through the contraction the number of bonds directed along the considered side have increased. To reform the tensors as updated versions of the origonal edge tensors and corner tensors, projectors P and $P^\dagger$ are introduced (Figure 4.6.a(iii)), updating the tensors as

$$C'^1_{fw} = A^1_{gaf} P_{gaw} \tag{4.31}$$

$$S'^4_{mbw} = P^\dagger_{mga} M^4_{ghabc} P_{hcw} \tag{4.32}$$

$$C'^4_{mk} = P^\dagger_{mhc} A^4_{hck} \tag{4.33}$$

For CTMRG-1, the projectors are calculated through the process depicted in Figure 4.6.b. Tensors A^1 and A^4 are contracted with their adjoint, preserving the indices which sit parallel to the side to be projected. The resulting tensors $A^1 A^{1\dagger}$ and $A^4 A^{4\dagger}$ are then added together forming tensor D, from which the SVD provides the projectors P and $P^\dagger$.

This completes CTMRG-1 renormalization for one side of the network. The process is then repeated clockwise around the square, sequentially updating the surrounding eight tensors (Figure 4.6.a(iv)). Once each side has been updated the same number of times, the transfer matrix, and by extension partition function, is taken as the contraction of the four CTMs (Figure 4.6.c). The leading computational cost of the algorithm is $\mathcal{O}(\chi^3)$.

Extending the process to CTMRG-2, while the overall idea is similar, several differences should be pointed out. CTMRG-2 begins with the 3×3 set of tensors T_{abcd} surrounded by 12 edge tensors and four CTMs, as seen in Figure 4.7.a. Additionally, all the edge tensors and CTMs are updated at once for each renormalization step. For the four edge tensors, this update occurs identically to that of CTMRG-1; however, for the CTMs and projectors there are some notable differences.

Taking the top left CTM, C^1_{ge}, as an example, the corner tensor is first contracted

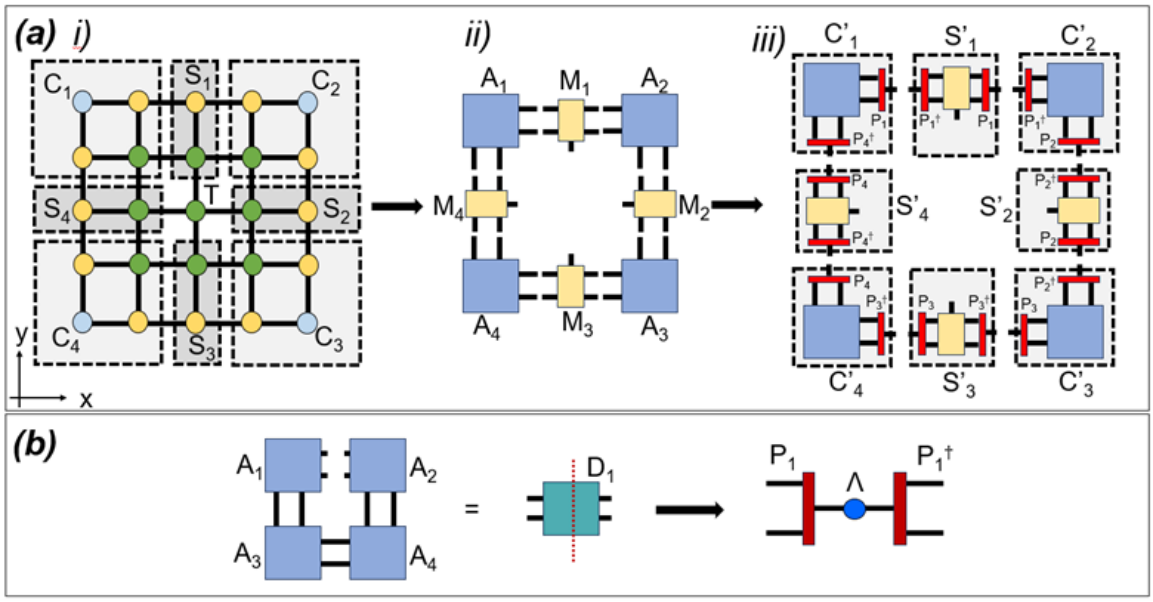

Figure 4.7: The steps used in CTMRG2.

with both connecting edge tensors and a central tensor providing (Figure 4.7.a(i))

$$A^1_{gcfb} = C^1_{ge} S^1_{eaf} S^4_{ghd} T_{abcd} \tag{4.34}$$

Repeating the process on the other four corners, three more rank-4 tensors are produced (Figure 4.7.a(ii)). As with CTMRG-1, the four updated CTMs are reformed by the insertion of projectors along each side. For CTMRG-2 the projectors are calculated by contracting the four rank-4 tensors on each corner together, depicted in Figure 4.7.b, leaving only the indices along the side which the projectors will be applied uncontracted. As with CTMRG-1, an SVD of the resulting D tensor is used to calculate the projectors.

Inserting the projectors for each side into the network, the contraction used to define the updated CTMs and edge tensors is provided in Figure 4.7.b(iii). This completes one iteration of renormalization with CTMRG-2, whereas with CTMRG-1 the partition function is retrieved from the complete contraction of the CTMs. Again, the leading computational cost of this algorithm is $\mathcal{O}(\chi^3)$.

Linearized tensor renormalization group (LTRG, LTRG++)

The LTRG algorithm may be classified similarly to CTMRG type algorithms in the way renormalization is completed [69]. Like CTMRG, LTRG does not renormalize

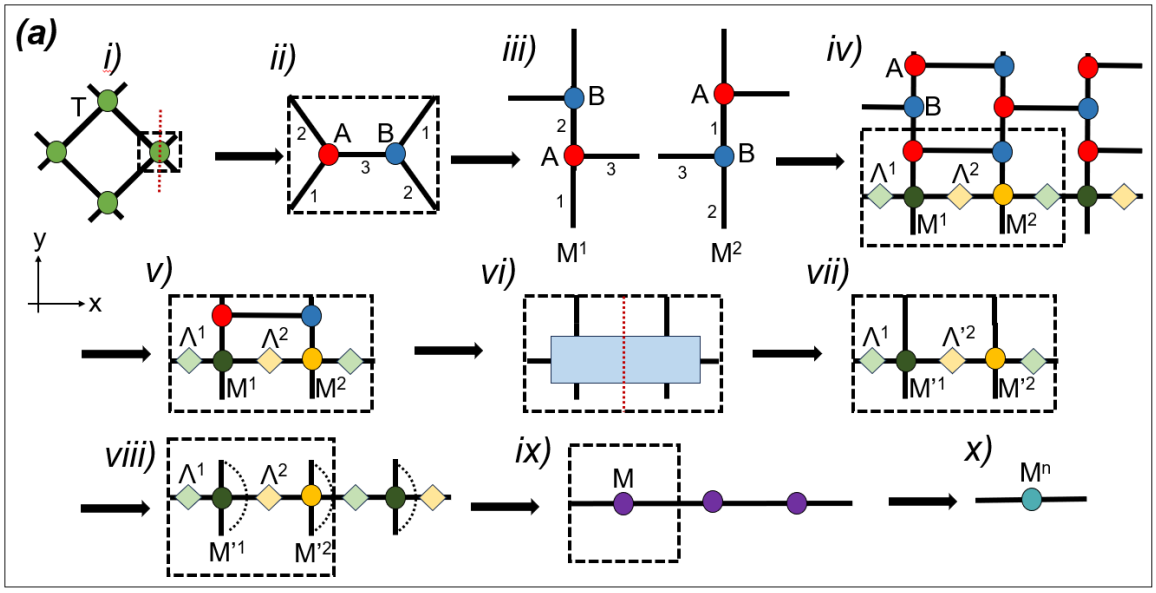

Figure 4.8: The steps used in LTRG.

by completing a typical global coarse graining of the tensor network as with TRG type algorithms. Instead, LTRG picks a one-dimensional chain of tensors within the network upon which sites are linearly added to from one direction.

The algorithm begins by taking a symSVD on every site of the tensor network (Figure 4.8(i)). Unlike TRG, here the symSVD is taken along the same direction for every tensor within the network, providing only tensors A_{ade} and B_{ebc} as in Figure 4.8(ii). Changing slightly the tensor diagrams, it is seen that this network decomposition reforms the systems as an A-B lattice with a brick wall structure (Figure 4.8(iii-iv)).

Picking an arbitrary layer of the tensor wall, a chain of alternating rank-4 tensors is formed through the contraction

$$M^1_{ebdf} = B_{ebc}A_{cdf} \tag{4.35}$$

$$M^2_{fcae} = A_{abe}B_{cbf} \tag{4.36}$$

pictured in Figure 4.8(iii). Similar to the BTRG bond-weighted matrices, matrices Λ^1 and Λ^2 are inserted on the edges connecting each M^1 and M^2 (Figure 4.8(iv)). These matrices are additionally initialized as identity matrices, again like BTRG.

Renormalization in LTRG subsequently occurs in a linear fashion by contracting layers of the A-B network above the formulated tensor chain, as seen in Figure 4.8(v). Once the set of three bond matrices, tensors M^1, M^2, A, and B are contracted

together to form the rank-6 tensor of Figure 4.8(vi) as

$$D_{hbdack} = \Lambda^1_{he} M^1_{ebdf} \Lambda^2_{fg} M^2_{gcaj} \Lambda^1_{jk} \tag{4.37}$$

an SVD is completed to reform the rank-4 tensors M^1 and M^2. Taking the SVD to be

$$D_{hbdack} = U_{hbdf} \Omega_{fg} V^\dagger_{gack} \tag{4.38}$$

the chain of rank-4 tensors are updated as (Figure 4.8(vii))

$$M'^1_{ebdf} = U_{hbdf} / \Lambda^1_{he} \tag{4.39}$$

$$M'^2_{gcae} = V^\dagger_{gcaj} / \Lambda^1 jk \tag{4.40}$$

and the edge matrix which sat between the two rank-4 tensors is updated by

$$\Lambda'^2_{fg} = \Omega_{fg} / \lambda_{max} \tag{4.41}$$

where λ_{max} is the largest singular value of the density matrix Ω_{fg}.

Notably, the contractions and decompositions described only form a half step of the algorithm. Upon renormalization of the next layer of the A-B network onto the chain the contractions have changed slightly. Specifically, the positions of M^1 and M^2 as well as Λ^1 and Λ^2 must be swapped iteratively for each layer.

Unlike many other renormalization group algorithms, the calculation of thermodynamic properties is not immediately retrieved from the trace of a single site within the network. Instead, after N full renormalization steps of LTRG a trace is taken over the chain of tensors M^1 and M^2 in the direction of the A-B lattice to create a one dimensional product of matrices (Figure 4.8(viii)). Completing the contraction

$$M_{hj} = \Lambda^1_{he} M^1_{ef} \Lambda^2_{fg} M^2_{gj} \tag{4.42}$$

the chain is further reduced to a set of identical matrices M_{hj}, where it is assumed 2^N matrices are along the new chain (Figure 4.8(ix)). Pairs of matrices are then contracted together over N products to form a single matrix M^n_{hj} (Figure 4.8(x)). To avoid divergence, during each pairwise contraction the resulting matrices are normalized by their largest value m_{max}. As a result the free energy density, and therefore

thermodynamic properties, are retrieved for a classical system from the equation

$$f = \frac{-1}{\beta}\left[\sum_{i=1}^{2N-2}\frac{\ln(\lambda_m^i ax)}{2} + \sum_{i=1}^{N}\frac{\ln(m_{max}^i)}{2^i}\right] \tag{4.43}$$

Expanding on LTRG, a second algorithm was produced, known as LTRG++, with a nearly identical algorithmic procedure but calculates the free energy density slightly differently [70]. Instead of tracing over the vertical bonds of each rank-4 matrix M^1 and M^2 in Figure 4.8(viii), the adjoint of each tensor is contracted onto the network as in Figure 4.8, leaving only the horizontal bonds uncontracted. As such, half as many renormalization steps are required to reach the same number of sites. Additionally, in LTRG++ instead of contracting the chain of matrices M together (Figure 4.8(ix)) and using their largest values to calculate the free energy density, the largest eigenvalue θ_{max} of the transfer matrix

$$\rho^1_{hgfr} = \Lambda^1_{he} M^1_{ebdf} \Lambda^{1\dagger}_{gk} M^{1\dagger}_{kbdr} \tag{4.44}$$

or

$$\rho^2_{hgfr} = \Lambda^2_{he} M^2_{eacf} \Lambda^{2\dagger}_{gk} M^{2\dagger}_{kacr} \tag{4.45}$$

is determined. The free energy density is thus given by

$$f = \frac{-1}{2N\beta}\left[\sum_{i=1}^{2N-2}\ln(\lambda_m^i ax) + \ln(\theta_{max})\right] \tag{4.46}$$

For both LTRG and LTRG++ the leading computational cost is $\mathcal{O}(\chi^3)$.

4.3.2 Using disentanglers (projective truncation)

One can ask generally how to represent a tensor at a smaller bond dimension. Following the line of thinking that is used for the SVD, the natural way to do this is to preserve the amount of information in the tensor by maximizing the entropy between two tensors, one at a lower bond dimension [71, 72].

In this case, the trace of the density matrix must be maximized during the change of the bond dimension. In order to add an isometry that maps from the larger bond dimension to the smaller bond dimension, the form of the the isometry W must be determined such that $\max\mathrm{Tr}(W\rho)$ is ensured [71].

Because the density matrix can be decomposed according to Eq. (4.5), it happens that

$$\text{maxTr}(W\rho) = \text{maxTr}(WU\Lambda V^\dagger) \tag{4.47}$$

and by the cyclic property of the trace $\text{Tr}(V^\dagger WU\Lambda)$ is an equivalent expression. If any other choice for W does not yield $\text{Tr}(\rho)$, then the value of the trace will not be maximized. Thus, the form of the isometry W must be

$$W = VU^\dagger \tag{4.48}$$

This truncation allows for the reduction of degrees of freedom in the network while preserving the information content. Thus, a larger tensor can be expressed as a smaller tensor but retain a high accuracy in the final evaluation of the problem.

The original use of this technique is most well known in the evaluation of the multi-scale entanglement renormalization ansatz (MERA) [72]. It is used in several algorithms here to be introduced not in historical order but by level of complexity.

Projective truncation-tensor network renormalization (PTTRG 1-3)

The PTTRG algorithm is a straightforward approach to include the use of the projective truncation methods. By Nakamura et al., a total of three algorithms were constructed, defined as PTTRG1, PTTRG2, and PTTRG3 [73].

For PTTRG1, focusing on a single site from a given square lattice tensor network, four isometries are introduced along the diagonal of each tensor (Figure 4.9(a.ii)) which are optimized through the network provided in (Figure 4.9(b.i)). Similar to the TRG algorithm, only half the tensor network is depicted in the diagram as on every other site the bonds which are isolated together are alternated. A symSVD is then completed on the rank-2 tensor formed by $w_1 T w_2$, which are further contracted into the flanking $w_1^\dagger$ or $w_2^\dagger$ tensors to create two rank-3 A and B tensors (Figure 4.9(a.iii-a.iv)). Those created along the alternate axis are defined as C and D.

Pairs of A, B, C, and D are contracted together as BD and AC (BC, AD), followed by the insertion of two pairs of isometries within the system Figure 4.9(a.v). Again, these isometries are optimized through the projective truncation environment provided in Figure 4.9.b.ii. As well, the diagram only provides the operations along the horizontal direction for the isometries, but the same is done along the vertical direction. The central isometries are further contracted together, decomposed through

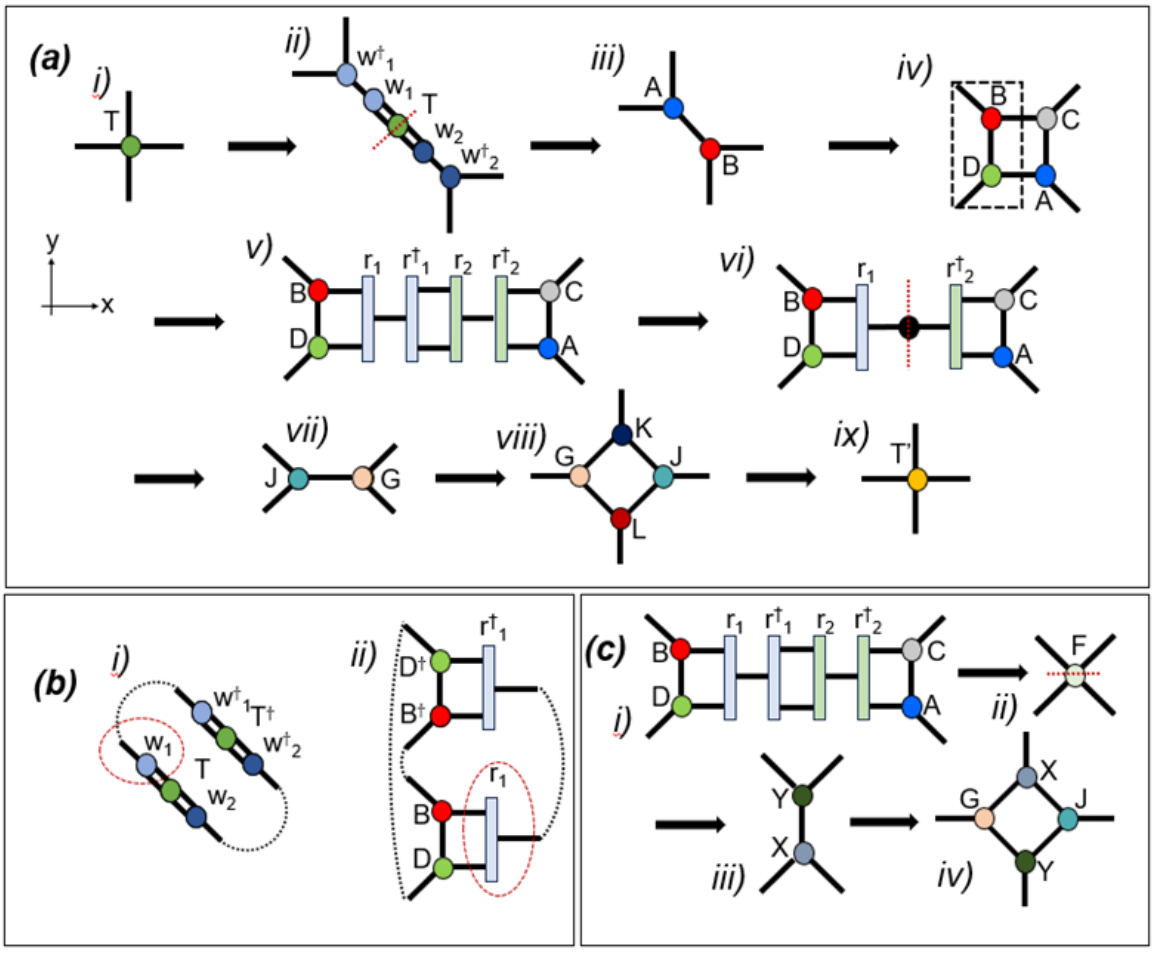

Figure 4.9: The steps used in PTTRG. Dashed circles indicate tensors which are optimized by the surrounding network environment through projective truncation.

a symSVD, and contracted into the flanking tensors (Figure 4.9(a.vi)) to form tensors G and J (K and L) (Figure 4.9(a.vii)). From this point the final tensors are contracted together as in TRG to recreate the initial lattice orientation. Within this coarse graining process the total number of sites has been reduced by a factor of two, at a computational cost of $\mathcal{O}(\chi^6)$.

The PTTRG2 and PTTRG3 algorithms reduce the computational cost by shortening the number of steps required for each iteration of the algorithm. In the case of PTTRG2, this is completed by looping the algorithm from the four rank-3 tensors of Figure 4.9(a.viii) back to Figure 4.9(a.iv) after the first iteration. PTTRG3 then further reduces the cost by directly contracting the network of Figure 4.9(a.v) together as in Figure 4.9(c). This alleviates the need to insert isometries along the

vertical direction within the network since the rank-4 tensor may be decomposed as seen in Figure 4.9(c.ii) to form an approximate version of the tensors K and L of Figure 4.9(a.viiii) as tensors X and Y of Figure 4.9(c.iii).

Tensor network renormalization (TNR)

Unlike many other algorithms the TNR algorithm begins with a 2×2 plaquette of sites on the square lattice where a gauge transformation has been performed on the bottom two tensors [57]. The gauge transformation chosen is equivalent to taking the complex conjugate of the tensors and flipping the top and bottom indices. It is therefore useful to note that the top and bottom half of the depicted network in Figure 4.10(a) are mirror images of each other when looking at the indices, symbolized by the dashed line which bisects the network.

From the initial plaquette (Figure 4.10(a.i)), two sets of isometries (w, $w^\dagger$ and $v^\dagger$, v) and a pair of disentanglers ($u^\dagger$, u) are inserted into the network, each optimized by the environment of Figure 4.10(b) [71]. Tensors A and B are then constructed as depicted in Figure 4.10(a.ii). With respect to the wider lattice, a network of alternating A and B tensors has been constructed, with which a TRG iteration may be completed to reform the coarse grained network of tensors T' (Figure 4.10(a.iii-a.iv)). The direction which the projectors are implemented on the network is then exchanged for the horizontal axis on the next step.

Within an iteration the number of sites has therefore been reduced by four, at a computational cost of $\mathcal{O}(\chi^7)$. Importantly, however, a significant portion of the computational time required for the algorithm is allocated to the optimization of the disentanglers and isometries, which need on the order of tens to hundreds of projective truncation iterations to appropriately converge.

Binary, ternary and TNR-2 tensor network renormalization (biTNR, terTNR, TNR-2)

The biTNR algorithm is an extension of the original TNR algorithm which modifies the algorithm after the insertion of the isometries and disentanglers [71]. Constructing tensor A from Figure 4.10(a.ii), additional projectors y_1 and y_2 are inserted flanking the tensor in the horizontal direction (Figure 4.11(a.ii)) forming a rank-2 tensor C (Figure 4.11(a.iii)). The tensor is subsequently decomposed through a symSVD and contracted into the hermitian conjugate of the inserted projectors forming two rank-

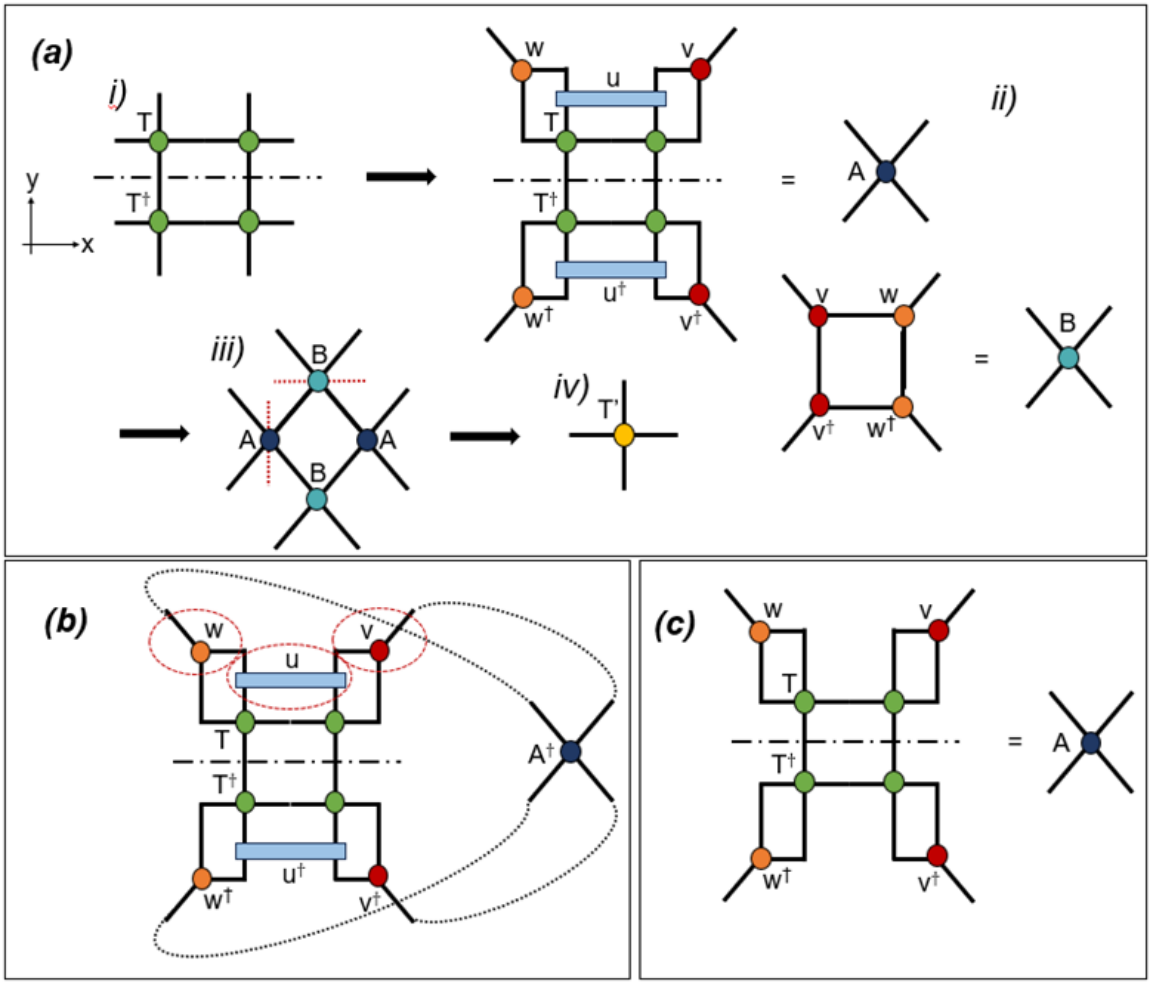

Figure 4.10: The steps used in TNR. Dashed circles indicate tensors which are optimized by the surrounding network environment through projective truncation.

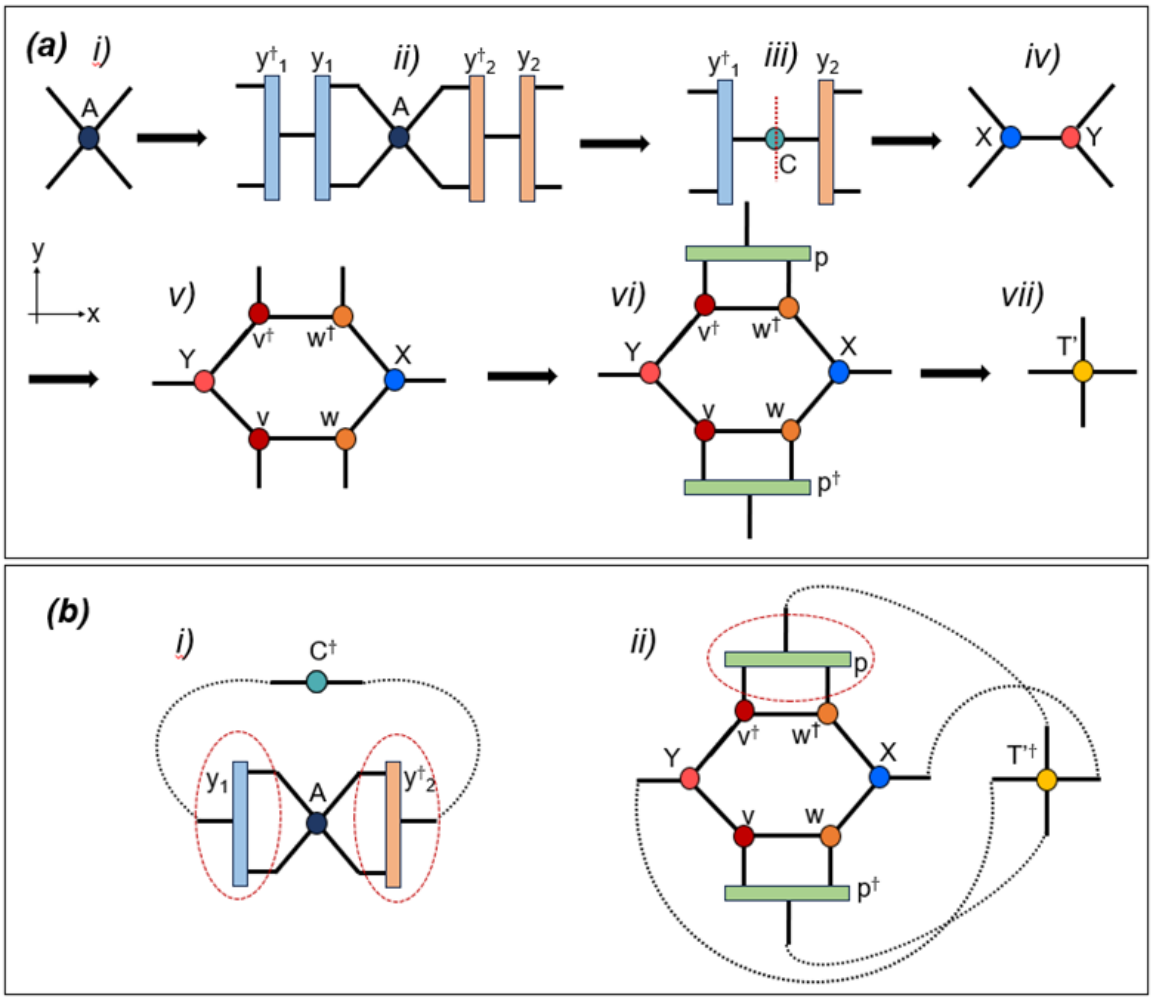

Figure 4.11: The steps used in biTNR. Dashed circles indicate tensors which are optimized by the surrounding network environment through projective truncation.

3 tensors X and Y (Figure 4.11(a.iii)). Unlike the previous TNR algorithm where tensor B of Figure 4.10(a.ii) was constructed through the two isometries w and v along with their hermitian conjugates, the isometries are contracted back into the tensors X and Y, which are further contracted together to make a rank-6 network (Figure 4.11(a.v)). The projector p and its hermitian conjugate are then inserted on the vertical indices to reform the coarse grained tensor network. The direction the projectors are inserted are, like in TNR, flipped to the horizontal axis for the next step. The environments which optimize the novel isometries y_1, y_2, and p through projective truncation are provided in Figure 4.11(b.i-b.ii), with a total proposed cost comparable to that of regular TNR at $\mathcal{O}(\chi^7)$.

Two close variants of the biTNR algorithm have also been completed, called here

TNR-2 and ternary-TNR (terTNR). Within TNR-2 the disentanglers $u^\dagger$ and u of Figure 4.10(a.ii) are initially positioned on top of the isometries w, $w^\dagger$ and $v^\dagger$, v [74]. In this form, however, if the projective truncation environment suggested by [74], pictured in Figure 4.10(b), was used, then the disentanglers would annihilate to the identity immediately. Regardless, the algorithm where the tensor A is exchanged for that of Figure 4.10(c) have been implemented at a proposed computational cost of $\mathcal{O}(\chi^6)$.

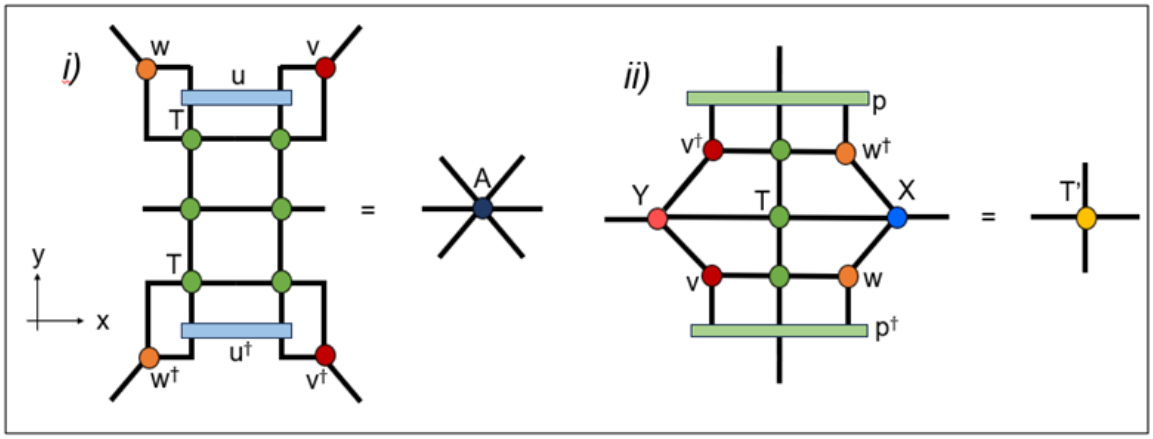

Figure 4.12: The tensors used in terTNR.

For terTNR the operations follow exactly that of the biTNR algorithm, but instead starting with a 3×2 plaquette of network sites T [71]. As such the tensor A gains two indices as a rank-6 tensor (Figure 4.12(i)), with the projectors y_1 and y_2 also gaining a third connecting index each when calculated. The only other change is that a row of tensors T are inserted between the tensors X, Y, and the relevant isometries ((Figure 4.12(ii)) when reforming a reduced network. A third connecting index is therefore also required for the projector p and $p^\dagger$. The number of sites is therefore reduced by a factor of nine each iteration of terTNR. No order of computational cost was provided with terTNR in the original paper, however following the steps of the biTNR algorithm, it is predicted to have a cost of order $\mathcal{O}(\chi^{10})$.

4.3.3 Modifying the singular value decomposition, HOSVD

While the methods of decomposition are not the focus of this work, many algorithms are known to utilize the HOSVD procedure [59, ?]. As such, the benefits will not be commented on, but a mechanical idea of the process within tensor networks is as

follows. Instead of decomposing a tensor $T_i, j, k = U_{i,m} D_{m,n} V^{\dagger}_{n,j,k}$ under the SVD, the HOSVD decomposes the tensor for each index about a core orthogonal tensor [75]. That is,

$$T_{i,j,k} = A_{i,I} O_{I,J,K} B_{j,J} C_{k,K} \tag{4.49}$$

where A, B, and C are unitary.

For much of the processes below, it is only noted when the HOSVD is taking place, as many of the decomposed tensors are immediately contracted back together to create a projector.

Higher order tensor renormalization group (HOTRG)

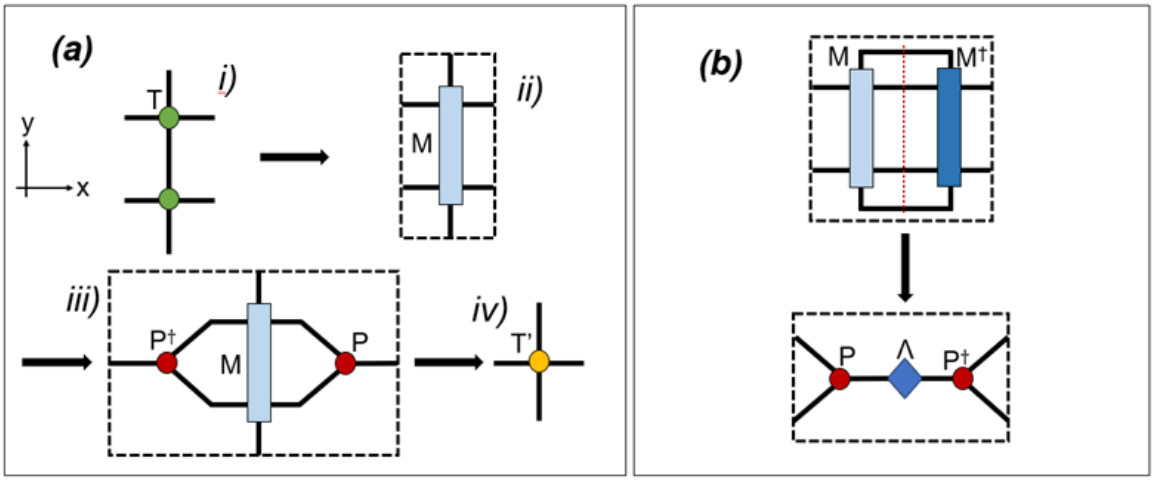

Figure 4.13: The steps used in HOTRG.

The HOTRG algorithm is defined by its use of the higher-order singular value decomposition (HOSVD) operation to combine adjacent tensor indices together [59]. Starting with two lattice sites stacked along the vertical direction, the sites are contracted to form a rank-6 tensor M (Figure 4.13(a.i-a.ii)). The tensor M is then contracted with its hermitian conjugate to form the object from which the HOSVD may take place, retrieving projectors which group the horizontal indices P and $P^{\dagger}$ (Figure 4.13(b)). The tensor M is finally contracted with the determined projectors to form the reduced tensor network. At this point the dimension of the indices along the vertical direction have remained the same as in the initial network, and as such the following iteration of the algorithm is completed along those indices. Each iteration the number of sites has been reduced by half along either the vertical or horizontal

directions at a computational cost of $\mathcal{O}(\chi^7)$.

Bond-weighted higher order tensor renormalization group (BHOTRG)

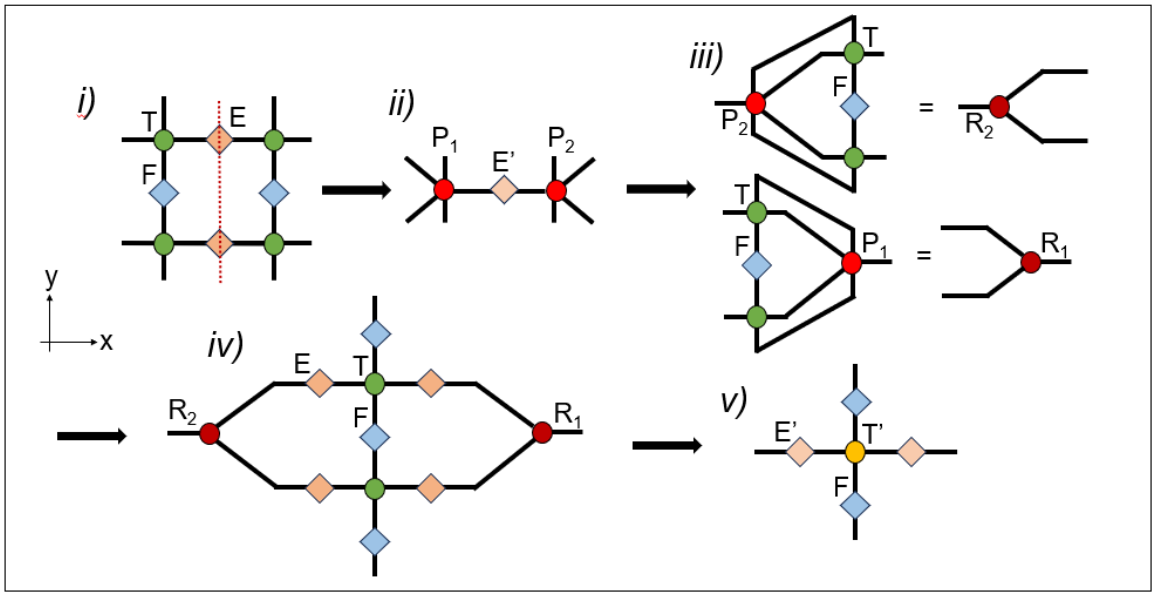

Figure 4.14: The steps used in BHOTRG.

Combining the bond-weighted tensors of the aforementioned BTRG algorithm with the algorithmic steps of HOTRG, the BHOTRG algorithm begins with a plaquette of four tensors T_{abcd} and associated bond-weighted tensors E_{db} and F_{ac} as seen in Figure 4.14(i) [64]. To form the HOTRG-like projectors and coarse grain the network along the vertical direction, the plaquette is contracted together along the internal bonds to form a rank-8 tensor (Figure 4.14(ii)). Here, a similar decomposition is completed to that of BTRG, where instead of a symSVD the tensor $D_{abcdefgh}$ is decomposed by an SVD as

$$D_{abcdefgh} = U_{abcdj}\Lambda_{jk}V^{\dagger}_{kefgh} \tag{4.50}$$

to give (Figure 4.14(iii))

$$P^{1}_{abcdk} = (U\Lambda^{\frac{-(1+\phi)}{2}})_{abcdk} \tag{4.51}$$

$$P^{2}_{jefgh} = (\Lambda^{\frac{-(1+\phi)}{2}}V^{\dagger})_{jefgh} \tag{4.52}$$

where ϕ is some constant $\phi \in [0, 1]$ (Figure 4.14(iii)). Again as with BTRG, the

bond-weighted tensor is updated for the next renormalization iteration to be

$$E'_{jk} = \Lambda^{\phi}_{jk} \tag{4.53}$$

Using the determined rank-5 tensors P^1_{abcdk} and P^2_{jefgh} the final projectors R^1_{cdm} and $R^2_{ghn}$are formed through the contractions of Figure 4.14(iii).

Finally, as with HOTRG, the projectors are applied to reduce the network along the vertical direction by a factor of two. Now for BHOTRG, however, bond-weighted matrices $E^{1/2}_{bd}$ are included along the horizontal edges alongside a matrix F_{ac} between the two tensors T_{abcd} (Figure 4.14(iv)). With this contraction of the projectors with the bond matrices and network tensors one step for the BHOTRG algorithm is concluded, having formed a new network of tensors T'_{abcd} with updated bond-weighted tensors E'_{bd}. The same process is subsequently completed along the horizontal axis, updating bond-weighted matrices F_{ac} instead. The overall computational cost of BHOTRG is $\mathcal{O}(\chi^{10})$.

Anistropic tensor renormalization group (ATRG)

The ATRG algorithm is an extension of the HOTRG algorithm which attempts to reduce the overall cost by decomposing the tensors into smaller ranks during coarse graining procedure [76]. Similar to HOTRG, the number of sites within the network is reduced by two along either the horizontal or vertical direction each iteration. The cost, however, is reduced to $\mathcal{O}(\chi^6)$ for the square lattice, comparable to that of regular TRG.

The algorithm begins by taking a symSVD along the same direction on every network site, forming rank-3 tensors A, B, C, and D (Figure 4.15(a.i-a.ii)). The middle tensors B and C are then contracted along their connecting index as in Figure 4.15(a.iii) to create tensor M, which is further decomposed via a symSVD. The result is a network of tensors A, Y, X, and D, where pairs of left or right facing indices have been moved together (Figure 4.15(a.iv)). A depiction of how the network as a whole is connected along the horizontal axis at this point is provided in Figure 4.15(c). A set of projectors, E and F, are finally inserted on each pair of indices, contracting tensors A and Y or X and D together to retrieve tensors G and H (Figure 4.15(a.v-a.vi)), which are further contracted along their connecting vertical index to reform the coarse grained network (Figure 4.15(a.vii)).

The projectors of the ATRG algorithm are produced through a process slightly

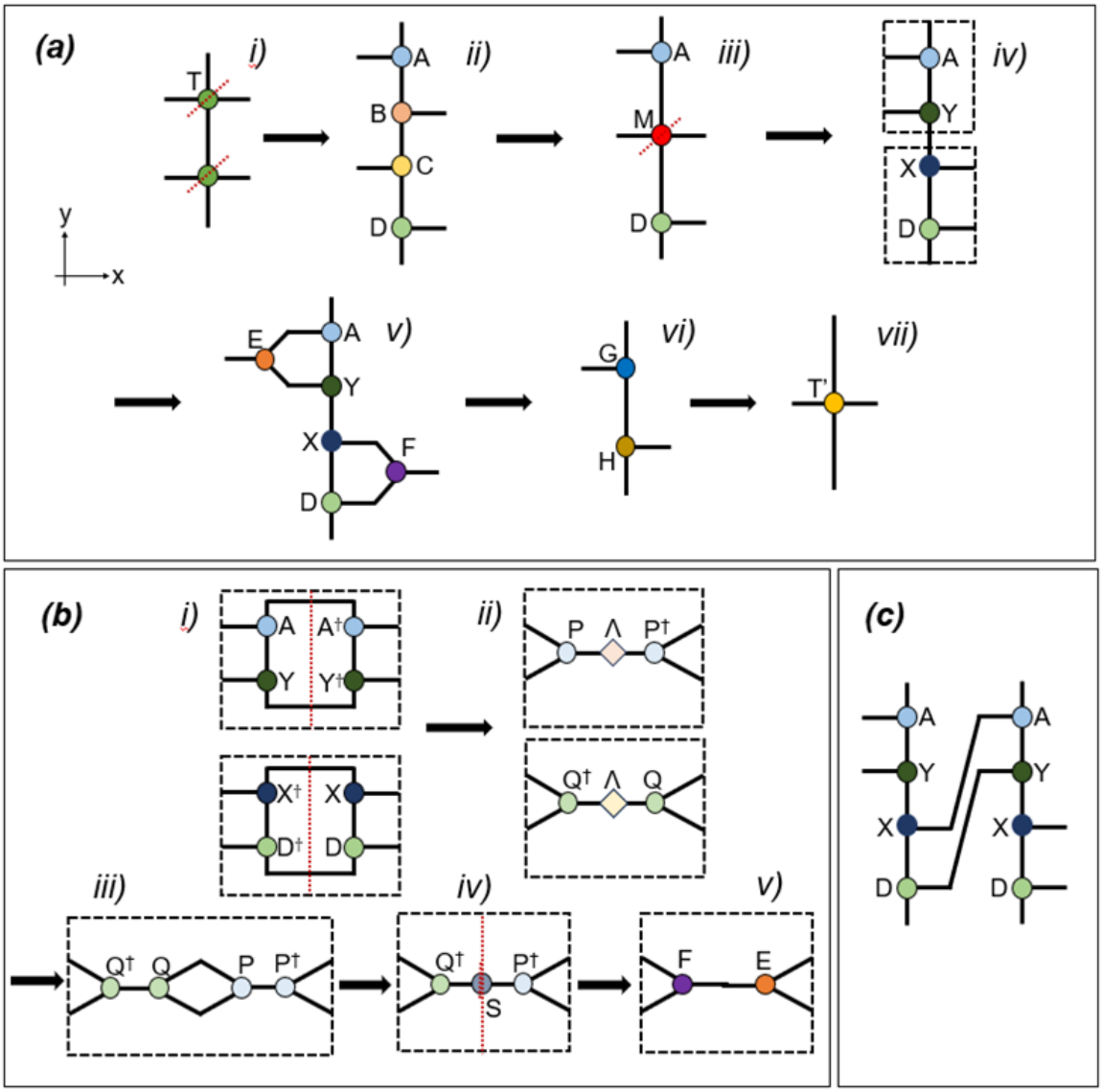

Figure 4.15: The steps used in ATRG.

different to the HOSVD within HOTRG. The pair of rank-3 tensors A and Y (X and D) enclosed by the dashed line box of Figure 4.15(a.iv) are contracted with their hermitian conjugate as in Figure 4.15(b.i). The tensors are subsequently decomposed through an SVD to tensors P, Λ and $P^\dagger$ (Q, Λ and $Q^\dagger$), from which the diagonal tensor Λ is removed, similar to the HOSVD operation (Figure 4.15(b.ii)). The set of tensors P and Q are then contracted together, decomposed through a symSVD, and contracted back into $P^\dagger$ and $Q\dagger$ tensors to form the projectors E and F (Figure 4.15(b.iii-b.v)).

Triad tensor renormalization group (TTRG)

The TTRG algorithm may be thought of as a mix of the ATRG, LTRG and HOTRG algorithms, with the advantage of reducing the overall computational cost to $\mathcal{O}(\chi^5)$ by coarse graining on the triad network [77]. While the algorithm was first formulated to reduce the computational cost of cubic lattice tensor network renormalization, making the triad network potentially more unique in its construction, for the two dimensional square lattice it is seen that it is just an alternate way to draw a hexagonal lattice network or the brick wall network of the LTRG algorithm.

The TTRG algorithm therefore begins in the same way as ATRG and LTRG, taking a symSVD of every tensor throughout the initial network, thus mapping to the triad network of Figure 4.16.a(ii). As with HOTRG, projectors P and $P^\dagger$ are inserted into the network, reducing the number of edges in the vertical direction (Figure 4.16.a(iii)). Instead of directly contracting the entire set of tensors down to a single site, however, the projectors are contracted with a single adjacent rank-3 A or B tensor, as seen in Figure 4.16.a(iv).

Contracting the remaining A and B tensors together within the system, the result is a set of three tensors C, M, and D. While there are various methods to reduce the computational cost further when reforming these three tensors back to the triad network, here a $\mathcal{O}(\chi^5)$ cost is maintained by taking a symSVD of the central tensor M and contracting the two halves onto the adjacent tensors C and D (Figure 4.16.a(v)). One iteration of TTRG is therefore complete where the number of sites has been reduced in half, and with the triad network reformed (Figure 4.16.a(vi)). The process is then repeated but with the projectors inserted along the vertical, thus rotating the diagrams by $\pi/2$. The partition function may finally be pulled from the system through the complete contraction of tensors A and B, matching the vertical (horizontal) bond

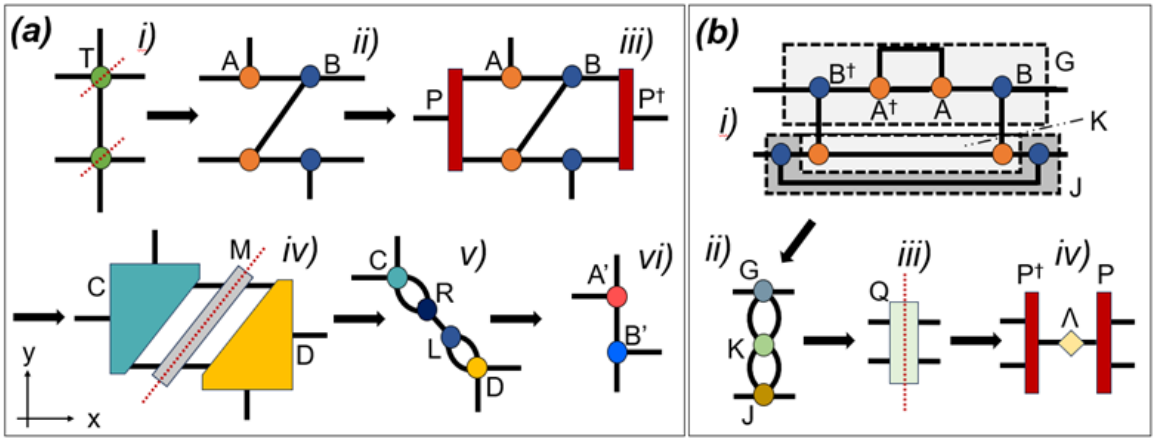

Figure 4.16: The steps used in TTRG.

of each tensor together.

In order to calculate the projectors used in TTRG, again a similar process to HOTRG is applied. The adjoint of the network of four rank-3 tensors in Figure 4.16.a(ii) is taken, and contracted back onto the initial network. This process may be seen in Figure 4.16.b(i), where only the horizontal bonds of the B tensors within the network remain uncontracted. In order to keep the computational cost low, the contraction is taken to initially form three rank-4 tensors G, J, and K. The parts of the network used to form each tensor are represented by the three boxed out regions of Figure 4.16.b(i), with the result in Figure 4.16.b(ii). The tensor K is then decomposed by symSVD and contracted into the adjacent tensors G and J, as was done in the main TTRG algorithm, which are further contracted to form tensor Q (Figure 4.16.b(iii)). The projectors P and $P^\dagger$ are finally formed by the SVD of tensor Q (Figure 4.16.b(iv)).

Core tensor renormalization group (CTRG)

The CTRG algorithm may be thought of as counter to the CTMRG algorithms [78]. Where the CTMRG algorithms take a single site within a network and repeatedly contracts it outward into corner matrices, the CTRG algorithm does the opposite by continually contracting surrounding tensors into a central site.

With respect to the square lattice of Figure 4.17.a(i), CTRG begins by choosing a single site within the network (T^C_{abcd}) to act as the central tensor upon which the surrounding network will be contracted onto. A symSVD is then taken on each site

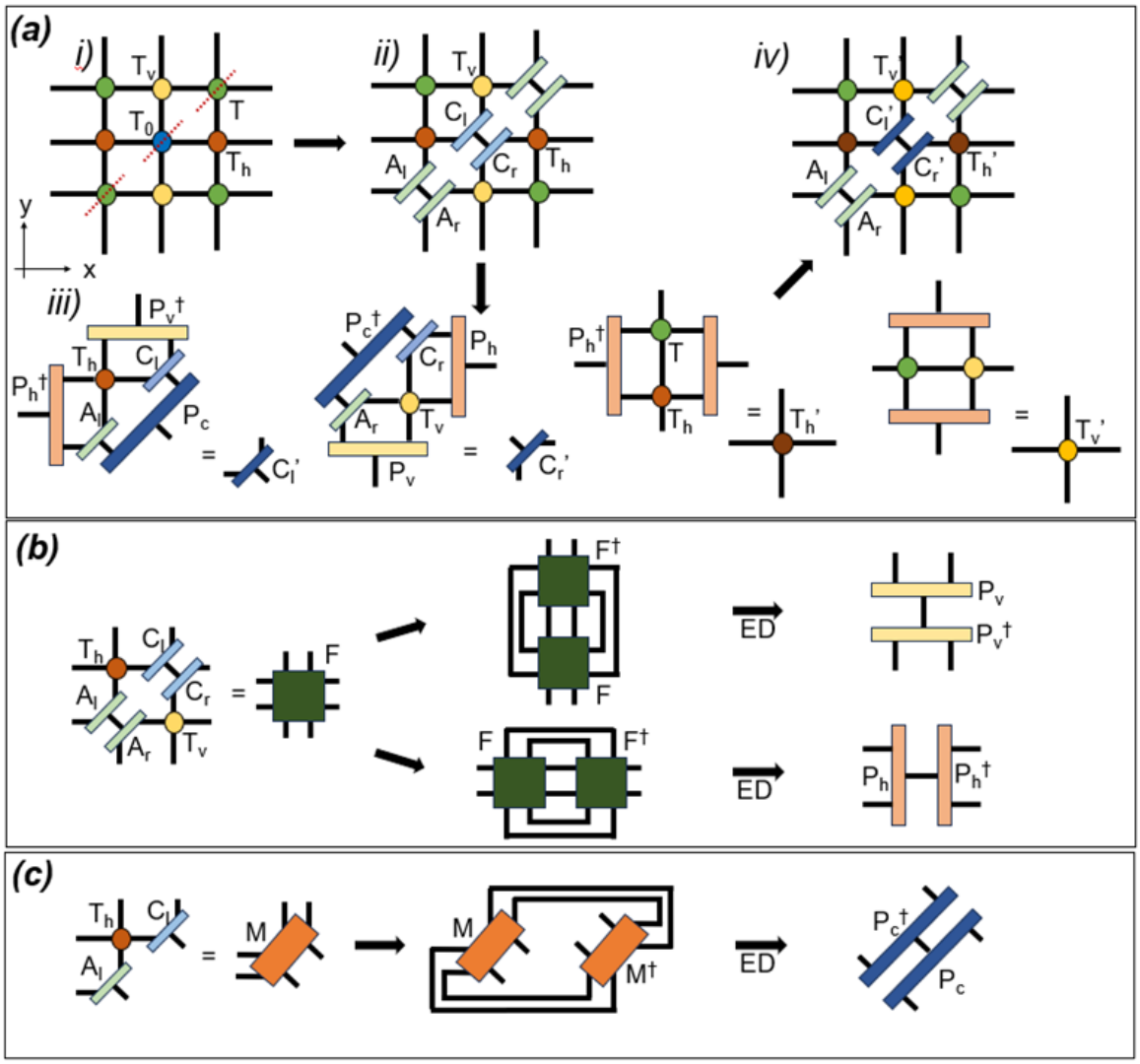

Figure 4.17: The steps used in CTRG.

along the diagonal of the network, splitting the central tensor to

$$T^{C}_{abcd} = C^{L}_{ade} C^{R}_{ebc} \tag{4.54}$$

and all tensors along the same diagonal to

$$T_{abcd} = A^{L}_{ade} A^{R}_{ebc} \tag{4.55}$$

Iterations of the algorithm are then completed on the new network of Figure 4.17.a(ii).

Similar to HOTRG, the CTRG algorithm uses the application of projectors to pull tensors from same row/column (T^{H}_{abcd}, T^{V}_{abcd}) as the core site into the core tensors (C^{L}_{ade}, C^{R}_{ebc}). As such, at each step tensors from the left/bottom (Figure 4.17.a(iii)) or the top/right row or column are contracted into C^{L}_{ade}/C^{R}. By the introduction of the projectors onto the core tensor, the tensors along the row (T^{H}_{abcd}) and column (T^{V}_{abcd}) are updated at the same time. The number of sites from the initial network renormalized into the core tensors per iteration therefore increases over time as the row/column tensors are updated to represent more sites of the initial network.

In practice, the update of the row/column tensors is identical to that of the HOTRG algorithm, using the projectors produced for the core tensor to make the contraction

$$T'^{V}_{mdbn} = P^{V\dagger}_{mae} T^{V}_{ahcd} T_{ebgh} P^{V}_{cgn} \tag{4.56}$$

$$T'^{H}_{amnc} = P^{H\dagger}_{mdh} T_{abgd} T^{H}_{gfch} P^{H}_{bfn} \tag{4.57}$$

To update the core tensors a larger set of tensors is required (Figure 4.17.a(iii)). Considering first the contraction of the left/bottom row/column, C^{L}_{ade} is contracted with the row tensor T^{H}_{abcd}, and further contracted with one of the formulated rank-3 diagonal tensors A^{L}_{ade} as

$$N^{L}_{apedhq} = C^{L}_{agp} T^{H}_{egcd} A^{L}_{chq} \tag{4.58}$$

and similarly for C^{R}_{ebc} with T^{V}_{abcd} and A^{R}_{ebc} to give

$$N^{R}_{pbgcqh} = C^{R}_{pbf} T^{V}_{fgcd} A^{R}_{qdh} \tag{4.59}$$

Projectors can then be applied to these rank-6 tensors to the updated network to

provide the updated core tensors

$$C'^{L}_{jkm} = P^{H\dagger}_{jhd} P^{V\dagger}_{kae} N^{L}_{apedhq} P^{C}_{pqm} \tag{4.60}$$

$$C'^{R}_{mlo} = P^{C\dagger}_{mpq} N^{R}_{pbgcqh} P^{H}_{bhl} P^{V}_{gco} \tag{4.61}$$

completing one iteration of the CTRG algorithm.

To produce the projectors used within CTRG, as with many other algorithms, a chosen sub-network is contracted with its adjoint leaving uncontracted only the edges which will be used to reduce the number of bonds within the system. For CTRG, to make the projectors in the horizontal and vertical direction (P^H, P^V) the sub-network chosen is provided in Figure 4.17.b, leaving exposed the vertical/horizontal indices. However, it should be noted that the presented diagram simplifies the order of operations. That is, when contracting the tensor network with its adjoint the cost may be reduced greatly by contracting individual tensors with their adjoint first, instead of directly constructing the rank-8 tensor. For example, when producing the vertical projectors, the tensor T^V is first contracted with C^L, and the resulting rank-5 tensor is contracted with its adjoint at a leading $\mathcal{O}(\chi^4 n^3)$ cost where n is the edge dimension of the original network.

To make the central projectors for CTRG (P^C), applied in Figure 4.17.a(iii) between the core tensors, a simpler sub-network is required. Here, the previously computed N^L_{apedhq} may be contracted with its adjoint to provide the appropriate sub-network, already at a $\mathcal{O}(\chi^4 n^3)$ cost (Figure 4.17.c). Unlike other algorithms the central, horizontal, and vertical projectors are finally pulled from the system not through an SVD, but rather through an eigenvalue decomposition (ED) of the formulated sub-networks in Figure 4.17.b and Figure 4.17.c.

To pull thermodynamic quantities from the algorithm, the two core tensors C^L and C^R may be fully contracted together over complementary horizontal, vertical, and diagonal edges to produce the partition function Z as

$$Z = C^{L}_{ade} C^{R}_{eda} \tag{4.62}$$

4.3.4 Environment updates

While many of the previous sections focused on the tensors being renormalized only, here a set of algorithms are presented which used the local environment (i.e. the surrounding tensors) in order to optimize each step.

Graph independent local truncation tensor network renormalization (GILT-TNR 1-2)

The GILT-TNR algorithm extends on the TRG algorithm by introducing a preliminary update to each of the network indices through consideration of the local environment around each index [79]. With reference to Figure 4.18, the algorithm begins by the sequential insertion of matrices, called the environment tensors, on each index of the lattice. These tensors are produced through completion of graph independent local truncation GILT. The process begins by the contraction of four lattice sites together, as in Figure 4.18(a.i), leaving open the inner connecting indices on which the environment tensor is to be applied. Here, the brute force contraction of this network results in a rank-10 tensor, making it computationally expensive. While the subsequent steps of the algorithm remain identical regardless, to reduce cost contracting over the external bonds as well is recommended, symbolized by the dashed lines connecting the outer indices of Figure 4.18(a.i), for a total cost of $\mathcal{O}(\chi^6)$, but this is not mandatory.

Following the contraction of the plaquette, an SVD is applied to the resulting tensor, isolating the aforementioned inner indices on a rank-3 tensor U (Figure 4.18(a.i-a.ii)). The two indices are then contracted over each other, forming vector t (Figure 4.18(a.iii-a.iv)). An exchange is then made for t', following the equation

$$t'_i = t_i \frac{S_i^2}{\epsilon^2 + S_i^2} \tag{4.63}$$

where S_i is the i^{th} diagonal element of the tensor S, t_i is the i^{th} element of the vector t, and ϵ is an input parameter. The result is a rescaled version of the vector t by which the smallest elements may be taken as essentially zero, and therefore truncated away when convenient without major information losses. It has was given by the authors of the algorithm that the parameter ϵ should be made large for a greater scaling, with a value of $8E(-7)$ recorded as a generally good value. The vector t' is then contracted back onto the hermitian conjugate of rank-3 tensor U, creating the environment tensor R^1 (Figure 4.18(a.v)).

Decomposing R^1 via a symSVD, and contracting the halves R^{11} or R^{12} onto the original network tensor, T, the bond dimension may be reduced from χ to χ' (Figure 4.18(b.i-b.iii)). The process is then sequentially repeated for each of the other four inner bonds of the plaquette, each time operating on one of the indices of tensor

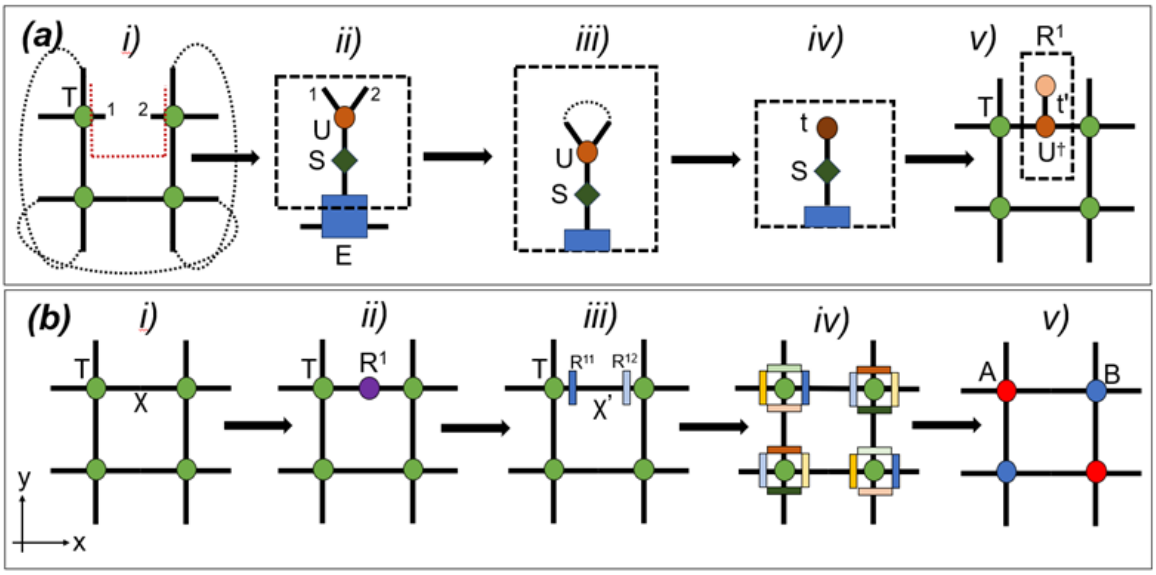

Figure 4.18: The steps used in GILT-TNR.

T before recreating the plaquette and starting the next GILT step. Generally, this process may be repeated many times if desired, continually truncating the dimension of each network index until some specified size is obtained, thus avoiding the need to truncate through only an SVD. For the GILT-TNR algorithm, however, this is not the goal. Instead, the GILT step is iterated just once in an attempt to filter out short range correlations within the system. In this way it could be considered as an updated version of the Tensor Entanglement Filtering Renormalization (TEFR) process, specified in [80], and for this reason the TEFR algorithm has been neglected.

Finishing off the GILT-TNR iteration, by contracting half of the environment tensors onto one side of one network site each step, and the opposite side for the next network site, it is seen that a lattice of marginally different A and B tensors is produced (Figure 4.18(b.iv-b.v)). To retrieve a homogeneous system again an application of regular iteration of the TRG algorithm on the A-B lattice is therefore required.

Second renormalization group (SRG)

The SRG algorithm considers an environment beyond a local plaquette of four sites to produce its optimization [58]. The algorithm begins by constructing an environment tensor by completing N renormalization steps through the TRG algorithm (forward process). At each layer the rank-3 tensors (A, B, C, D) are saved. After the N^{th}

iteration a rank-8 E^{N+1} tensor is constructed, taken as an identity tensor, upon which eight of the rank-3 tensors from the step N may be contracted onto (backwards process). The diagram for this process may be seen in Figure 4.19(i), where the E^{N+1} environment tensor surrounds the system, and the rank-3 tensors are contracted onto its eight interior edges at $\mathcal{O}(\chi^{10})$ cost. In completing this contraction it can be seen that a new rank-8 environment tensor E^N is constructed for the $N-1$ layer of rank-3 tensors. The backwards process is repeated down each layer until the environment tensor E^1 is formed. At this point three tensors from the original lattice (T) are contracted onto the interior of the environment, forming the rank-4 environment tensor E^0 (Figure 4.19(i)).

With the environment contribution calculated, to now use it to optimize renormalization, an SVD is taken of the environment tensor to isolate pairs of edges (Figure 4.19(ii))

$$E^0 = X^1_{cde}\Lambda^1_{eg}Y^1_{gab} \tag{4.64}$$
$$E^0 = X^2_{bch}\Lambda^2_{hf}Y^2_{fad} \tag{4.65}$$

The resulting rank-3 tensors from the decomposition are then contracted back onto a lattice site, giving matrices (Figure 4.19(iii-iv))

$$M^1_{eg} = (\sqrt{\Lambda^1}Y^1)_{eab}T_{abcd}(X^1\sqrt{\Lambda^1})_{cdg} \tag{4.66}$$
$$M^2_{fh} = (\sqrt{\Lambda^2}Y^2_{had})T_{abcd}(X^2\sqrt{\Lambda^2}_{bcf}) \tag{4.67}$$

which are again decomposed as (Figure 4.19(iv-v))

$$M^1_{eg} = R^1_{em}\Omega^1_{mn}L^1_{ng} \tag{4.68}$$
$$M^2_{fh} = L^2_{fo}\Omega^2_{op}R^2_{ph} \tag{4.69}$$

From the rank-3 tensors of the environment decomposition and the determined matrices from the previous decomposition, four rank-3 tensors are created (Figure 4.19(vi))

$$A'_{cdm} = X^1_{cde}(\Lambda^1)^{-1/2}_{eg}L^1_{ng}(\Omega^1)^{1/2}_{mn} \tag{4.70}$$
$$B'_{nab} = (\Omega^1)^{1/2}_{mn}R^1_{em}(\Lambda^1)^{1/2}_{eg}Y^1_{gab} \tag{4.71}$$
$$C'_{bcp} = X^2_{bch}(\Lambda^2)^{-1/2}_{hf}L^2_{fo}(\Omega^2)^{1/2}_{op} \tag{4.72}$$
$$D'_{oad} = (\Omega^2)^{1/2}_{op}R^2_{ph}(\Lambda^2)^{-1/2}_{hf}Y^2_{fad} \tag{4.73}$$

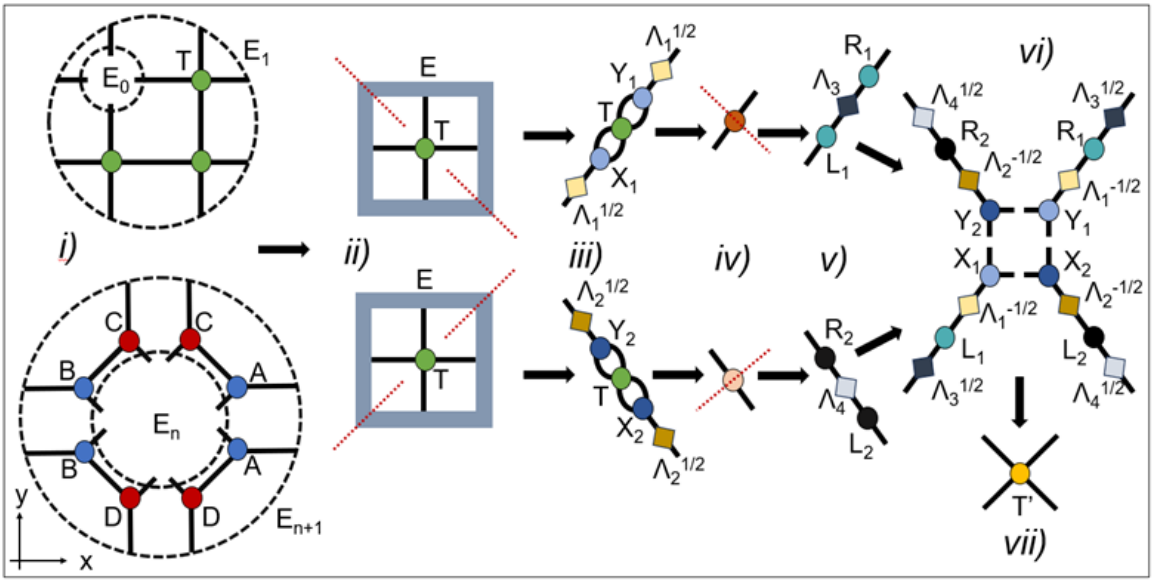

Figure 4.19: The steps used in SRG.

which are contracted together in a similar fashion as TRG to provide the renormalized lattice (Figure 4.19(vii))

$$T'_{mnop} = A'_{cdm} B'_{nab} C'_{bcp} D'_{oad} \tag{4.74}$$

The process of backwards, forwards, and formation of new rank-3 tensors is then repeated to reduce the system size. For SRG on the square lattice a computational cost of $\mathcal{O}(\chi^{10})$ is obtained. The cost for the same operations may be reduced greatly for other lattice systems, however.

Higher-order second renormalization group (HOSRG)

The HOSRG algorithm follows almost entirely the same process as SRG, however, completes it on the infrastructure of HOTRG instead of TRG, and uses the environment tensor to optimize specifically the projectors of HOTRG [59]. HOSRG therefore begins by completing several renormalization iterations through HOTRG, saving both the projectors ($P^{N,x}$ or $P^{N,y}$) and the renormalized tensor (T^N) from the N^{th} iteration. As with SRG, the environment tensor E^{N+1} is taken as the identity tensor, and the environment tensor for the next layer down (E^N) is formed by (Figure 4.20(i))

$$E^N_{mnop} = E^{N+1}_{mefg} P^{N\dagger}_{edn} T_{obgd} P^N_{fbp} \tag{4.75}$$

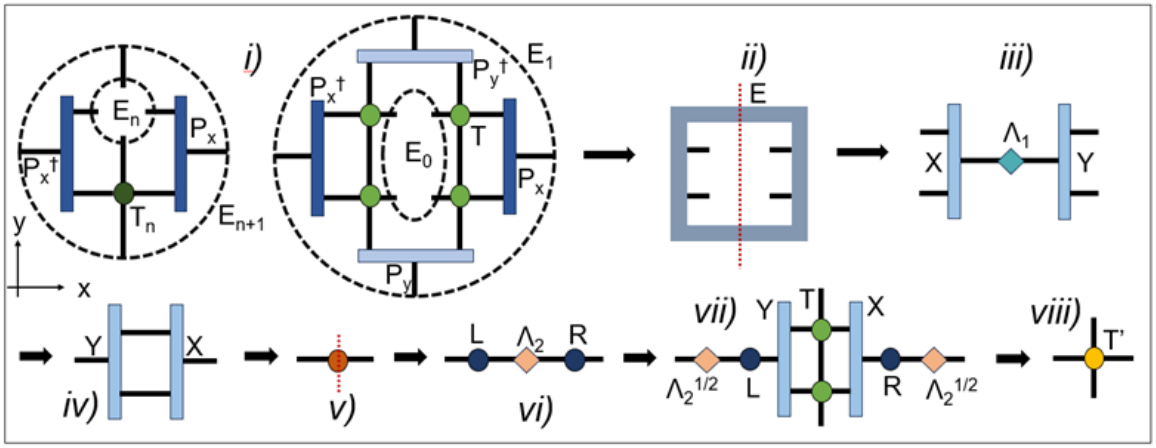

Figure 4.20: The steps used in HOSRG.

Again, the process is then repeated back down the layers until the environment tensor E^1 is obtained. Here, four projectors and four sites of the initial network are contracted on the interior of the E^1 at the leading cost of the algorithm of $\mathcal{O}(\chi^8)$ (Figure 4.20(i)). As seen, two pairs of edges along the horizontal direction have been left exposed to act as the environment (E^0) which computes the projectors. In practice, the indices exposed are alternated between the horizontal and vertical directions.

With the environment tensor E^0 calculated, an SVD is taken over it to provide (Figure 4.20(ii-iii))

$$E^0_{dhbf} = X_{dhm}\Lambda_{mn}Y_{nbf} \tag{4.76}$$

The rank-3 tensors X and Y are then contracted back onto each other to give matrix (Figure 4.20(iv-v))

$$M_{nm} = Y_{nbf}X_{bfm} \tag{4.77}$$

Like with SRG, the matrix M_{nm} is then decomposed as (Figure 4.20(vi))

$$M_{nm} = L_{nj}\Lambda_{jk}R_{km} \tag{4.78}$$

which are then contracted back onto tensors X_{dhm}, Y_{nbf}. The HOSRG algorithm finally completes with an HOTRG process, using tensors X_{dhm}, Y_{nbf} as the projectors.

Again, like SRG, this process of computing the environment and applying it onto the network sites is completed iteratively, but here at a total computational cost of $\mathcal{O}(\chi^8)$. While a difference in accuracy is recorded against SRG in literature, the reduced cost of HOSRG may make it a better option for some models.

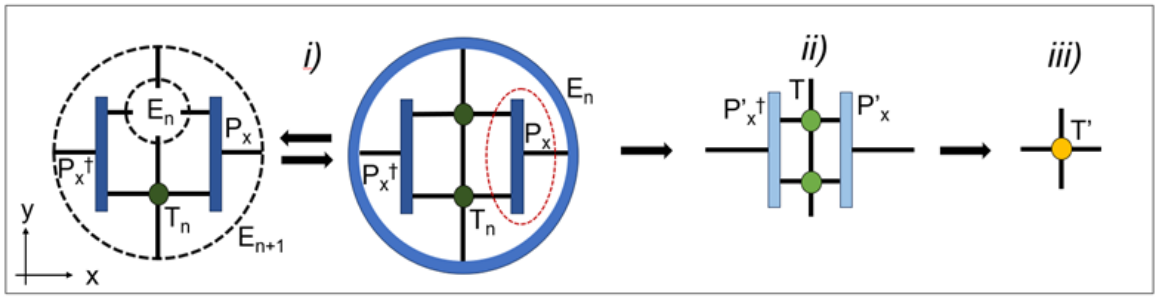

Figure 4.21: The steps used in dTRG.

Differentiable tensor renormalization group (dTRG)

The dTRG algorithm works, again, from the structure of the HOTRG algorithm in a similar way to HOSRG [81]. In fact, even the environment tensor used at each step is constructed the same as HOSRG (Figure 4.21(i)). The novelty here, is that once the environment tensor has been determined at a maximal scale n, the projectors P_{ijk} at scale $n-1$ and below are recalculated from the environment tensor, as well as other projectors and tensors at that scale.

Taking some influence here from the TNR type algorithms, this recalculation is completed by taking an SVD of the local network + environment with the projector to be optimized removed (red oval of Figure 4.21(i)). With the SVD taken by

$$M_{ijk} = U_{ijm}\Lambda_{mn}V^{\dagger}_{nk} \tag{4.79}$$

the projector is reconstructed by

$$P'_{ijk} = U_{ijm}V^{\dagger}_{mk} \tag{4.80}$$

The final projected input back into the network is then an average of the left and right projector recalculated. This process is then done descending backwards down the scales until fully optimized projectors are retrieved from the environment for the initial lattice of tensors T_{abcd} (Figure 4.21(ii)). A HOTRG contraction then completes the first renormalization step of the algorithm. A leading order computational cost is thus found at $\mathcal{O}(\chi^7)$.

4.4 Example calculation

With a brief overview of the algorithms currently completed for the DMRJulia library, omitting non-square lattice variants and those under construction, a short demonstration of accuracy is provided here. Since a full comparison of the algorithms is yet to be completed, three algorithms are arbitrarily chosen for contrast to the exact solutions of the free energy f and specific heat C_v of the Ising model. Following Onsager's well known results [6], the exact free energy density and specific heat are taken here as

$$f = -T\Big(\ln(\sqrt{2}\cosh(\frac{2}{T})) + \frac{1}{\pi}\int_0^{\frac{\pi}{2}} \ln(1+\sqrt{1-c_2^2\sin^2(\phi)})\mathrm{d}\phi\Big) \tag{4.81}$$

and

$$C_v = \frac{2}{\pi T^2}\coth^2(\frac{2}{T})\Big(2K_1 - 2K_2 - (1-c_1)(\frac{\pi}{2}+c_1K_1)\Big) \tag{4.82}$$

where T is the temperature, $c_1 = 2\tanh^2(2/T) - 1$, $c_2 = 2\sinh(2/T)/\cosh^2(2/T)$, and K_1, K_2 are the complete elliptic integrals

$$\begin{aligned} K_1 &= \int_0^{\frac{\pi}{2}} \Big(1 - c_2^2\sin^2(\phi)\Big)^{-1/2}\mathrm{d}\phi \\ K_2 &= \int_0^{\frac{\pi}{2}} \Big(1 - c_2^2\sin^2(\phi)\Big)^{1/2}\mathrm{d}\phi \end{aligned} \tag{4.83}$$

With respect to Figure 4.22, it is seen that not only do the algorithms match each other well, but they also sit precisely on the exact solution curves for both f and C_v for all temperatures tested. The algorithms implemented are therefore known to be accurate as far as replication of the Ising results.

4.5 Summary and future work

With nearly 30 working algorithms coded and implemented to date, and more under way, most of the major tensor network renormalization group algorithms have been considered. While a complete contrast was not provided, basic testing on the Ising model has shown the produced algorithms to have good consistency. Future work is therefore shifted to determining which algorithm is the most accurate for what type of physical system, which is quickest for the least cost of accuracy, and in general to determine any limitations. Since sorting through the information associated with the massive set of possible comparisons, it is expected that this may be an ongoing

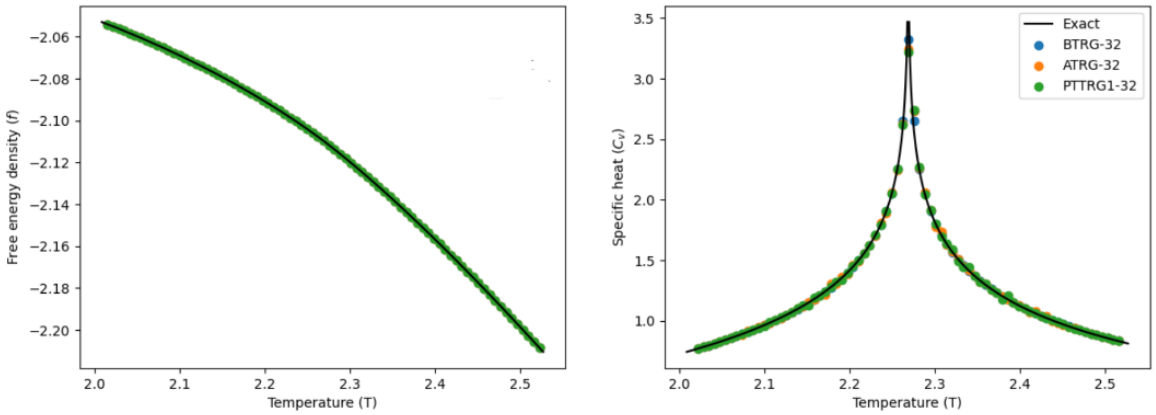

Figure 4.22: The free energy density, f (left), and specific heat, C_v (right), of the Ising model calculated over a range of temperatures, T, for the ATRG, BTRG, and PTTRG-1 algorithms. The bond size has been truncated to 32. The exact solution determined by Onsager is given by the solid black line [6].

process which will adapt over time. In any case, a single library of these algorithms has been produced in order to facilitate this research avenue.

Chapter 5

Summary

Through this thesis three types of physics systems have been explored through both numerical and mathematical methods. In chapter 2, glacier ice thickness was modeled via relative changes in gravitational strength. Not only was the method shown to be effective when compared to other more direct surveying techniques, but a new baseline measurement was also retrieved for Comox glacier. With an accuracy around 5-10% of the total ice thickness, satisfactory for most applications, more critical data on local and global ice volumes may be gained from this process.

In chapter 3, the scale of the system was reduced to a periodic quantum 1D chain, where the Anderson model with CUE disorder was explored. Calculating several statistics, it was seen that adding correlation to the disorder changed some of the scaling collapses, but many of the generic properties observed in the uniform disordered Anderson model remained. In 1D, localization in position space, transition through a peak of chaotic level statistics, and then localization in momentum space stayed as a highly universal feature. Moreover, localization for any hopping amplitude remained a feature. Despite this, new avenues have been opened to look at similar models in higher dimensions. With the 2D spectral statistics exhibiting a much more stable GOE plateau, how the metrics behave in this regime will be interesting to see.

In chapter 4, methods for analyzing 2D (or higher dimension) lattice models were implemented as tensor network renormalization group algorithms. How tensor networks are constructed, what they are looking to calculate in this context, and the general overview of how each algorithm works was discussed. Additionally, it was found that the network which an algorithm acts on does not matter. So long as the normalization constants are considered, simple transformations can take the one lattice to that which the algorithm works on without affecting the physics. Finally, an

example calculation of the well known Ising model free energy density and specific heat was completed, showing good alignment of the numerics with analytic results. While a total of around 30 algorithms have been completed, including non square lattice variants and 3D cubic ones as well, more are still under development. Beyond this, what remains is to find the models where certain algorithms function best, or rather if there is a single algorithm which should unanimously be preferred.

Modeling different kinds of physical systems through numerical and mathematical methods varies greatly from one topic to the next. Through this thesis, some of those methods were explored, and new results were gained across different areas of research. However, more work is required to answer the questions which remain.

Appendix A

Glacier Survey Data and Supplementary Figures

A.1 Data and Tides

Here the data associated with the relative gravity measurements, as well as corrections, are supplied. Figure A.1 depicts the calculated tidal correction for Kokanee and Comox Glacier survey. Table A.1 provides the field data for both glaciers, and Table A.2 further provides the gravity corrections applied to the raw data.

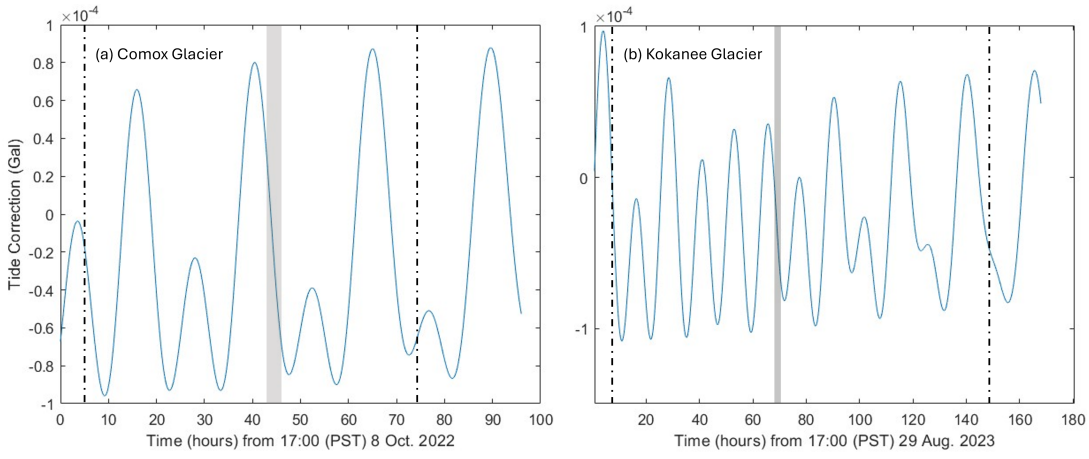

Figure A.1: Calculated corrections for the gravity effect of solid Earth tides for Comox glacier (a) and Kokanee glacier (b) during the survey periods (shaded area) and control measurement points (dashed line).

Table A.1: Gravity survey field data recorded on 10 October 2022 and 1 September 2023 for each point across Comox (left) and Kokanee (right) glacier respectively. Control measurements made before each survey (*av.*) on 8 October 2022 and 30 August 2023, and after each survey (*ap.*) on 11 October 2022 and 4 September 2023 are listed below. The recorded gravitational value (mGal), time of measurement (PST), altitude (Alt.), North and West coordinates (N/W), relative height (Ht.), and distance (Dst.) to the point 1 base station are provided. Any values not required for the consistency of the control measurements were neglected.

Comox glacier

#	*mGal* ±0.05	*PST*	*Alt.*(*m*) ±5	*N/W* ±0.00005	*Ht.*(*m*) ±0.05	*Dst.*(*m*) ±0.1
1	4266.73	12:01	1880	$^{49.54586}/_{-125.35709}$	0.00	0.0
2	4266.52	12:12	1879	$^{49.54617}/_{-125.35698}$	-0.93	37.4
3	4267.04	12:26	1875	$^{49.54662}/_{-125.35704}$	-5.22	84.5
4	4267.61	12:35	1874	$^{49.54694}/_{-125.35701}$	-5.98	120.2
5	4267.90	13:06	1868	$^{49.54726}/_{-125.35697}$	-12.33	155.9
6	4267.12	13:15	1869	$^{49.54767}/_{-125.35723}$	-11.48	201.5
7	4267.33	13:21	1868	$^{49.54831}/_{-125.3575}$	-11.67	274.0
8	4266.92	13:26	1869	$^{49.54887}/_{-125.35764}$	-10.76	337.4
9	4266.93	13:33	1868	$^{49.54925}/_{-125.35768}$	-11.55	409.2
10	4267.78	13:42	1866	$^{49.5498}/_{-125.35726}$	-14.07	438.3
11	4267.12	13:49	1870	$^{49.54983}/_{-125.35796}$	-9.80	445.9
12	4269.71	14:18	1880	$^{49.54586}/_{-125.35709}$	0.00	0.0
av.	4575.63	22:27	-	$^{48.46341}/_{-123.28809}$	-	-
ap.	4575.88	19:16	-	$^{48.46341}/_{-123.28809}$	-	-

Kokanee glacier

#	*mGal* ±0.05	*PST*	*Alt.*(*m*) ±5	*N/W* ±0.00005	*Ht.*(*m*) ±0.05	*Dst.*(*m*) ±0.1
1	3990.29	13:20	2661	$^{49.74992}/_{-117.14843}$	0.00	0.0
2	3987.74	13:34	2659	$^{49.74986}/_{-117.14814}$	-1.13	25.9
3	3986.93	13:41	2659	$^{49.74976}/_{-117.14778}$	-1.41	52.3
4	3986.68	13:47	2658	$^{49.74971}/_{-117.14754}$	-2.11	70.4
5	3986.145	13:53	2659	$^{49.74966}/_{-117.14723}$	-1.53	88.8
6	3985.68	14:03	2658	$^{49.74959}/_{-117.14697}$	-2.41	110.2
7	3985.6	14:12	2657	$^{49.74955}/_{-117.14671}$	-3.09	129.4
8	3984.93	14:20	2658	$^{49.74938}/_{-117.14642}$	-2.63	159.4
9	3984.36	14:25	2660	$^{49.74929}/_{-117.14602}$	-0.78	187.6
10	3984.05	14:32	2661	$^{49.74921}/_{-117.14555}$	0.20	224.1
11	3987.39	14:41	2661	$^{49.74992}/_{-117.14843}$	0.00	0.0
-	-	-	-	-	-	-
av.	4578.96	0:20	-	$^{48.46341}/_{-123.28809}$	-	-
ap.	4579.23	22:21	-	$^{48.46341}/_{-123.28809}$	-	-

Table A.2: Comox (left) and Kokanee (right) glacier gravitational anomaly corrections used to retrieve the Bouguer anomaly for each point over the two transects. The control measurements made before (*av.*) and after (*ap.*) each survey are additionally provided at the bottom. All listed values are in mGal unless stated.

Comox glacier

#	Δg^{tide} ±2.E(−4)	Δg^{drift} ±2.4%	$\Delta g^{lat.}$ ±1.%	$\Delta g^{elev.}$ ±1.%	Δg^{bp} ±5.6%	$\Delta g^{top.}$ ±0.08
1	2.86E(-2)	0.0	0.0	0.0	0.0	0.0
2	2.23E(-2)	0.23	-2.77E(-2)	-0.287	0.113	-0.02
3	1.39E(-2)	0.53	-6.79E(-2)	-1.61	0.635	0.30
4	8.5E(-3)	0.72	-9.65E(-2)	-1.85	0.730	-0.11
5	-1.07E(-2)	1.38	-0.125	-3.81	1.50	0.01
6	-1.62E(-2)	1.57	-0.162	-3.54	1.40	-0.15
7	-1.98E(-2)	1.69	-0.219	-3.60	1.42	0.16
8	-2.26E(-2)	1.80	-2.69E(-2)	-3.32	1.31	0.75
9	-2.68E(-2)	1.95	-0.303	-3.56	1.40	0.55
10	-3.19E(-2)	2.14	-0.352	-4.34	1.71	0.41
11	-3.59E(-2)	2.29	-0.354	-3.02	1.19	0.44
12	-5.08E(-2)	2.90	0.0	0.0	0.0	0.0
av.	-2.02E(-2)	-	-	-	-	-
ap.	-6.55E(-2)	-	-	-	-	-

Kokanee glacier

#	Δg^{tide} ±2.E(−4)	Δg^{drift} ±2.4%	$\Delta g^{lat.}$ ±1.%	$\Delta g^{elev.}$ ±1.%	Δg^{bp} ±3.1%	$\Delta g^{top.}$ ±0.08
1	-3.16E(-2)	0.0	0.0	0.0	0.0	0.0
2	-3.83E(-2)	-0.51	-4.64E(-3)	-0.349	0.130	0.09
3	-4.13E(-2)	-0.76	-1.24E(-2)	-0.435	0.163	0.17
4	-4.40E(-2)	-0.98	-1.62E(-2)	-0.651	0.243	0.15
5	-4.66E(-2)	-1.20	-2.01E(-2)	-0.472	0.176	0.02
6	-5.10E(-2)	-1.56	-2.55E(-2)	-0.743	0.277	0.19
7	-5.47E(-2)	-1.88	-2.86E(-2)	-0.954	0.356	0.22
8	-5.77E(-2)	-2.17	-4.18E(-2)	-0.812	0.303	0.23
9	-5.98E(-2)	-2.35	-4.82E(-2)	-0.241	8.99E(-2)	0.28
10	-6.21E(-2)	-2.61	-5.47E(-2)	6.17E(-2)	-2.31E(-2)	0.29
11	-6.52E(-2)	-2.93	0.0	0.0	0.0	0.0
-	-	-	-	-	-	-
av.	-6.09E(-3)	-	-	-	-	-
ap.	-5.08E(-2)	-	-	-	-	-

Appendix B

Tensor Network Algorithms

B.1 Non-square lattice TRG renormalization diagrams

Two short examples of non-square lattice tensor network renormalization are briefly summarized below. While many more algorithms are, and will be, included in the DMRJulia library, including cubic, kagome, and other algorithm variants, here only the hexagonal and triangular renormalization algorithms are provided. In each case, the algorithm chosen on these lattice types is based on the TRG process.

B.1.1 Triangular lattice TRG

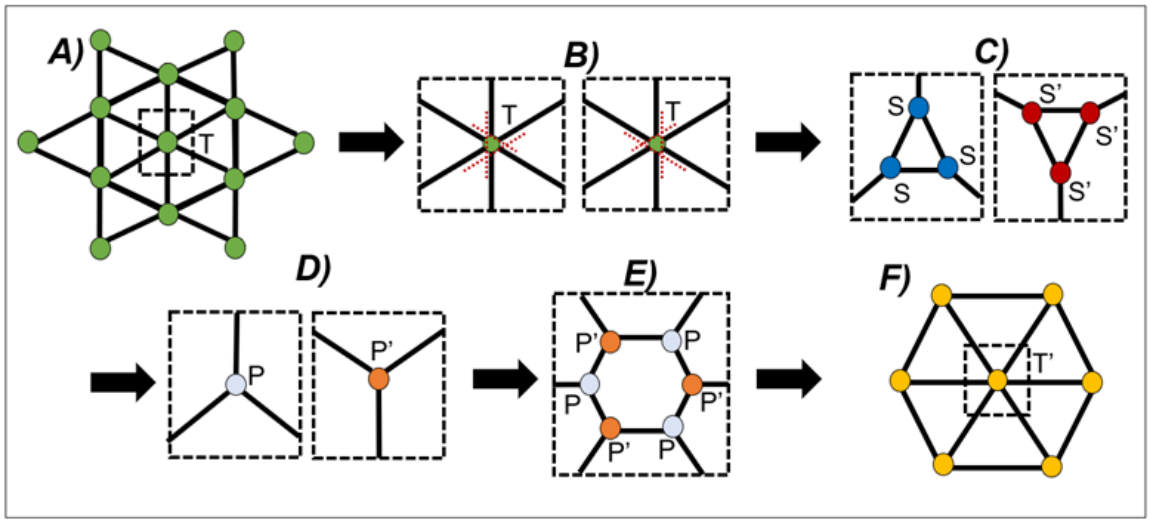

Figure B.1: TRG renormalization on the triangular lattice [7].

With respect to Figure B.1, a similar case to the square lattice TRG algorithm can be seen [7]. The process begins with a 2D lattice of rank-6 tensors T_{ijklnm} (Figure B.1.A). The tensor is then decomposed via a symSVD in six different ways to isolate all possible pairs of indices (Figure B.1.B). Considering the same process occurring on adjacent sites, a network of rank-3 tensors S_{ojk} and S'_{gnm} is produced, connected as in Figure B.1.C. Contracting these small networks together, new rank-3 tensors P_{opq} and P'_{fgh} are formed (Figure B.1.D), connected over the network in a hexagonal formation, as seen in Figure B.1.E. Contracting sets of 6 together, the initial network is reformed as T'_{opqfgh}. The number of sites within the network has thus been reduced by a factor of 3, at a total cost of $\mathcal{O}(\chi^8)$.

B.1.2 Hexagonal lattice TRG

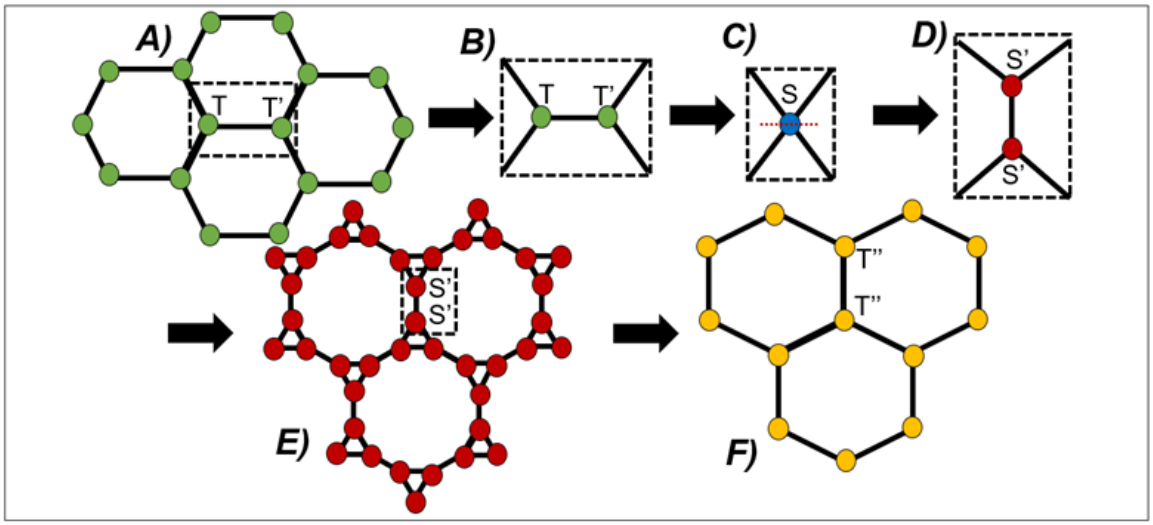

Figure B.2: TRG renormalization on the hexagonal lattice [7].

Unlike the square lattice, the honeycomb or hexagonal lattice has two distinct sites represented by rank-3 tensors T_{ijk} and T'_{kij} which share a mutual linking indices [7]. Following the steps of Figure B.2, the two tensors are initially contracted together over each of the three possible index pairs. One such contraction is depicted in Figure B.2.B to C. The new tensor S_{jknm} is then decomposed orthogonal to the contraction direction to create pairs of rank-3 tensors S'_{jno} and S'_{pkm} (Figure B.2.D), forming the lattice of Figure B.1.E. As with renormalization on the triangular lattice, the subnetwork of tensors forming the triangular patterns are contracted together,

bringing the network back to a hexagonal lattice. The number of sites has thus been reduced by a factor of 3, at a leading computational cost of $\mathcal{O}(\chi^5)$.

Bibliography

[1] L. . R. Inc., "Instruction manual for lacoste & romberg, inc. model g and d land gravity meter," 1989.

[2] H. Burger, A. Sheehan, and C. Jones, *Introduction to Applied Geophysics: Exploring the Shallow Subsurface*. Cambridge University Press, 2023.

[3] B. Pelto, F. Maussion, B. Menounos, V. Radić, and M. Zeuner, "Bias-corrected estimates of glacier thickness in the columbia river basin, canada," *Journal of Glaciology*, vol. 66, no. 260, p. 1051–1063, 2020.

[4] L. Vidmar, L. Hackl, E. Bianchi, and M. Rigol, "Entanglement entropy of eigenstates of quadratic fermionic hamiltonians," *Phys. Rev. Lett.*, vol. 119, p. 020601, Jul 2017.

[5] P. Łydżba, M. Rigol, and L. Vidmar, "Entanglement in many-body eigenstates of quantum-chaotic quadratic hamiltonians," *Physical Review B*, 2021.

[6] L. Onsager, "Crystal statistics. i. a two-dimensional model with an order-disorder transition," *Phys. Rev.*, vol. 65, pp. 117–149, Feb 1944.

[7] M. Levin and C. Nave, "Tensor renormalization group approach to two-dimensional classical lattice models," *Phys. Rev. Lett.*, vol. 99, p. 120601, Sep 2007.

[8] J. Taillant, *Meltdown: The Earth Without Glaciers*. Oxford University Press, 12 2021.

[9] P. Wester, A. Mishra, A. Mukherji, and A. Shrestha, *The Hindu Kush Himalaya Assessment: Mountains, Climate Change, Sustainability and People*. 01 2019.

[10] C. V. R. District, "Comox valley water system." https://www.comoxvalleyrd.ca/Water. last accessed: 14 October 2022.

[11] D. Kloster, "'receding before our eyes': Island glaciers likely to be all gone by mid-century," *Times Colonist*, 2021.

[12] G. Clarke, A. Jarosch, F. Anslow, V. Radić, and B. Menounos, "Projected deglaciation of western Canada in the twenty-first century," May 2015.

[13] B. A. . F. C. A. Initiative, "Vancouver island adaptation strategies, agriculture & food climate action initiative." https://www.bcagclimateaction.ca, 2020.

[14] G. Consortium, "Glacier thickness database 3.1.0." https://doi.org/10.5904/wgms-glathida-2020-10, 2013.

[15] A. R. Bevington and B. Menounos, "Accelerated change in the glaciated environments of western canada revealed through trend analysis of optical satellite imagery," *Remote Sensing of Environment*, vol. 270, p. 112862, 2022.

[16] E. R. Kanasewich, "Gravity measurements on the athabaska glacier, alberta, canada," *Journal of Glaciology*, vol. 4, no. 35, p. 617–631, 1963.

[17] C. Corbató, "Thickness and basal configuration of lower blue glacier, washington, determined by gravimetry," *Journal of Glaciology*, vol. 5, no. 41, p. 637–650, 1965.

[18] W. Lowrie, *Gravity, the figure of the Earth and geodynamics*, p. 43–120. Cambridge University Press, 2007.

[19] P. Schureman, U. Coast, and G. Survey, *Manual of Harmonic Analysis and Prediction of Tides*. Special publication, U.S. Department of Commerce, Coast and Geodetic Survey, 1994.

[20] I. M. Longman, "Formulas for computing the tidal accelerations due to the moon and the sun," *Journal of Geophysical Research (1896-1977)*, vol. 64, no. 12, pp. 2351–2355, 1959.

[21] B. Elsaka, "Comparison of different polynomial degrees for correcting the instrumental drift of scintrex cg-5 autograv gravimeter," *Australian Journal of Basic and Applied Sciences*, vol. 14, pp. 19–25, 05 2020.

[22] F. Cella, "Gtec—a versatile matlab® tool for a detailed computation of the terrain correction and bouguer gravity anomalies," *Computers Geosciences*, vol. 84, pp. 72–85, 2015.

[23] M. British Columbia Ministry of Energy, P. R. Mining, and M. Division, "Geobc: Topographic maps (1:20,000)." https://pub.data.gov.bc.ca/datasets/177864/, 2013.

[24] A. Greene, J. Scoates, D. Weis, E. Katvala, S. Israel, and G. Nixon, "The architecture of oceanic plateaus revealed by the volcanic stratigraphy of the accreted wrangellia oceanic plateau," *Geosphere*, vol. 6, pp. 47–73, 02 2010.

[25] N. Massey, D. MacIntyre, P. Desjardins, and R. Cooney, "Geology of british columbia geoscience map 2005-3," *British Columbia Ministry of Energy, Mines and Petroleum Resources Mining and Minerals Division*, 2005.

[26] R. Consortium, "Randolph glacier inventory – a dataset of global glacier outlines: Version 6.0: Technical report, global land ice measurements from space." https://doi.org/10.7265/N5-RGI-60, 2017.

[27] D. Brown and J. Logan, *Geology and Mineral Evaluation of Kokanee Glacier Provincial Park, Southeastern British Columbia (82F/11,14)*. Paper (British Columbia. Geological Survey Branch), Mineral Resources Division, Geological Survey Branch, 1989.

[28] J. Logan, J. Gabites, and D. Brown, *Galena lead isotope characteristics of mineralization in Kokanee Glacier Provincial Park, southeastern British Columbia (82F/11,14)*. Paper (British Columbia. Geological Survey Branch), Mineral Resources Division, Geological Survey Branch, 1988.

[29] R. Enkin, *The Canadian Rock Physical Property Database - first public release Geological Survey of Canada*. Natural Resources Canada, 2018.

[30] P. Sharma, *Environmental and Engineering Geophysics*. Cambridge University Press, 1997.

[31] D. Farinotti, D. J. Brinkerhoff, G. K. C. Clarke, J. J. Fürst, H. Frey, P. Gantayat, F. Gillet-Chaulet, C. Girard, M. Huss, P. W. Leclercq, A. Linsbauer,

H. Machguth, C. Martin, F. Maussion, M. Morlighem, C. Mosbeux, A. Pandit, A. Portmann, A. Rabatel, R. Ramsankaran, T. J. Reerink, O. Sanchez, P. A. Stentoft, S. Singh Kumari, W. J. J. van Pelt, B. Anderson, T. Benham, D. Binder, J. A. Dowdeswell, A. Fischer, K. Helfricht, S. Kutuzov, I. Lavrentiev, R. McNabb, G. H. Gudmundsson, H. Li, and L. M. Andreassen, "How accurate are estimates of glacier ice thickness? results from itmix, the ice thickness models intercomparison experiment," *The Cryosphere*, vol. 11, no. 2, pp. 949–970, 2017.

[32] A. Pandit and R. Ramsankaran, "Modeling ice thickness distribution and storage volume of glaciers in Chandra Basin, western Himalayas," *Journal of Mountain Science*, vol. 17, pp. 2011–2022, Aug. 2020.

[33] S. C. B. Raper and R. J. Braithwaite, "The potential for sea level rise: New estimates from glacier and ice cap area and volume distributions," *Geophysical Research Letters*, vol. 32, no. 5.

[34] D. Shugar, I. Walker, O. Lian, J. Eamer, C. Neudorf, D. McLaren, and D. Fedje, "Post-glacial sea-level change along the pacific coast of north america," *Quaternary Science Reviews*, vol. 97, pp. 170–192, 2014.

[35] P. Sierant, M. Lewenstein, A. Scardicchio, L. Vidmar, and J. Zakrzewski, "Many-body localization in the age of classical computing*," *Reports on Progress in Physics*, vol. 88, p. 026502, jan 2025.

[36] L. D'Alessio, Y. Kafri, A. Polkovnikov, and M. R. and, "From quantum chaos and eigenstate thermalization to statistical mechanics and thermodynamics," *Advances in Physics*, vol. 65, no. 3, pp. 239–362, 2016.

[37] D. A. Trunin, "Quantum chaos without false positives," *Phys. Rev. D*, vol. 108, p. L101703, Nov 2023.

[38] M. Mehta, *Random Matrices*. Pure and Applied Mathematics, Academic Press, 2004.

[39] J. Šuntajs, T. Prosen, and L. Vidmar, "Spectral properties of three-dimensional anderson model," *Annals of Physics*, vol. 435, p. 168469, 2021. Special issue on Philip W. Anderson.

[40] D. Braun and G. Montambaux, "Spectral correlations from the metal to the mobility edge," *Phys. Rev. B*, vol. 52, pp. 13903–13909, Nov 1995.

[41] M. Lisiecki, L. Vidmar, and P. Łydżba, "Localization transitions in quadratic systems without quantum chaos," *Phys. Rev. E*, vol. 111, p. 054110, May 2025.

[42] J. Šuntajs, T. c. v. Prosen, and L. Vidmar, "Localization challenges quantum chaos in the finite two-dimensional anderson model," *Phys. Rev. B*, vol. 107, p. 064205, Feb 2023.

[43] D. Thouless, "Electrons in disordered systems and the theory of localization," *Physics Reports*, vol. 13, no. 3, pp. 93–142, 1974.

[44] K. Ishii, "Localization of eigenstates and transport phenomena in the one-dimensional disordered system," *Progress of Theoretical Physics Supplement*, vol. 53, pp. 77–138, 1973.

[45] L. Tessieri, I. Herrera-González, and F. Izrailev, "Anomalous localisation near the band centre in the 1d anderson model: Hamiltonian map approach," *Physica E: Low-dimensional Systems and Nanostructures*, vol. 44, no. 7, pp. 1260–1266, 2012.

[46] T. N. Ikeda, L. Vidmar, and M. O. Flynn, "Exact spectral form factors of noninteracting fermions with dyson statistics," *Phys. Rev. B*, vol. 111, p. 144312, Apr 2025.

[47] T. Xiang and C. Wu, *Bogoliubov Transformation*, p. 343–345. Cambridge University Press, 2022.

[48] I. Peschel and V. Eisler, "Reduced density matrices and entanglement entropy in free lattice models," *Journal of Physics A: Mathematical and Theoretical*, vol. 42, p. 504003, dec 2009.

[49] R. E. Prange, "The spectral form factor is not self-averaging," *Phys. Rev. Lett.*, vol. 78, pp. 2280–2283, Mar 1997.

[50] E. J. Torres-Herrera, J. A. Méndez-Bermúdez, and L. F. Santos, "Level repulsion and dynamics in the finite one-dimensional anderson model," *Phys. Rev. E*, vol. 100, p. 022142, Aug 2019.

[51] Y. Y. Atas, E. Bogomolny, O. Giraud, and G. Roux, "Distribution of the ratio of consecutive level spacings in random matrix ensembles," *Phys. Rev. Lett.*, vol. 110, p. 084101, Feb 2013.

[52] V. Oganesyan and D. A. Huse, "Localization of interacting fermions at high temperature," *Phys. Rev. B*, vol. 75, p. 155111, Apr 2007.

[53] G. Vidal, J. I. Latorre, E. Rico, and A. Kitaev, "Entanglement in quantum critical phenomena," *Phys. Rev. Lett.*, vol. 90, p. 227902, Jun 2003.

[54] I. Peschel, "Calculation of reduced density matrices from correlation functions," *Journal of Physics A: Mathematical and General*, vol. 36, p. L205, mar 2003.

[55] M.-C. Chung and I. Peschel, "Density-matrix spectra of solvable fermionic systems," *Phys. Rev. B*, vol. 64, p. 064412, Jul 2001.

[56] L. Kadanoff, "Scaling laws for ising models near T_c," *Physics Physique Fizika*, vol. 2, pp. 263–272, Jun 1966.

[57] G. Evenbly and G. Vidal, "Tensor network renormalization," *Phys. Rev. Lett.*, vol. 115, p. 180405, Oct 2015.

[58] H. H. Zhao, Z. Y. Xie, Q. N. Chen, Z. C. Wei, J. W. Cai, and T. Xiang, "Renormalization of tensor-network states," *Phys. Rev. B*, vol. 81, p. 174411, May 2010.

[59] Z. Y. Xie, J. Chen, M. P. Qin, J. W. Zhu, L. P. Yang, and T. Xiang, "Coarse-graining renormalization by higher-order singular value decomposition," *Phys. Rev. B*, vol. 86, p. 045139, Jul 2012.

[60] H. Zou, B. Liu, E. Zhao, and W. Liu, "A continuum of compass spin models on the honeycomb lattice," *New Journal of Physics*, vol. 18, p. 053040, may 2016.

[61] T. E. Baker *et al.*, "DMRjulia: Tensor recipes for entanglement renormalization computations," *arXiv preprint arXiv:2111.14530*, 2021.

[62] F. Reif, *Fundamentals of Statistical and Thermal Physics*. Waveland Press, 2009.

[63] R. Pathria and P. Beale, *Statistical Mechanics*. Academic Press, 2021.

[64] D. Adachi, T. Okubo, and S. Todo, "Bond-weighted tensor renormalization group," *Phys. Rev. B*, vol. 105, p. L060402, Feb 2022.

[65] R. Baxter, "Dimers on a rectangular lattice," *Journal of Mathematical Physics*, vol. 9, no. 4, pp. 650–654, 1968.

[66] T. Nishino and K. Okunishi, "Corner transfer matrix algorithm for classical renormalization group," *Journal of the Physical Society of Japan*, vol. 66, no. 10, pp. 3040–3047, 1997.

[67] R. "Orús and G. Vidal, "Simulation of two-dimensional quantum systems on an infinite lattice revisited: Corner transfer matrix for tensor contraction," *Phys. Rev. B*, vol. 80, no. 9, p. 094403, 2009.

[68] M. T. Fishman, L. Vanderstraeten, V. Zauner-Stauber, J. Haegeman, and F. Verstraete, "Faster methods for contracting infinite two-dimensional tensor networks," *Phys. Rev. B*, vol. 98, p. 235148, Dec 2018.

[69] W. Li, S.-J. Ran, S.-S. Gong, Y. Zhao, B. Xi, F. Ye, and G. Su, "Linearized tensor renormalization group algorithm for the calculation of thermodynamic properties of quantum lattice models," *Phys. Rev. Lett.*, vol. 106, p. 127202, Mar 2011.

[70] Y.-L. Dong, L. Chen, Y.-J. Liu, and W. Li, "Bilayer linearized tensor renormalization group approach for thermal tensor networks," *Phys. Rev. B*, vol. 95, p. 144428, Apr 2017.

[71] G. Evenbly, "Algorithms for tensor network renormalization," *Phys. Rev. B*, vol. 95, p. 045117, Jan 2017.

[72] G. Vidal, "Class of quantum many-body states that can be efficiently simulated," *Phys. Rev. Lett.*, vol. 101, p. 110501, Sep 2008.

[73] Y. Nakamura, H. Oba, and S. Takeda, "Tensor renormalization group algorithms with a projective truncation method," *Phys. Rev. B*, vol. 99, p. 155101, Apr 2019.

[74] G. Evenbly, "Implicitly disentangled renormalization," *arXiv: Quantum Physics*, 2017.

[75] G. Bergqvist and E. Larsson, "The higher-order singular value decomposition: Theory and an application [lecture notes]," *IEEE Signal Processing Magazine*, vol. 27, no. 3, pp. 151–154, 2010.

[76] D. Adachi, T. Okubo, and S. Todo, "Anisotropic tensor renormalization group," *Phys. Rev. B*, vol. 102, p. 054432, Aug 2020.

[77] D. Kadoh and K. Nakayama, "Renormalization group on a triad network," 12 2019.

[78] W. Lan and G. Evenbly, "Tensor renormalization group centered about a core tensor," *Phys. Rev. B*, vol. 100, p. 235118, Dec 2019.

[79] M. Hauru, C. Delcamp, and S. Mizera, "Renormalization of tensor networks using graph-independent local truncations," *Phys. Rev. B*, vol. 97, p. 045111, Jan 2018.

[80] Z. Gu and X. Wen, "Tensor-entanglement-filtering renormalization approach and symmetry-protected topological order," *Phys. Rev. B*, vol. 80, p. 155131, Oct 2009.

[81] B.-B. Chen, Y. Gao, Y.-B. Guo, Y. Liu, H.-H. Zhao, H.-J. Liao, L. Wang, T. Xiang, W. Li, and Z. Y. Xie, "Automatic differentiation for second renormalization of tensor networks," *Phys. Rev. B*, vol. 101, p. 220409, Jun 2020.